

REPORT DOCUMENTATION PAGE				Form Approved OMB No. 0704-0188	
Public reporting burden for this collection of information is estimated to average 1 hour per response, including the time for reviewing instructions, searching existing data sources, gathering and maintaining the data needed, and completing and reviewing this collection of information. Send comments regarding this burden estimate or any other aspect of this collection of information, including suggestions for reducing this burden to Department of Defense, Washington Headquarters Services, Directorate for Information Operations and Reports (0704-0188), 1215 Jefferson Davis Highway, Suite 1204, Arlington, VA 22202-4302. Respondents should be aware that notwithstanding any other provision of law, no person shall be subject to any penalty for failing to comply with a collection of information if it does not display a currently valid OMB control number. <b>PLEASE DO NOT RETURN YOUR FORM TO THE ABOVE ADDRESS.</b>					
1. REPORT DATE (DD-MM-YYYY) 9/30/2008		2. REPORT TYPE FINAL REPORT		3. DATES COVERED (From - To) Aug 2007 - September 2008	
4. TITLE AND SUBTITLE  Passive Collision Avoidance System for UASs				5a. CONTRACT NUMBER N00014-07-C-0755	
				5b. GRANT NUMBER	
				5c. PROGRAM ELEMENT NUMBER	
6. AUTHOR(S)  Wilson, Mike Baker, Glenn				5d. PROJECT NUMBER 06PR00293-00/07PR07105-00	
				5e. TASK NUMBER	
				5f. WORK UNIT NUMBER	
7. PERFORMING ORGANIZATION NAME(S) AND ADDRESS(ES)  MilSys Technologies, Inc. 408 East 4 <sup>th</sup> Street, Ste. 204 Bridgeport, PA 19405-1823				8. PERFORMING ORGANIZATION REPORT NUMBER MST080005	
9. SPONSORING / MONITORING AGENCY NAME(S) AND ADDRESS(ES) Office of Naval Research Code 3123: James Waterman 875 North Randolph St, Suite 1425 Arlington, VA 22203-1995				10. SPONSOR/MONITOR'S ACRONYM(S) ONR	
				11. SPONSOR/MONITOR'S REPORT NUMBER(S)	
12. DISTRIBUTION / AVAILABILITY STATEMENT Distribution Statement A: Approved for Public Release					
13. SUPPLEMENTARY NOTES					
14. ABSTRACT MilSys has demonstrated the feasibility of using SWAP efficient LWIR microbolometers as outlined in the Priest report circa 1998 as a solution to the collision avoidance problems for UASs . It has accomplished this by, modeling the response, collecting data and leveraging and developing detection and tracking algorithms that could be implemented into future systems. Design proposals were completed that showed the feasibility of extending the concept up to larger aircraft and down the smaller Tier I type UASs. To solve the entire collision avoidance problem, as discussed by the JIPT, technology was proposed, that would create an integrated color FPA that could determine range, weather, and still perform the collision avoidance function					
15. SUBJECT TERMS Sense and Avoid, Collision Avoidance, UAS					
16. SECURITY CLASSIFICATION OF:			17. LIMITATION OF ABSTRACT  UU	18. NUMBER OF PAGES  102	19a. NAME OF RESPONSIBLE PERSON Sandy Oehmke
a. REPORT U	b. ABSTRACT U	c. THIS PAGE U			19b. TELEPHONE NUMBER (include area code) (610) 272-5050

## **TITLE: Passive Collision Avoidance System for UAS**

COMPANY NAME: MilSys Technologies, LLC  
COMPANY ADDRESS: 408 East 4<sup>th</sup> Street, Ste. 204  
Bridgeport, PA 19405-1823  
DATE (MONTH YEAR): September 2008  
FINAL REPORT Contract No. N00014-07-C-0755



## Table of Contents

1	Identification and Significance of the Problem or Opportunity.....	1
1.1	Background - SAA .....	1
1.2	MilSys Technologies Passive Collision Avoidance System (PCAS) .....	2
1.3	Technical Approach .....	3
1.4	Operational .....	5
2	System Modeling .....	6
2.1	Bolometer sensor model(s) overview .....	6
2.1.1	Excel model for single detector pixel performance prediction .....	6
2.1.2	Imaging matlab model for aggregate pixel (FPA and sensor) performance prediction .....	7
2.1.3	Capacity for sequential vendor model inputs and fair comparison .....	8
2.1.4	Iterative heat balance equation and comparison to approximations often used .....	8
2.2	Sensor systems model and evaluation criteria .....	9
2.2.1	Mathematical basis for model: NETD, NEP, MTF, CTF, and MRTD equations compiled and derived from literature and from NVTherm models .....	9
2.2.2	System level analysis (bar target imaging and MRTD prediction) .....	11
2.2.3	MTF, CTF, target temperature contrast and probabilities of detection, recognition and identification .....	13
2.3	Model validation .....	13
2.3.1	NETD comparisons to literature and other model results .....	13
2.3.2	MTF and MRTD comparisons to NVTherm2002 and NVTherm IP .....	14
2.3.3	Detection, identification and recognition of small (subtended) objects .....	15
2.4	Observations/conclusions from manufacturer's data and model results .....	17
2.4.1	Relative strengths of noise sources .....	17
2.4.2	1/f noise detail .....	18
2.4.3	Response times and sensitivity comparisons .....	18
2.5	Simulation of microbolometer sensors for aerial collision avoidance .....	19
2.6	Some unique attributes of the model .....	24
2.7	Summary and discussion .....	25
3	Hardware and Software .....	26
3.1	Data Collection Software .....	26
3.2	COTS Microbolometers .....	27
3.3	GPS Data Logger .....	29
3.4	Aircraft .....	31



3.5	Camera hardware development .....	32
3.6	Airports .....	35
4	Representative Data Collections .....	36
5	Algorithm Development.....	40
5.1	UConn Report.....	40
5.2	Image Differencing.....	76
6	Hardware Approach for Tier I UAV.....	78
7	Extension of the Technological Approach to solve the full CA problem .....	80
7.1	Introduction.....	80
7.2	Cloud Detection via Infrared Imaging (Background) .....	81
7.3	LWIR Multispectral Sensor.....	84
7.4	LWIR Temperature Sensor and Passive Ranging .....	87
7.5	Autonomous Avoidance .....	88
7.5.1	Autonomous avoidance Algorithms.....	88
8	Conclusion .....	89
9	References .....	90

## Table of Tables

Table 1: Potential configurations for various airframes. The nomenclature of X/Y refers to the number of sensors and the need for a central track processor. ....	1
Table 2: Factors effecting collision times.....	4
Table 3: Relative ratios of noise from data packages and this model's predictions.....	18
Table 4: NETD's predicted from model for like-detectors of VOx and a-Si for different levels of 1/f noise. ....	19
Table 5: Comparison of the specifications of the two(2) main MB technologies.....	28
Table 6: Specifications for Piper and Cessna. ....	31
Table 7: Slant Range estimates of ground-air data.....	39
Table 8: Estimated weight. ....	78
Table 9: L-3 3600AS. ....	79
Table 10: JIPT SAA requirements. ....	81

## Table of Figures

Figure 1: Schematic of MilSys Technologies Passive Collision Avoidance System. ....	2
Figure 2: Flow diagram of the image through the sensor.....	5
Figure 3: Example of a detection report.....	5
Figure 4: Block diagram of some of the processing algorithms.....	6
Figure 5: Excel performance chart .....	6
Figure 6: Scene, optics and electronics inputs .....	7
Figure 7: Simulated bar target images from the matlab program .....	8
Figure 8: bolometer choice section.....	8
Figure 9: Heat balance equations.....	9
Figure 10: NETD as a function of f-number (left) and of scene temperature (right).....	10
Figure 11: MTF's vs. spatial frequency.....	11
Figure 12: MRTD's from theory (top blue and yellow), from NVTherm IP runs (black diamonds), and discerned from matlab image sequences shown at 30Hz (red circles); three images at 1.25*NETD bar target temperature and summed over the eye integration time are shown at bottom right.....	12
Figure 13: Main sheet for sensor performance evaluation .....	13
Figure 14: MRTD's from equations (blue and purple), NVTherm IP outputs (red diamonds), matlab image viewing (green squares), left plot is without Stmp component, right is with full expression .....	15
Figure 15: MRTD curves (temperature vs. spatial frequency and vs. range) for a 4x4 meter target .....	17
Figure 16: Effective temperatures of horizontal path vs. altitude (left) and 8-12um transmittances vs. range for altitudes from sea level to 10km (right) .....	20
Figure 17: SNR's vs. target range for case 1 and 2 sensor configurations .....	22
Figure 18: SNR's vs. range for case 3.....	22
Figure 19: SNR's vs. range with NETD varied from 20 mK to 50 mK .....	22
Figure 20: Three atmospheres currently simulated in program.....	23
Figure 21: Case #2 with a +30F target and at altitudes from 0 to 3 km for the 1976 US standard 23km vis, the MLS 23km vis and the MLS 5km vis atmospheres. ....	24
Figure 22: solid angle of scene (phi/pi) gives more accurate NETD at f/1 and lower .....	25
Figure 23: Streams5 screen capture .....	26
Figure 24: Modules to developed to control the camera and IMU.....	27
Figure 25: Raytheon microbolometer 320 X 240, 25um with electronics .....	28
Figure 26: STD and average of the L-3 microbolometer. Note the red circle is a defect in the FPA.....	28
Figure 27: Camera system used to collect initial data of Ultralight. Both BAE and L3 are shown. ....	29

Figure 28: Dual L-3 Camera used in later side by side data collections.....	29
Figure 29: LandAirSea GPS data logger. ....	30
Figure 30: An example of the data export from the GPS tracker into Google Earth. ....	30
Figure 31: Piper aircraft used for data collections.....	31
Figure 32: Piper from website. ....	31
Figure 33: Cessna from website.....	31
Figure 34: Kolb FireStar Ultralight 33ft wing span cruising speed 60mph. ....	32
Figure 35: LWIR image of the Ultralight. Muffler runs at approximately 1200°F.....	32
Figure 36: 3D model of LVDS circuit board with L-3 AS4500. ....	33
Figure 37: Silk screen of circuit board. ....	33
Figure 38: Assembled camera and cable. ....	33
Figure 39: L3 Core with LVDS circuit board. ....	33
Figure 40: 3D model of GiGE and IMU with L-3 AS4500. ....	33
Figure 41: View of the completed camera. ....	33
Figure 42: View of the completed camera. ....	34
Figure 43: Installation of the computer, battery, and DC charger.....	35
Figure 44: Mini-ITX computer.....	35
Figure 45: View of the completed camera installed in the UltraLight.....	35
Figure 46: Ariel View with flight path of the Pottstown Airport, PA. ....	35
Figure 47: Dual camera setup at Pottstown Airport. ....	36
Figure 48: Ariel View of the Pottstown Airport, PA.....	36
Figure 49: Ariel View of the Alloway Airport, NJ. ....	36
Figure 50: Ground level view of the Alloway Airport. ....	36
Figure 51: BAE (left) and L-3 (right) collected at the Alloway Airport using camera configuration in Figure 27.....	37
Figure 52: L-3 both parallel (Figure 28) collected at Pottstown Airport. ....	37
Figure 53: L-3 side by side (Figure 28) collected at Pottstown Airport. ....	38
Figure 54: Frame showing Piper crossing from one camera FOV to another later in the data collection of Figure 53. ....	38
Figure 55: Initial test flight of the IMU for Air-Air data collection.....	39
Figure 56: The angular velocity of the roll of the aircraft for Figure 55. ....	40
Figure 59: Video track of Ultralight of Figure 6 of the UConn report showing no collision. ....	76
Figure 60: Video track of Ultralight of Figure 7 of the UConn report showing collision course. .	76
Figure 59: Video track of Piper aircraft using side by side L3 cameras at Pottstown Airport (Figure 28). Left hand side in the data logger GPS track, right hand side is the calculated track .....	76

Figure 58: Flow diagram of the image through the sensor.....	78
Figure 61: Side on diagram of the propose sensor / TP. Note the dimensional scales. ....	78
Figure 62: Block diagram of how the new functions of air-ground would be implemented to leverage the existing PCAS architecture and developments. ....	79
Figure 63: Temmek Optics – IRViper Lens, F/# 0.8, FOV $\approx 80^\circ \times 60^\circ$ , Weight – 260g.....	80
Figure 64: Schematic of a wide angle FOV converter.....	80
Figure 65: Schematic of a Fresnel lens. ....	80
Figure 66: Transmission spectrum of Fresnel Technologies POLY IR® 2 IR plastic.....	80
Figure 67: Down-welling atmospheric emission spectrum for the Atmosphere model, shown for a clear sky with three different values of water vapor content (0.1x, 1x, and 2x the standard value) and for altostratus clouds (top blue).....	82
Figure 68: Atmospheric transmittance for a zenith path through the Standard Atmosphere. The top (blue) curve 1x water vapor, and the bottom curve (red) is for 2x. ....	82
Figure 69. Down-welling emission spectrum for clear sky (blue curve, bottom), very thin cirrus at 9 km altitude (red curve, 2 <sup>nd</sup> from bottom), alto-stratus cloud at 2.4 km (green curve, 3 <sup>rd</sup> from bottom), and cumulus cloud with its base near 100 m (teal curve, top). ....	83
Figure 70. Images from the wide-angle Infrared Cloud Imager system developed at Montana State University: (left) radiance, (center) residual radiance after removing atmospheric emission, and (right) detected clouds classified by cloud type (from 0 = no clouds to 5 = thick clouds as described in text).....	83
Figure 71: LWIR image of clouds using $\mu$ bolometer. Red circle is an aircraft. ....	84
Figure 72: Image before rain. ....	84
Figure 73: Image during rain. ....	84
Figure 74: Cloud formations. ....	84
Figure 75: Same day as Figure 74 .....	84
Figure 76: Representation of different filters.....	85
Figure 77: Schematic of a GMR membrane (purple) above a pixel (light blue). ....	85
Figure 78: SEM of a wire grid polarizer produced by L-3.....	85
Figure 79. An example of a fabricated guided-mode resonance element with comparison between experiment and theory for a double-layer device (a). The parameters used for the theoretical curve fit are close to the nominal values; they are cover refractive index $n_c=1.0$ , $n_1=1.454$ (SiO <sub>2</sub> ), $n_2=1.975$ (HfO <sub>2</sub> ), substrate index $n_s=1.454$ , $d_1=135$ nm, fill factor (fraction of period occupied by the higher-index medium) $F=0.58$ , $d_2=208$ nm, period $F\Lambda=446$ nm, and angle of incidence $\theta=0^\circ$ (b). A scanning electron micrograph (SEM) and a schematic of the device are shown (c). ....	85
Figure 80: Example of the movement of a FPA to produce “multispectral image of an IFOV of the FOV. Each arrow ( $\rightarrow$ ) represent the physical movement of the FPA in time. ....	86
Figure 81: Pentax.....	86

<b>Figure 82: Blackbody curve for 25-100°C (300-380K). The blue box is the 8-10<math>\mu</math>m waveband, yellow is 10-12<math>\mu</math>m. The ratio between the total integrated radiance in each waveband indicates the temperature (Equation 3).</b>	<b>87</b>
Figure 83: Data collected of an aircraft in the distance with a COTS microbolometer.....	87
Figure 84: Schematic representation of the “safety” bubble.....	88

# 1 Identification and Significance of the Problem or Opportunity

It is a recognized requirement in the development path of UASs, by the DoD, FAA and commercial interests, that to reach the next level of autonomy they must be capable of sensing their environment and reacting as necessary. As defined by the JIPT<sup>i</sup> in their recently published draft UAS requirements document, a sense and avoid (SAA) system encompass the following functions: air-to-air, air-to-ground, ground-to-ground, ground-to-air, and man made hazards. Current and future plans envision UASs ranging in size from the micro (approximately 6 inches) to the macro (747 FedEx freighters) while their missions will range from crop dusting to the extreme in the battlefield to flight time of a few minutes to many days. In a SAA system, many of these functions can and may overlap in technology implementation or may not be required for specific missions or platforms. Due to the war and lack of standards, technology development has not kept up with market need. A SAA system is an enabling technology. There currently exist only a few technologies that have the capability and maturity to address both the operational needs and SWAP requirements for a SAA in the short or near term. The JIPT has estimated their timeline for full implementation and certification out to 2020 as well as RTCA SC-203 has now estimated that their standards will not be completed until 2020. However, the fact of the matter is, that the DoD is flying UASs day-in-and-day-out without SAA. This provides a clear path to gain experience and deploy a SAA system that may not include all JIPT functions but, will enable new missions, safer missions, lower costs and manpower requirements without a lengthy certification process. The FAA has indicated, in open forums; 1) that they are open to type certification for a SAA system for civilian operation, and 2) that they expect the first system to achieve certification to set the standard for the industry<sup>ii</sup>.

To meet the SWAP, mission (both civilian and military), and budgetary requirements of UAS manufacturers, MilSys Technologies is developing a core collision avoidance (CA) technology that is platform centric and can be leveraged across widely varying platforms

and divergent missions (Table 1). This will be accomplished by both innovative hardware and algorithm design. MilSys Technologies believes that it is possible in the near term to produce a system that has FOV of 50 to 220°, weighs <0.5lbs, and has the functions to perform air-air, air-ground, and autonomous maneuvering.

The goals of the program were to demonstrate the feasibility of using both COTS hardware and existing target detector and tracker technology for the purpose of developing a SWAP efficient collision avoidance system for UASs. The goals were partially met in that significant work was completed in both hardware and algorithms, but technical difficulties arose and time ran out on the present contract, before a full demonstration could be completed.

## 1.1 Background - SAA

Several different technologies are now being evaluated. They range from microwave, radar, EO active, EO passive, and even acoustic. The type of technology employed will primarily be a

	Tier I – Dragon Eye	Tier II – Scan Eagle	Tier II+/Tier III Global Hawk/Predator
	System 1/0	System 2/1	System 5/1
Weight	<0.5lbs	<1lbs	<8lbs
Size	0.01 ft <sup>3</sup>	0.03 ft <sup>3</sup>	<0.1ft <sup>3</sup>
Power	<5W	<10W	<30W
FOV	50°	100°	220°
<b>Table 1: Potential configurations for various airframes. The nomenclature of X/Y refers to the number of sensors and the need for a central track processor.</b>			

function of the platform and mission. Each is unique and no one technology will cover all of the possibilities.

Currently, FAA has been directing the regulatory development of SAA through the 14 CFR 91:113 Right of way rules. Which to paraphrase, states that all pilots are required to “see and avoid” other aircraft, whether operating under Instrument Flight Rules (IFR) or Visual Flight Rules (VFR), when conditions permit. The FAA has empowered the RTCA and ASTM to develop the regulatory /standards framework required so that UAVs can be granted equal access, as manned aircraft, to the national air space (NAS). Since “to see” is a

human function, a natural limit on the requirements of a SAA system is that it must be “only as good as” a pilot. As one can imagine, as a technical solution to the problem, the human solution has its limitations. The literature indicates that a diligent pilot can nominally cover  $\pm 110^\circ$  horizontal and  $\pm 15^\circ$  vertical not including obstructions. Poor eyesight, fatigue, distractions and the environment generally limit the range of contact to 1 to 1.5 miles and 12<sup>iii</sup> seconds of warning and in most cases is significantly worse<sup>iv</sup>.

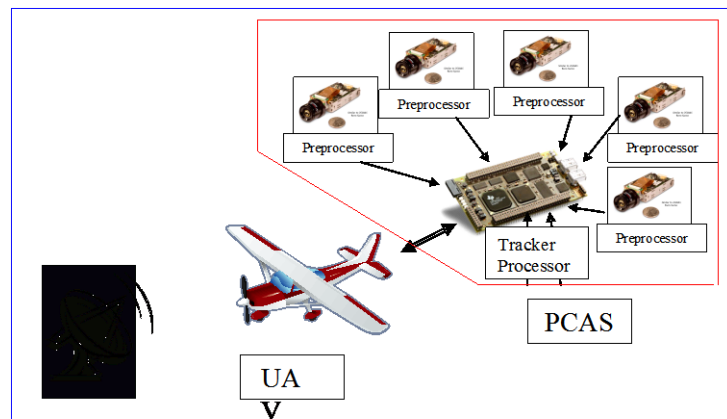


**Figure 1: Schematic of MilSys Technologies Passive Collision Avoidance System.**

## 1.2 MilSys Technologies Passive Collision Avoidance System (PCAS)

MilSys Technologies has been developing a collision avoidance system for the past three (3) years. The program is currently funded under an ONR BAA (contract N00014-07-C-0755). The primary goals are to design, develop, and certify a passive collision avoidance system (PCAS) for UASs. The statement of work focuses on designing and developing a man-in-the-loop (MITL) PCAS based on COTS components for UASs greater than 17' wingspan or multi-tens of pounds payload capacity (i.e. Predator). This systematic concept was extended and downsized for the application to Tier II and Tier I UASs, such as Raven, SilverFox, ScanEagle etc. By unit deliveries, these classes are the largest. Additionally, part of the funding was allocated to advanced developments of future sensors and concepts which could potentially meet JIPT requirements within the developed PCAS architecture. Overall, the effort is as a multi-year hardware and software development program culminating in flight certification in the final year.

The technology is based on uncooled LWIR microbolometer sensors (MB) in a staring configuration as proposed by the Priest<sup>v</sup> report of 1998. The MBs will be distributed around the perimeter of the aircraft with up to 360° of coverage. The total number of sensors could range between one and ten (10) depending on the mission and platform. To keep cost low, the architecture is modular and distributed in order that the largest number of platforms and missions could be accommodated with a minimum of customization (Figure 1).

From discussions with our customers, partners, and government technical officers, we have developed the following CA requirements. Some of the requirements are qualified by UAS class:

- Must be capable of providing CA and situation awareness (Air-Air) along the aircraft vertical  $\pm 15^\circ$  and the azimuth according to UAS classification.
  - Tier II+ (Predator/Global Hawk) - up to 360°, but more probably  $\pm 110^\circ$



- Tier II (ScanEagle) -  $\pm 110^\circ$
- Tier I (Raven) -  $50^\circ$
- Must operate 24/7 and be passive.
- Sensitivity: Detect a Cessna type object closing at 250knots with >90% probability at limits of detection (nominal).
- Detectability:
  - Tier II+ - 4km, 30s,  $\Delta 30^\circ$ F, MLS, 90% (nominal)
  - Tier II – 3km
  - Tier I – 2km
- For Tier II/II+ - Must be capable of interfacing with TCAS and ADS-B (future).
- First generation system must be MITL and provide the ground operator with the following information:
  - Coordinate locations of objects of interest,
  - Object prioritization,
  - Thresholds declaration.
- Future systems, as funding becomes available will add progressively more functionality to meet JIPT requirements,
  - Airspace situational awareness,
  - Autonomous maneuver and avoid,
  - Passive Ranging,
  - Separation assurance around Class B,C,D (airports etc)
  - Air-Ground, Ground-Ground, Ground-Air,
  - All Weather and man made hazards,
- Provide see and avoid capability equal to or better than current FAA requirements for 14CFR Part 91.113 Right of Way Rules
- Must be retrofittable and customizable so as to fit into the broadest grouping of both civilian & military aircraft covering the categories of UASs, rotorcraft, and fixed wing aircraft.
- Must comply with MIL-STD-810F for shock, vibration, drop, immersion, and temperature and MIL-STD-461/462 for EMI. All relevant FAA, military, aerospace specs. as required.
- Meet all required Reliability/Serviceability Standards as defined by the DoD and FAA.

### 1.3 Technical Approach

A pilot gauges a collision threat by analyzing its size, rate of change (extent and/or intensity), and track. Instinctively, these factors are prioritized and set to thresholds, once a threshold is breached, corrective action is taken.

There are several operating assumptions or scenarios that can be useful in understanding the operation of aircraft and the requirements of a CA system:

In the NAS there are two (2) types of traffic: cooperative and non-cooperative while in the battlefield all traffic is assumed to be non-cooperative. Cooperative traffic broadcasts its position using a transponder (TCAS or ADS-B future). Non-cooperative traffic does not.

Additionally, according to 14 CFR Part 91, aircraft that operate below 250 knots must remain below 10,000 feet and any aircraft flying above 10,000 feet must have a transponder. Therefore in the NAS, fast aircraft only fly >250 knots above 10,000 feet, allowing a TCAS enabled system to provide the additional detection range (Table 2). In the battlefield, the condition of lower and slower still applies but, is not universally true.

Above 18,000 feet aircraft (Class A) are required to fly under IFR (instrument flight rules) and be under ATC (air traffic control). Therefore, theoretically, when operating under IFR, compliant aircraft will not collide. However, several mid air collisions have taken place when aircraft are not compliant such as the [Tu-154 /DHL](#) mid air collision and the [AIR RAGE](#) Airbus mid air collision.

The two (2) examples highlighted above demonstrate the need a need for a platform centric CA technology over and above the existing implementations of TCAS, ADS-B and ATC in Class A airspace.

MilSys' approach is to mimic a pilot's analytical approach with a technological solution. Simply speaking, the system operates as a hot spot detector and corrective action must be taken when an object breaches a threshold and remains stationary in the field of view. Proprietary models, algorithms and methods are being developed to sense, detect, cluster, discriminate and threshold objects of interest (See Sections 5). Thresholds will be determined by the altitude, speed, external temperature, atmosphere/weather etc. based on the platform and its mission profiles. This approach can meet the SAA requirements for both civilian and military aircraft.

The process to avoid collision can be broken into three (3) distinct phases; detection and tracking, path planning, and maneuvering. Detection and tracking is the period of time between the initial breaching of a threshold and the determination of its track. Path planning, in a MITL system, is a function of the speed of the up/downlink and response of the ground controllers. In a UAS with autonomous avoidance guidance path planning would be the time to determine a de-confliction plan. The time to maneuver is a function primarily of the UAS bank angle.

Altitude	Table 2: Factors effecting collision times
>17,000	In the NAS, operating in Class A, ATC controlled airspace
Low <10,000ft	Lower Airspeeds <250knots Lower Temperatures Differentials (< $\Delta^{\circ}\text{F}$ ) Smaller objects More atmospheric absorption (> $\alpha$ ) No TCAS
High >10,000ft	Higher Airspeeds >250knots Higher Temperature Differentials (> $\Delta^{\circ}\text{F}$ ) Less atmospheric absorption (< $\alpha$ ) Larger objects TCAS (NAS only)

Nominally, the UAS of the Predator Class will take  $\approx 11$  seconds to maneuver 500ft at a bank angle of  $18^{\circ}$  independent of speed. In smaller Tier I UAS the time could be as short as 5 seconds. Independent of the platform, the detection and tracking of objects will be in the range of 2-5 seconds. All of these times are generally fixed, with the caveat that the UAS could maneuver faster if it increased its bank angle. The gating factor is the MITL which has been specified by UAS manufacturers as 15 seconds. From a systems perspective, the goal is to minimize MITL delays while providing the maximum amount of detection and tracking time. The object's slant range to the UAS is a key factor in maximizing the MITL time. Front on approaches will have a much shorter MITL time than side on. Overall, this sets the detection time to be 32 seconds out for the larger Tier II+ UASs and as short as 10 seconds for Tier I.

Currently under the statement of work for the BAA, PCAS is a MITL system for Predator Class UASs. As funding becomes available, and as the regulations, standards and technology progress', its MilSys' intention to integrate additional amounts of autonomy. This path may be as follows: MITL, autonomous path planning and recommend maneuvering, independent emergency action, limited autonomy, and full autonomy.

Discussions with the smaller Tier I and Tier II manufacturers and government program managers indicated a need and desire to move more quickly to autonomous path planning and maneuvering. The operational plan would be to be under MITL control for Class B,C,D airspace on landing, takeoff and when transiting. However, when in Class E airspace during transit and on station the UAS would operate under full autonomy. The rational being that >99.99% of the time this airspace is completely void of any traffic.

## 1.4 Operational

The PCAS architecture has been designed from the ground up to be SWAP and cost efficient, as well as modular and highly flexible in order to meet the requirements, both new and a retrofit, of most aircraft (UAS, manned fixed wing and rotorcraft) on the market today. It consists of two (2) hardware components: sensors and a track processor (TP). To reduce development time, costs, and program risk, both the sensors and TP will be based on COTS or modified COTS components.

The sensors will operate as independent self contained units having hardware/software/firmware for image stabilization (IMU), control, communication, an IR (or visible as required) camera with lens, and proprietary sense, detect and threshold algorithms. The algorithms will be based on LMS type filtering (5.1) not optical flow. Optical flow being determined as to processor intensive for this type of system. The FOV would be tailored depending on sensor location, UAS class and mission profile, with the front sensor having the smallest FOV and in the rear the largest. One proposed configuration is  $\approx 20^\circ$  at the nose,  $50^\circ$  at the wing tips and  $>100^\circ$  at the rear. They will be “plug and play” with the TP allowing easy customization.

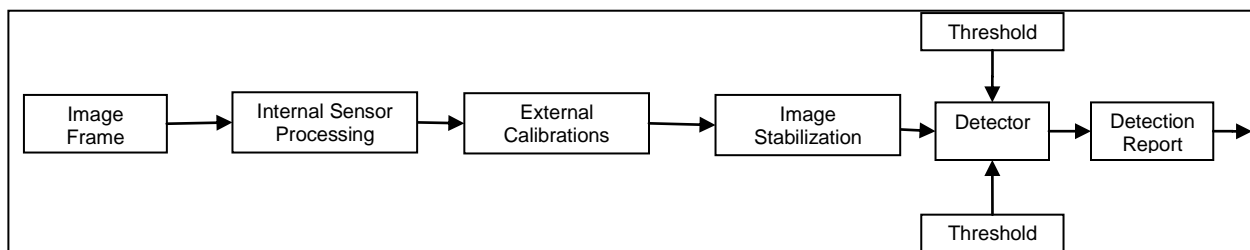


**Figure 2: Flow diagram of the image through the sensor.**

The image captured by the lens and FPA (Figure 2) will be processed by the internal DSP/FPGA and firmware to correct for internal calibration errors, normalization, dead pixel removal etc. The DSP/FPGA will then perform an external calibration (as required) and stabilize the image as required from information provided by the IMU. This processed image will then be passed through the detector and threshold algorithms. As required, detection reports (Figure 3) will be produced and communicated with TP. The image will then be discarded.

The central brain (i.e. TP) will be the locus of the system (Figure 1). It will control and communicate with the sensors, the autopilot, the operator (pilot or ground control) and the aircraft. It will receive detection reports, inputs from TCAS, INS, and other relevant data from the aircraft or ground control.

Proprietary algorithms (See 5) will translate detection reports

into tracks to be monitored, prioritized and set to thresholds (Figure 4). MITL or autonomous algorithms will make the appropriate decisions and control the aircraft to avoid any threat conditions.

A proposed configuration for the Predator, with five (5) sensors and TP, will have a SWAP of nominally 30Watts, <8lbs, and <0.1 cubic feet.

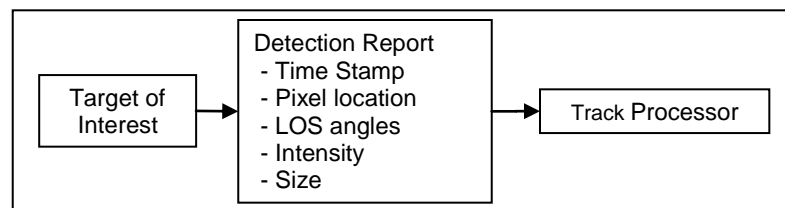


**Figure 3: Example of a detection report.**

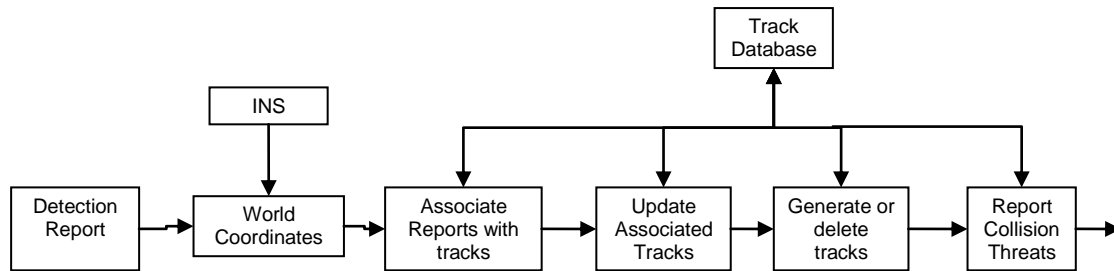


Figure 4: Block diagram of some of the processing algorithms.

## 2 System Modeling

A system model which will allow the prediction of range performance based on system design inputs, target geometries, thermal profiles and operating environmental conditions was developed by [Magnolia Optical](#) under the leadership of Dr. Ashok Sood. The model is designed to answer this type of question: Given a microbolometer with an f/1 optics, 25mm diameter, 17um pixel, etc. operating at mid latitude summer (MLS) at what range will it have a 50% probability of detecting a Cessna type target (4m<sup>2</sup>, Δ30°F) The validity of the data will be compared against NVTherm2002 and NVThermIP, as well as data collected in the field. Many of the microbolometer manufactures have contributed their actual production line data for comparison.

### 2.1 Bolometer sensor model(s) overview

#### 2.1.1 Excel model for single detector pixel performance prediction

This excel model was created to provide accurate estimations of bolometer array performance parameters, notably NETD and MRTD, for the many types of devices currently in production. Inputs include basic materials properties for the bolometric material, the absorber layer if used, the metallizations, and the structure of the pixel (table and leg structure). Electrical resistances, TCR's, heat capacitances and thermal conductances are calculated and are used to predict the time constant, the response and the NETD of the device. Inputs also include the optical system and the biasing and readout characteristics. Performance results can be seen in Figure 5, and optics, scene and electronics inputs are shown in Figure 6. The excel sheet is set up to easily allow inputs for three VOx manufacturers' and the alpha-silicon manufacturers' devices (Figure 9). NETD's here are calculated for the four major noise sources (Johnson noise, thermal fluctuation noise, 1/f noise and read noise).

Vn Resp	type	Vn	NEP	NETD hbe	In (RI)	NEFD	Vn sw	NETD sw	NETD RG
2.71E-12	thermal fluc	2.42E-06	2.40E-12	26.5	9.67E-15	1.21E+08	2.42E-06	23.5	23.5
5.45E-17	backgd fluc	4.87E-11	5.53E-13	5.4	1.95E-19	2.78E+07	4.87E-11	5.4	0.0
6.39E-12	johnson	5.71E-06	7.96E-12	62.7	2.28E-14	4.00E+08	5.71E-06	56.2	55.5
4.94E-12	1/f temporal	4.41E-06	6.05E-12	48.4	1.76E-14	3.04E+08	4.41E-06	42.9	42.9
8.40E-13	readout	7.50E-07	8.40E-13	8.2	3.00E-15	4.22E+07	7.50E-07	3.6	7.3

Figure 5: Excel performance chart

<b>scene</b>			<b>Electronics (readouts, sample rates, noise bandwidths)</b>				
T bk	298 K		full frame (1) for aSi or (2) for VOX				
larn hi, low (um)	12	8.0	N rows/cols 120 for int				
W	1.17E-02 W/cm2		rate Hz	time sec	del f		
dW/dT	1.92E-04 W/cm2-K		30	0.0333	15		
delta Ts	0.1 K		frame				
	baseline	new	sample				
T subst	298	298	1 integrate vox	3.60E+03	2.78E-04	1	port of time
T opt	298	298	1 integrate asi	31.6	0.0317	0.95	
T scene	298	298.1	4 calibration	1.23E-04	2040	34 minutes	
T dewar	298	298	4 tc thermal	33.0	0.0076		
			effective	33.0			
			rate Hz	sec	msec	usec	
			thermal t ro allowed	55.0	1.82E-02	18.17	tframe lim by thermal time
			ro array t ro allowed	3.60E+03	2.78E-04	0.28	tframe lim by #rows read
			f eff	3.600E+03	Hz		
			f used	3.158E+01	Hz		
			t used	1.58E-02	sec	15833.3	usec
				15.833	msec		
<b>optics</b>			<b>electronics</b>				
D opt	10 cm		choose	1	1=const	2=const	V
A opt	79 cm2		frame rate	30	0.0333		
eta opt	0.72		del f	15	0.0667		
f/#	1.00		t frame	16.7	msec		
eratio	0.0001		I bias pulse	1.00E-08	amps		load line expression
tau opt	1.00		pulse time	1.58E-02	sec		beta 0.02
foclen	10 cm		pulses/frame	1			f(beta) 1.00
det IFOV	2.00E-04	rad	I bias power	4.75E-09	amps		
diff IFOV	2.44E-04	rad	V bias total	5	volts		
diff spot	24.4	um	N tdi	4			
solid angle	0.211	0.250	ah/n	4.00E-29	norm hooge		
hor FOV	11.73	deg					
vert FOV	8.80	deg					

**Figure 6: Scene, optics and electronics inputs**

Shown are the noise voltages, the NEP, the NETD calculated from the heat balance equation, the current noise, the noise equivalent flux density, the noise voltage calculated from a variety of expressions found in literature sources<sup>vi-x</sup>. Figure 5 shows that near exact NETD agreement was accomplished from three independent equations and methods (NETDsw, NETDrg, and NETDhbe)<sup>xi-xv</sup>. The slightly higher NETD's from the heat balance equation (NETDhbe) are probably closer to reality than those predicted purely from equations as the response used in most equations is an approximation and assumes that the thermal leg conductance is much greater than the radiative conductance.

### 2.1.2 Imaging matlab model for aggregate pixel (FPA and sensor) performance prediction

A model in matlab for the generation of dynamic image sequences was developed to help assess and characterize sensors and cameras by providing images of bar targets in user-controlled noise backgrounds. This model is used to simulate dynamic bar target (NETD and MRTD) tests. The model generated bar target images of user-defined delta temperature and size are shown at 30Hz as in an actual test with a physical bar target, collimator, display and human eye. Temporal and spatial noise can be added by the user, the bars can be blurred by the diffraction PSF or a user-defined Gaussian PSF, and are displayed in real-time. The images are first constructed at super-resolution (8x to 32x), convolved with a super-resolution PSF then binned down to the FPA format of interest. Initial results (observer MRTD's) are much lower at the lower spatial frequencies than the NETD values and these MRTD plots agree with the NVThermIP run outputs. Older MRTD equations tend to overestimate the MRTD as does NVTherm2002. MRTD(f) will be an important parameter in calculating probabilities of detection, identification and recognition. For bar target spatial frequencies that approach the detector spatial frequency (Nyquist), large variation in MRTD is a result of aliasing. Placement of the bars in exact alignment gives the lowest MRTD; however, in reality this is almost never the case. As the spatial frequency approaches  $1/(2 \cdot \theta_{det})$ , bar location becomes more important and large variations in MRTD are seen for just small changes (portion of a detector pixel) in bar position.

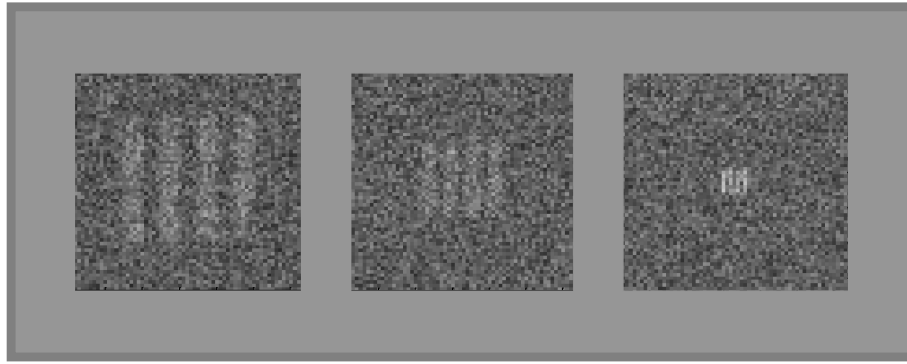


Figure 7: Simulated bar target images from the matlab program

These simulated MRTD's and MRTD's calculated by NVTherm or from NVTherm expressions will be used to predict the N50 spatial frequency and range and the corresponding identification and recognition probabilities and ranges in section 2.3.3.

### 2.1.3 Capacity for sequential vendor model inputs and fair comparison

The model has been adapted to get fast and accurate results for the four manufacturers' bolometers. The user can switch between the four by simply choosing a number from 1 to 5 in the "choices" cell shown in Figure 8. Once the sheet is populated by vendor's specifications or our best approximations, comparisons of bolometer arrays in identical optics and for identical operating conditions can be accomplished. Here the model may also be used for performance optimization since we have knowledge of all the noise sources and the response. Bias voltage, sample time, operating temperature can all be varied as well as the characteristics of the bolometer.

bolo setup		5	1 is L3	2 is RVS	3 is DRS	4 is BAE	5 is generic			
Needed for C and G and tau										
bolometer element - geometry										
		L3 aSi	RVS vox	DRS vox	BAE vox	generic	in use			
	D unit cell	20	20	17	17	28	28	um		
	Xpix SiN	18	19	16	16	24	24	um		
	Ypix SiN	15.5	19	12	13.5	20	20	um		
	X format	1024	640	640	640	320	320			
	Y format	768	480	480	480	320	320			
bolo pix 2.40E-17	Dim bolomaterial	18	19	16	16	24	24	um		
	VOX or aSi	15.5	19	12	13.5	20	20	um		
		0.075			0.05	0.05	0.05	um		
	absorber length	0	19	16	16	0	0	um		
	absorber width	0	18	15	15	0	0	um		
	absorber thickness	0	0.1	0.1	0.1	0	0	um		
	SiN support thick	0.23	0.23	0.23	0.4	0.23	0.23	um		
	additional layer thick	0	0.5	0.5	0.05	0.5	0.5	um		
	metal area	10			11	12	12	um <sup>2</sup>		
	metal thickness	0.05			0.05	0.05	0.05	um		
bolo legs	fill factor	0.70	0.90	0.85	0.75	0.61	0.61			
	SiN leg length	15	17	17	30	18	18	um		
	thickness	1		0.2	0.5	2	2	um		
	width	1.00	1.75	1.75	1.00	2.20	2.2	um		
	# of legs	2	2	2	2	2	2			
	Dim metal	15	17	17	30	18	18	um		
		0.5	2	2	2	0.34	0.34	um		
		0.03	0.05	0.05	0.05	0.05	0.05	um		
	perform									
	C							1.17E-09	J/K	
G							1.02E-07	W/K		
tau response		7.9	10				11.5	msec		
NETD		29	20		28		51.5	mK		
NETD hbe							#DIV 0!	mK		
response							9.77E+04	V/V		
response hbe							0.00E+00	V/V		

bolometer element - electrical									
		L3 aSi	RVS vox	DRS vox	BAE vox	generic	in use		
1/2tsamp	Rb (ohms)	2.50E+08				2.00E+04	2.60E+04	2.60E+04	ohms
	TCR	0.0285	0.024			0.025	0.02	0.02	
	Rload (ohms)	2.50E+08	0.00E+00	0.00E+00		2.00E+04	2.60E+04	2.60E+04	ohms
	absorb full spec	0.55	0.55	0.55		0.55	0.40	0.40	
	absorb inband	0.9	0.80			0.85	0.90	0.85	
	a hooge	4.00E-29				4.00E-29	4.00E-29	4.00E-29	m-3
	k 1/f	6.00E-12	1.00E-13	1.00E-13		4.00E-13	1.00E-13	1.00E-13	
	or 1/f noise						22	22	mK
	Vbias on bolo	5	2.33	2.3		3	2	2	v
	pulse duration	31.67	2.78E-04	2.78E-04		2.78E-04	6.90E-02	6.90E-02	msec
	pulses/frame	1	1	1		1	1	1	
	sample time	31.67	2.78E-04	2.78E-04		2.78E-04	6.90E-02	6.90E-02	msec
	noise bandwidth	15.79	1.80E+06	1.80E+06		1.80E+06	100	100	Hz
	frame rate	30.00	30	30		30	30	30	Hz
	frame time	33.33	33.33	33.33		33.33	33.33	33.33	msec
	band pass hi	12	14	12		14	14	14	um
	band pass low	8	8	8		8	8	8	um
	readout noise						10	10	mK
	resid spatial noise	10					10	10	mK

Figure 8: bolometer choice section

Figure 8: bolometer choice section

### 2.1.4 Iterative heat balance equation and comparison to approximations often used

For a more realistic representation and to assure that thermal runaway is not occurring at the biases applied, the heat balance equation is solved for the baseline conditions (no target), and the new conditions (target on a pixel). The model iterative solves for these conditions, finds the

bolometer temperatures, calculates resistances and currents, signal to noise, and NETD. The model supplies a user-defined target temperature. Here it was set at 1K above ambient. The model calculates the signal and the signal to noise. This is then divided into the delta T value to get the NETD. These values have corresponded closely to the purely equation derived NETD's but show consistently higher NETD's due to the lower response calculated from the heat balance equation. This lower response (generally 10-20% lower) is expected to be closer to reality than the response approximation usually used which does not consider the effects from radiative loss, only from the leg conductance. For higher leg conductance to radiative conductance ratios, the responses become equal. The SNR and computed NETD from the heat balance equation were found to be in close agreement with the theoretical models (equations) for a large variety of bolometer characteristics.

HEAT BALANCE - baseline				0.50		baseline measured values		
elect in	5.64E-09	3.418E-08	del Power	T subst	298	delta T	I bolo	1.0122E-08 amps
P scene	6.20E-09		2.77E-15	T bolom	298.8573	0.8573	V bolo	2.4695 volts
P nonscene	2.23E-08		0.000%				Rbolo	2.4397E+08 ohms
rad	2.60E-09	3.418E-08		set accuracy	in mK	delta T	delta I bol	3.67E-14 amps
cond leg	3.03E-08			1.00E-17	0.3	0.0003	delta V bol	-9.18E-06 volts
cond vacuum	1.29E-09							
HEAT BALANCE - new				0.50		new measured values		
elect in	5.64E-09	3.419E-08	del Power	T subst	298	delta T	I bolo	1.0122E-08 amps
P scene	6.21E-09		3.25E-15	T bolom	298.8575	0.8575	V bolo	2.4695 volts
P nonscene	2.23E-08		0.000%				R bolo new	2.4396E+08 ohms
rad	2.60E-09	3.419E-08					del Rbolo	-1791 ohms
cond leg	3.03E-08			del phi	1.08E-11	watt		-17.91 ohms/mK
cond vacuum	1.292E-09			V signal	9.66E-06	volt		

Figure 9: Heat balance equations

## 2.2 Sensor systems model and evaluation criteria

### 2.2.1 Mathematical basis for model: NETD, NEP, MTF, CTF, and MRTD equations compiled and derived from literature and from NVTherm models

**NETD and NEP derivations:** The bolometer NETD consists of contributions from background temperature fluctuation, bolometer temperature fluctuation, electrical current Johnson noise, bolometer 1/f noise and readout noise. The NETD in relation to the NEP, response and D-star is:

$$NETD = NEP \frac{4F^2}{\tau_o A_d [dM / dT]_{\Delta\lambda}} = \frac{V_n}{\mathfrak{R}_v} \frac{4F^2}{\tau_o A_d [dM / dT]_{\Delta\lambda}} = \frac{4F^2}{\tau_o A_d^{1/2} [dM / dT]_{\Delta\lambda}} \frac{\sqrt{\Delta f}}{D^*}$$

where F is the optics f/number, and dM/dT is the spectral radiance contrast of the scene evaluated over the spectral band

The NETD components are:

NETD Johnson:  $NETD_j = \left[ \frac{G}{\alpha_{icr} V_{bias}} \right] [4kTR_b (f_2 - f_1) f(\beta)]^{1/2} \left[ \frac{4F^2}{A_d \epsilon_{ib} \tau_o dM / dT} \right]$

NETD 1/f:  $NETD_{1/f} = \left[ \frac{G}{\alpha_{icr}} \right] [k_1 \ln(f_2 / f_1)]^{1/2} \left[ \frac{4F^2}{A_d \epsilon_{ib} \tau_o dM / dT} \right]$

NETD thermal fluct:  $NETD_{ff} = [4kT^2 G f_{eff}]^{1/2} \left[ \frac{4F^2}{A_d \epsilon_{ib} \tau_o dM / dT} \right] \quad f_{eff} = \min[f_{bol}, f_{read}]$



NETD background fluct: 
$$NETD_{bf} = \left[ \frac{8\epsilon\sigma k(T_b^5 + T_d^5)A_d\Delta f}{\alpha_{icr}} \right]^{1/2} \left[ \frac{4F^2}{A_d\epsilon_{ib}\tau_o dM / dT} \right] \quad (\text{negligible})$$

Note that NETD varies strongly with two commonly varied parameters, the f-number and the background temperature (and temperature contrast  $dM/dT$ ). NETD improves with slower optics as shown in Figure 10a. NETD degrades at cooler background temperatures (tracking with the spectral radiant contrast) as shown in Figure 10b. This NETD degradation (increase) observing cool scenes can, in part, be compensated for as bolometer noise may improve and response (TCR) may increase. L-3 has claimed improved performance for a-Si operating at below ambient temperatures. They report about a 2x improvement in NETD from 300K to 220K operation due mostly to an increase in TCR and resistance.

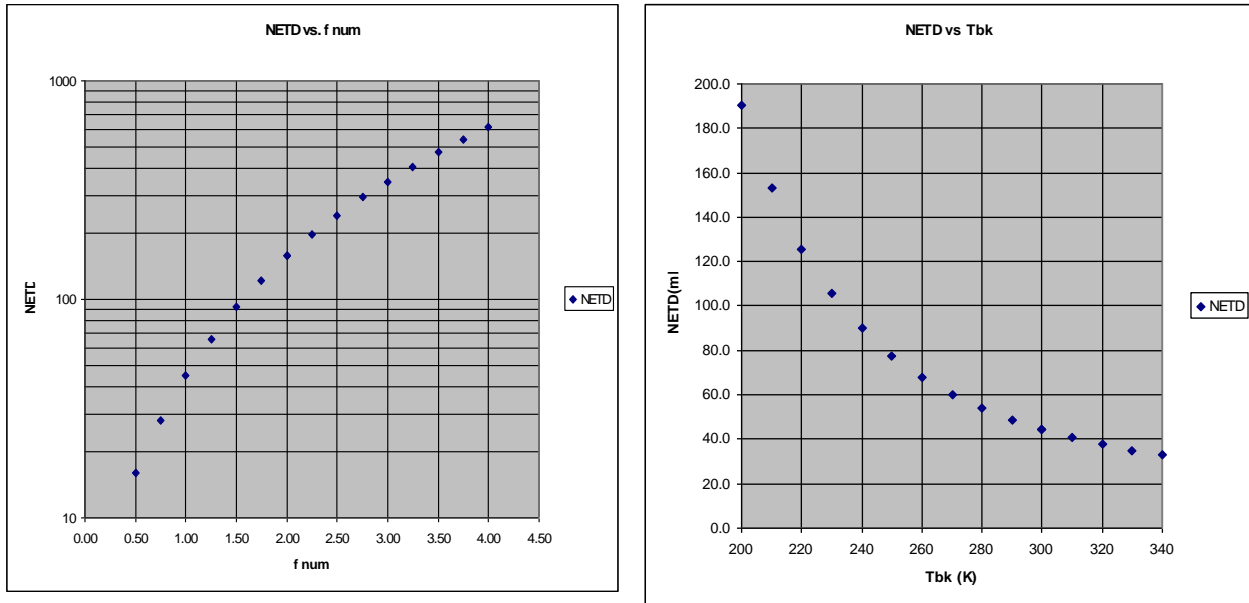
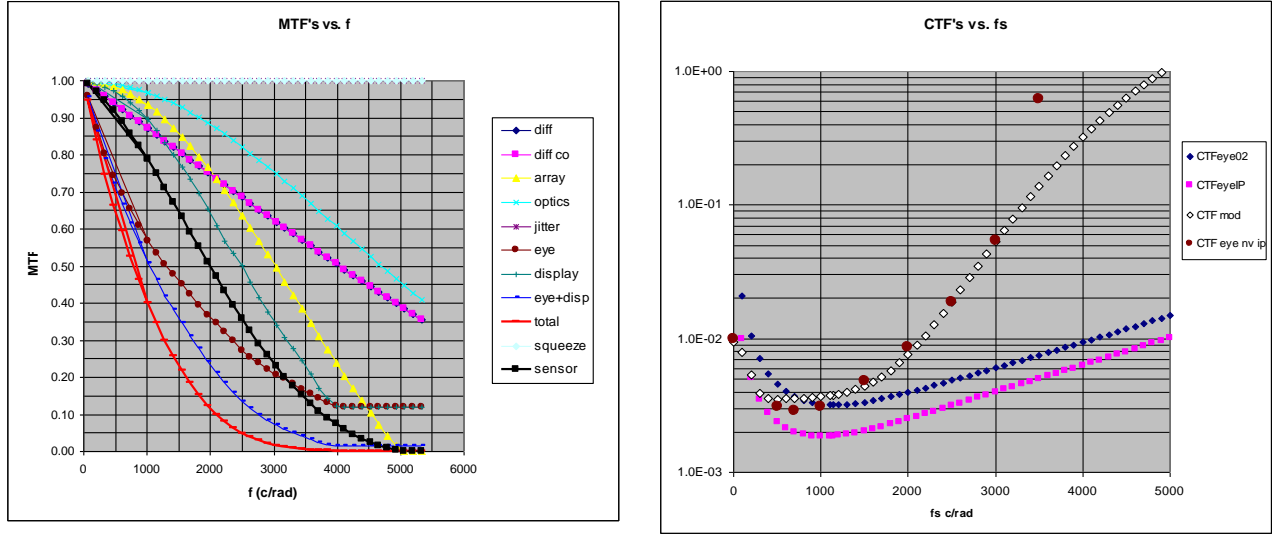


Figure 10: NETD as a function of f-number (left) and of scene temperature (right)

NETD and MRTD are the commonly used metrics for extended resolved target evaluation; however, for subpixel targets the NEP and NEI are used.

**MTF's and CTF's:** MTF's used in the model include the diffraction MTF, the detector spatial sample MTF, the eye MTF (used in some expressions), and the squeeze or spurious response MTF. These have been compared to the MTF expressions used in both NVTherm models and are identical as are the output plots. Shown in Figure 11a are these and some of the additional MTF types.





**Figure 11: MTF's vs. spatial frequency**

**CTF system and CTF eye:** The contrast threshold function is related to the MRTD ( $CTF = MRTD / (2 \cdot Stmp)$ ), where  $Stmp$  is the scene temperature contrast. The  $Stmp$  default value in NVTherm is 4C which is the value used in my excel and matlab model runs. The CTF plots in Figure 11b are from the eye CTF equations given in the NVTherm2002 and NVTherm IP manuals.

### 2.2.2 System level analysis (bar target imaging and MRTD prediction)

About a dozen different MRTD expressions were found in the literature dating back to the early 1980's. Past expressions were not found to be accurate over the entire spatial frequency range. Some of these have been incorporated into the model and the user may choose which to use. Plots from these expressions are shown in Figure 12 and Figure 14 along with NVTherm IP run results and a visual assessment of matlab simulated images shown to the observer at 30 Hz. Expressions are from the Ratches and Lloyd papers, and the two latest versions of NVTherm<sup>xvi-xix</sup>.

The Lloyd expression which gives a pretty good fit in the mid-range spatial frequencies is:

$$MRTD = \frac{SNRt}{1.51} \left(\frac{4}{\pi}\right)^2 \frac{NETD}{H_f} \theta_{det} f_s \quad \text{where } SNRt=2.25$$

Adding the second constant term to the expression improves the low frequency accuracy. This constant corresponds to the eye and display contrast limitations.

$$MRTD = \left[ \left\{ \frac{SNRt}{1.51} \left(\frac{4}{\pi}\right)^2 \frac{NETD}{H_f} \theta_{det} f_s \right\}^2 + \{MRTD_{ed}\}^2 \right]^{1/2}$$

The MRTD NVTherm2002 expression given in the manual is:

$$MRTD(f_s) = \frac{CTF_{eye}}{M_d H_f} \left\{ \left[ \frac{K_{eye} F_{\#} \pi}{(dL/dT) D_{pk}^* \tau_o f (2t_e t_i / t_f)^{1/2}} \frac{(B_w B_L)^{1/2}}{S_L} f_s \right]^2 + \frac{4S_{tmp}^2}{G^2} \right\}^{1/2}$$

where  $M_d$  is the magnification of display,  $H_f$  is the combined MTF,  $dL/dT$  is the scene spectral radiant contrast,  $G$  is the display gain,  $K_{eye}=823$ ,  $(B_w B_L)^{1/2}/S_L$  is the eye filter response

Substituting for the D-star to get the expression in terms of NETD we get:

$$MRTD(f_s) = \frac{CTF_{eye}}{M_d H_f} \left\{ \left[ \frac{\pi^2 (B_w B_L)^{1/2}}{4 S_L} K_{eye} \left( \frac{t_f}{t_e} \right)^{1/2} NETD \theta_{det} f_s \right]^2 + \frac{4S_{mp}^2}{G^2} \right\}^{1/2}$$

The MRTD from NVTherm IP is: 
$$MRTD(f_s) = \frac{CTF_{eye}}{M_d H_f} \left\{ [2\alpha \Gamma_{det} \frac{(B_w B_L)^{1/2}}{S_L}]^2 + \frac{4S_{mp}^2}{G^2} \right\}^{1/2}$$

where 
$$\Gamma_{det} = \frac{4F_{\#}^2}{\pi \tau_o f (dL/dT) D_{pk}^* (t_i t_e / t_f)^{1/2}}$$

and in terms of NETD is: 
$$MRTD(f_s) = \frac{CTF_{eye}}{M_d H_f} \left\{ [2\sqrt{2}\alpha \frac{(B_w B_L)^{1/2}}{S_L} \left( \frac{t_f}{t_e} \right)^{1/2} NETD \theta_{det}]^2 + \frac{4S_{mp}^2}{G^2} \right\}^{1/2}$$

This last expression and the Lloyd expression give the best MRTD fits to data (simulated bar target images) and with the results from NVTherm IP runs. These results are described more fully in the model validation section. These equations were used in the excel model and images were generated in an identical matlab version of the model to generate realistic bar targets with temporal noise. These images were compared to MRTD predictions from this excel model and to NVTherm outputs. Some representative images and MRTD's curves are shown in Figure 12 and Figure 14.

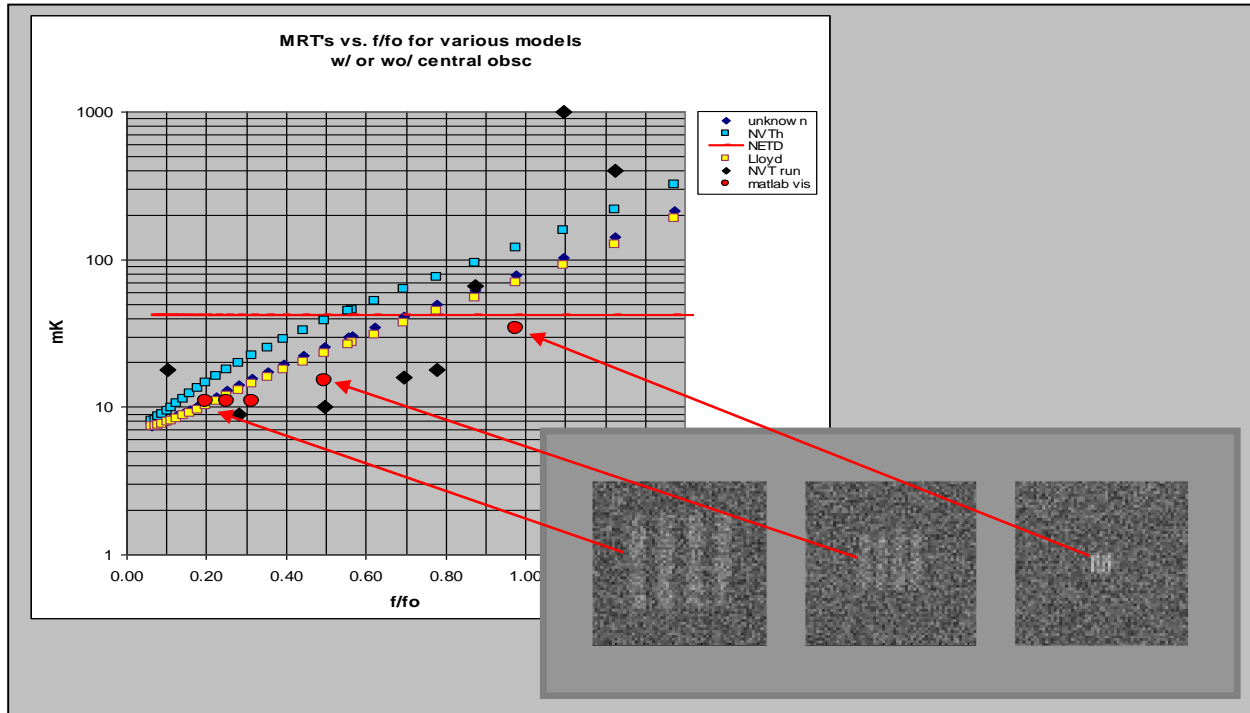


**Figure 12: MRTD's from theory (top blue and yellow), from NVTherm IP runs (black diamonds), and discerned from matlab image sequences shown at 30Hz (red circles); three images at 1.25\*NETD bar target temperature and summed over the eye integration time are shown at bottom right.**

## 2.2.3 MTF, CTF, target temperature contrast and probabilities of detection, recognition and identification

In addition to the NETD, the MTF and CTF are critical parameters in predicting MRTD. The main components of the MTF are from optics diffraction, detector sampling and aliasing. The CTF is determined from the human eye and the display characteristics such as the display brightness and magnification and the human eye's response to light level and spatial frequency. MTF's and CTF's are shown in Figure 13 for a typical LWIR f/1 bolometer based sensor. The sheet consists of the target section, the probabilities section, the MRTD sections, and the MTF section. Other parameters of interest include the D-star, the NEP, the CTF's and the SNR where the SNR is calculated for the target specified in the target section and the atmosphere (radiance and transmittance) specified for the range and altitude.

ID det sample		1786 from IFOV	Nyquist		atmosphere		Eye and Display	
NL(/rad)		9091 D / lam			range		rho	
N (/rad)		1350	c/deg		abs coeff		Mag hor	
N (/mrad)		1.35	30 F		tau atm (range)		Dpupil	
			16.7 C		0.995		fo	
							io	
target				for NVTh MRTD		for starers		
Dhor, Dvert		2	2 meters		(f) BW		MTF's	
radh, radv		2.00	2.00 mradian		(f) BL(phi)		MTF diffraction	
IFOVh, IFOVv		0.28	0.28 mradian		SNRth 2002		MTF opt design	
tar sub pixels		7.14	7.14 t/fo		Keye		MTF gauss	
target dT		45 mK			SNRth IP		MTF atmos	
dT at range		44 mK			alpha		MTF array	
tar mean (K)		300.04	bk mean (K)		Mdisplay		MTF sig proc	
em tar		1	e bk		CTFeYE IP		MTF display	
tar sigma (K)		0	tau atm		CTFeYE 2002		MTF eye	
tar rss (K)		0.04	NEI watts		CTF modeled		MTF det tc	
tar app rss (K)		0.04	SNR		CTF used		MTF jitter	
tar contrast		0.01	set T bk and e bk for altitude		Dstar pk		MTF turb	
target as IFOV		2.00E-03	altitude (km)		srcon		MTF int hold	
det IFOV		2.80E-04	trans (8-14um)		tauopt		MTF sensor blue	
target rel size		7.14	T eff (K)		SL		MTF squeeze	
target is resolved >>>		look at NETD		Stemp		MTF total - bold		
				MRT base level				
Probabilities		V50	R50	E ip	Probs	Lloyd, unk		
num bar for search		2.7	0.75	1.6	0.24	stmp term mks		
for recog		14.5	3	1.5	0.03	42.9		
for ID		18.8	6	1.5	0.02	turn off stmp		
fs(range)		1350 c/rad	w deg	3.85	f det (c/rad)	0		
		1.35 c/mrad	L cd/m2	17.13	f det (c/mrad)			
Nsample		1000 c/rad	num	535.69	f diff (c/rad)			
N50 hor		3.38 c/mrad	denom	1.33	f diff (c/mrad)			
N50 vert		0.04 c/mrad	a	403.08	DEL det			
N50		2.5 km	b	0.40				
TTPF		0.03	CTFeYE2002	3.67E-03	c/deg			
			CTFeYE2002	2.10E-04	c/mrad			

Figure 13: Main sheet for sensor performance evaluation

## 2.3 Model validation

### 2.3.1 NETD comparisons to literature and other model results

Expressions from a variety of models for the noise and NETD were found in the literature. The expressions from the various sources were slightly different. Each set of equations had some shortcomings or approximations that were explored. More accurate expressions for the optical throughput and for the response were developed. For example, a common expression for the optical throughput involves the expression  $4F^2$  or  $4F^2+1$ . An exact expression was found whose solutions lie between the values from these two expressions.

The scene solid angle is derived from: 
$$\Omega = 2\pi - \frac{2\pi}{\sqrt{1+1/(4F^2)}}$$

The model is in agreement with three independent models (expressions and outputs) for noise and NETD. For the NETD calculations, two responses were used, the heat balance equation response and the thermal leg conductance response.

The heat balance equation response is:  $\Re_{hbe} = (V_{bo}' - V_{bo}) / (P_{sc}' - P_{sc})$

The leg conductance approximation is:  $\Re_G = \frac{\alpha_{icr} V_b}{G} \frac{R_b R_L}{(R_b + R_L)^2}$

The approximation overestimates the response by about 10% and underestimates the NETD also by 10% for these f/1 microbolometer cases.

### 2.3.2 MTF and MRTD comparisons to NVTherm2002 and NVTherm IP

In general, the MRTD is equal to the NETD\*k<sub>2</sub> / MTF. The constant k<sub>2</sub> actually has a frequency dependence that slightly increases the MRTD at the lower spatial frequencies. In NVThermIP, the contrast transfer function (CTF) includes this dependency as can be seen in the NVThermIP data points in Figure 14. The MRTD plot from the new NVThermIP CTF expression agrees well with the matlab image evaluations. The MRTD plot and the target effective temperature are used in NVTherm2002 to find the N50 point (target spatial size where the probabilities of detection /recognition /identification are 50%). NVTherm IP uses the system CTF and the target temperature contrast to find the N50 point (renamed in NVTherm IP as the V50 point). These are just the previous NVTherm2002 parameters divided by 2\*Stmp, where Stmp is the scene temperature contrast which is assumed in these simulations to be 4C. The MTF's currently used in the model include diffraction, detector shape, display, and eye MTF's as shown in Figure 12a. For the MRTD calculation, the NVTherm2002 model used the system MTF which included the eye MTF and a constant (SNRt). The newer version uses the system CTF and the system MTF, but without the eye MTF. For this 47mK NETD bolometer, the MRTD is seen to reach a minimum of about 16mK in the 0.40-0.60 c/mrad spatial frequency range as predicted by NVTherm IP (red diamonds). This matches the 14mK MRTD discerned from the 30Hz matlab simulated images (green squares). The difference between the plots modeled in the excel program and the data plots (NVTherm run outputs and visual MRTD data) occurs because of differences in the eye CTF curves used and the positive effects of aliasing which improve the actual MRTD at the higher frequencies. The excel model MRTD's do not currently provide for spurious response and for the case where the bars are perfectly aligned with the detector pixels (0 degree phase case). When considering these factors, the MRTD is actually fairly flat until the spatial frequency approaches the Nyquist frequency. The model which uses the eye CTF expression alone overestimates the MRTD at high spatial frequencies.

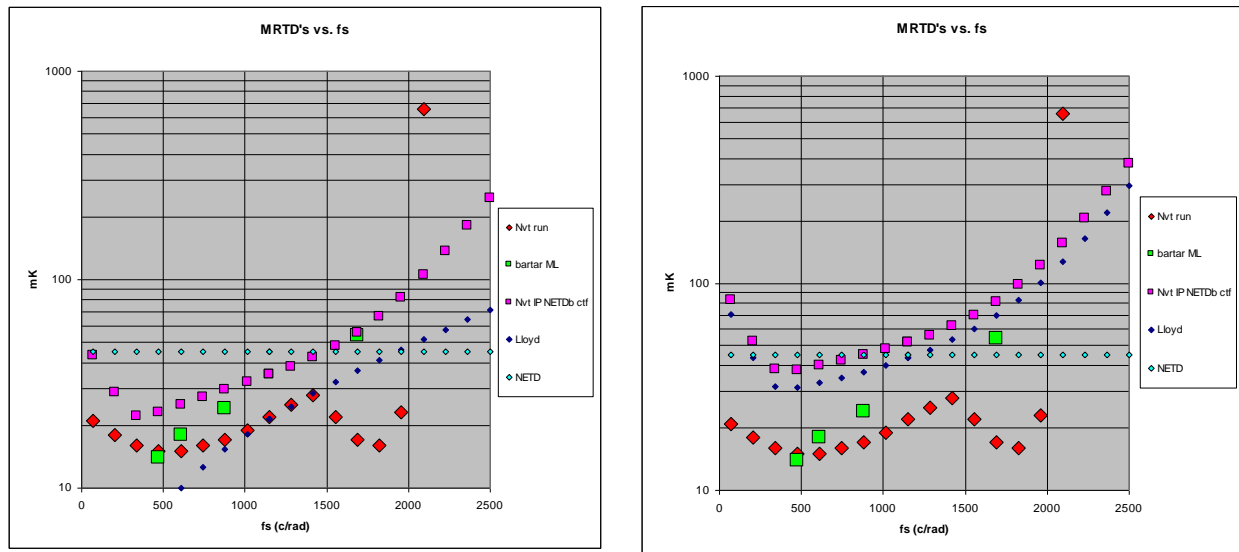


**Figure 14: MRTD's from equations (blue and purple), NVTherm IP outputs (red diamonds), matlab image viewing (green squares), left plot is without Stmp component, right is with full expression**

### 2.3.3 Detection, identification and recognition of small (subtended) objects

Recently we procured copies of NVTherm2002 and NVThermIP for comparisons with this model's system level outputs. The cooled and uncooled detector models in the NV products are not at all comprehensive; however, their image evaluation models are considered one of the standards for predictions of MRTD's and detection and ID probabilities. Many of the MTF and MRTD equations I used in my model were taken from or derived from equations in the NVTherm manuals. As such, exact agreement with NV model products for system level parameters is expected. Much of the work in this model is geared towards providing a physics-based simulation tool for the accurate approximation of NETD for the many material, optical and electronic properties that are involved in each of the manufacturers' products. The model can then be used as a tool for device geometry and device materials optimization and with the addition of the image generation and analysis functions will provide an end-to-end uncooled sensor analysis tool.

The next task was to compile as extensive a database of bolometer pixel characteristics as possible from the vendors inputs, input these into the model, run performance predictions and compare these to data if available, and extend the image evaluation section (MTF's, MRTD's, CTF's) and assure agreement with NVTherm outputs. Accomplishing these tasks, the model was able to provide validated performance predictions from basic semiconductor materials inputs all the way through to image and image sequence generation and image evaluation.

Bolometer sensor system performance parameters such as probabilities of target detection, target identification and target recognition are based on their mathematical components such as the NETD, the MRTD, and the target thermal contrast and size (extent on the FPA in cycles/radian).

The NETD is calculated from bolometer material and geometrical characteristics (pixel and leg geometries, electrical and thermal characteristics) from vendor specifications. The main parameters are the pixel heat capacity, the leg thermal conductance, the sensing material's absorptance, resistance, and TCR. Noise is also a factor and consists of a combination of Johnson noise, thermal fluctuation noise, background fluctuation noise, and 1/f noise. We also employ controlled spatial noise (3D noise) in the model to account for row and column noise,

etc. This model was based on the Night Vision 3D noise model. The final NETD will consist of the traditional temporal NETD value plus the spatial noise components.

The probabilities and ranges are calculated from the MRTD and the target thermal contrast and size (cycles on target from Johnson criteria). Also, for longer ranges, we need to add the atmospheric transmittance into the equation. The model finds the intersection of the MRTD curve and the target thermal contrast (apparent target contrast) curve on the plot of temperature (y-axis) vs. spatial frequency (x-axis). MRTD and target contrast are also plotted against range where we diminish the target contrast by the atmospheric transmittance as a function of range. The intersection of the two curves gives us a spatial frequency value that is used in the detection, identification and recognition equations to determine their probabilities. This calculation is also done in the NVTherm model and has been compared to this model's findings. Thus, knowing the target size and thermal contrast, we find solutions of the probability equations and the range equations for that ideal target on the modeled bolometric sensor.

For subpixel sized targets, the metric to use is the Noise Equivalent Irradiance (NEI) or the Noise Equivalent Power (NEP). For pixel sized targets the NETD value can be used to determine detection. For extended targets, the MRTD and target size and contrast are required. The NEI and NEP expressions use the target subtended area and irradiance, the detector response and noise, and the detector optical efficiency which is mainly determined by the fill factor and the diffraction spot size. The NETD is calculated from the bolometer and optics properties discussed previously. The probabilities based on the MRTD and the target characteristics are more involved and are open to some interpretation. NVTherm2002 has been updated and the new NVThermIP uses slightly different expressions, such as the CTF (contrast threshold function) and introduces the  $V_{50}$  expressions to replace the formerly used  $N_{50}$  expressions.

As an example that illustrates the detection, identification and recognition parameters, we consider a typical uncooled sensor. The format is 640x480 with 17 micron pixels, the optics is f/1 (10 cm aperture), and the frame rate is 30Hz. The fill factor is 75% and the measured NETD is 30mK. The FOV is 4.7 x 6.2 degrees and the IFOV is 0.17 mradian. The MRTD curve here has been generated using a derivation of the NTherm2002 manual expression:<sup>xx</sup>

$$MRTD = \frac{CTF_{eye}}{M_d H_f} \left\{ \left[ \frac{\pi^2}{4} \frac{(B_w B_L)^{1/2}}{S_L} K_{eye} \left( \frac{t_f}{t_{eye}} \right)^{1/2} NETD \theta_{det} f_s \right]^2 + \frac{4S_{imp}^2}{G^2} \right\}^{1/2}$$

The apparent target temperature is:  $T_{rss} = \tau_a(r) [(\mu_{tar} - \mu_{bk})^2 + \sigma_{tar}^2]^{1/2}$  and was assumed to be 0.1K.

In this example we do not include the atmospheric transmittance which is close to unity for the shorter ranges under clear conditions. From figure 12, the intersection of the target with an apparent target temperature of 100mK and the MRTD curve occurs at a spatial frequency of 3.5 to 4.0 cycles/mradian that correspond to a range of 5.2 to 6.0 kilometers. This spatial frequency is defined as the cutoff frequency and is the spatial frequency that specifies the 50% probability of recognition for this sensor and target. The MRTD curves shown are from derivations of Lloyd's expression and from NVTherm expressions. The sporadic points are from visual inspection of images generated in the matlab program.

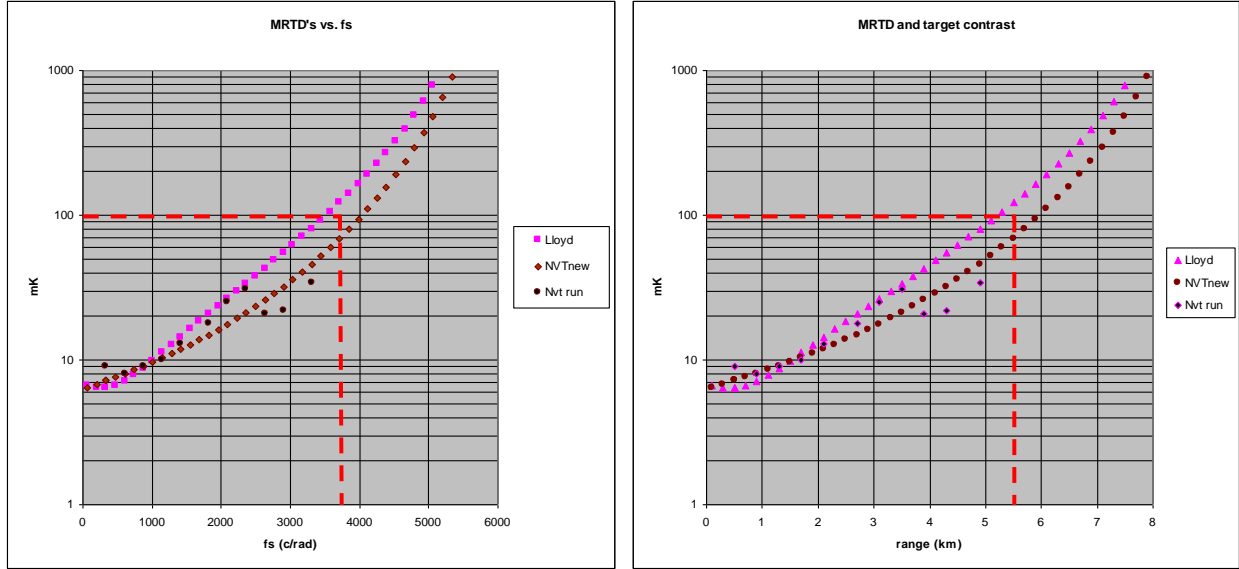


**Figure 15: MRTD curves (temperature vs. spatial frequency and vs. range) for a 4x4 meter target**

The recognition probability for other spatial frequencies can be calculated from the NVTherm2002 expression:<sup>xxi</sup>

$$P_{rec} = \frac{(N / N_{50})^{3.76}}{1 + (N / N_{50})^{3.76}}$$

Much of the probability section of this model is based on NVTherm2002 derivations which employ  $N_{50}$  values and traditional Johnson criteria using MRTD's and apparent target temperature. The newer version, NVThermIP uses  $V_{50}$  criteria, the apparent target temperature contrast, and the contrast threshold function. The probability expressions from NVThermIP are:<sup>xxii</sup>

$$P_{recIP} = \frac{(V / V_{50})^E}{1 + (V / V_{50})^E} \quad E = 1.51 + 0.24(N_s / V_{50}) \quad \text{and} \quad N_s = N_r (1 - 0.585 S_{rh})^{1/2} (1 - 0.585 S_{rv})^{1/2}$$

where  $N_r$  is the resolved spatial frequency,  $S_{rh}$  and  $S_{rv}$  are the spurious responses (horizontal and vertical)

NEI, NETD and MRTD (lab MRTD) remain the critical, most accurate and performance-telling metrics and the current model now provides accurate predictions of these parameters. Probabilities of detection, identification, and recognition and the ranges for each are much more varied due to the specific target shapes and aspects, the field environment (lighting conditions, vibration, display glare) and background clutter. We can usually assume that sensors with similar NETD's and MRTD's will provide similar target range estimations. The major variability factors then are the observer, background, atmosphere and target which are captured to some extent in the range probability equations; however, these rely also on additional empirical values derived from field observations on specific targets and target sets under specific conditions.

## 2.4 Observations/conclusions from manufacturer's data and model results

### 2.4.1 Relative strengths of noise sources

Initial looks at VOx and alpha-silicon detectors using the model and using data from DRS and L3 papers indicate that both detectors are limited by  $1/f$  noise at the high bias voltages used to maximize the response<sup>xxiii-xxxi</sup>. The a-Si is more dominated by  $1/f$  noise but it is also operated

typically at 4-5 volts where the VOx is at 2-2.5 volts. The higher resistance of a-Si allows for full frame time integration while the VOx is limited to a bias pulse and integrate to inhibit overheating the bolometer. From DRS data (17 micron pixels at 2.4 volts bias), after 1/f noise, the next highest noise source for the VOx is temperature fluctuation noise, followed by readout noise, then Johnson noise. From L3 data (20 micron pixels at 5 volts bias), the second strongest noise source is Johnson noise, then readout noise, then temperature fluctuation noise. While the absolute noise values are not given for the DRS bolometer, the ratios from the chart are 4.6, 3.7, 3.3, 2.8 for 1/f, temp fluctuation, readout, and Johnson. The model predicts similar ratios even though layer thicknesses and device structure are not known very well. For the L3 a-Si the values are 26, 12, 11, 6.5 for 1/f, Johnson, readout, and temp fluctuation. This model predicts similar ratios here also. The ratios are tabulated in Table 3.

Noise type	DRS data	RR model	Noise type	L3 data	RR model
1/f	4	4 (2e-13)	1/f	1.64	1.64 (6e-12)
johnson	1.85	2.38	Temp fluct	1.32	1.29
Read	1.69	1.69	Read	1.18	1.18
Temp fluct	1	1	johnson	1	1

**Table 3: Relative ratios of noise from data packages and this model's predictions**

#### 2.4.2 1/f noise detail

The level of 1/f noise is determined in the model by the value of the Hooge parameter or the k factor which at this point are not precisely known for the VOx and a-Si. In the literature a typical Hooge value for VOx is about  $10^{-23} \text{ cm}^3$ , but depending on processing details this value can vary greatly. We can extract a Hooge parameter value or k factor from the data if the level of 1/f noise is given. In the above table the 1/f noise was modeled using the k factor. Agreement with data was found for k's of 2e-13 for VOx, and 6e-12 for a-silicon. This indicates that the 1/f noise from the alpha-silicon is about  $\sqrt{60}$  or about 8 times higher; however this does not seriously degrade the a-Si NETD since the alpha-silicon noise bandwidth is much smaller and it is operated at about twice the bias voltage. Consequently 1/f noise based NETD limits look to be very similar. 1/f noise will also depend on the layer thickness (volume of material) so this must also be known for each type of detector to be able to predict 1/f noise.

#### 2.4.3 Response times and sensitivity comparisons

It appears from the limited data seen so far that sensitivity (NETD) is comparable for the VOx and a-Si based bolometers. It may be that the higher voltage, TCR and response available to the a-Si compensates for a higher level of 1/f noise. As far as response times, the VOx may be inherently slower due to the requirement for an absorbing layer and an underlying substrate. The alpha-silicon can be grown on a sacrificial substrate like a polymer, and doesn't require an absorber so a lower heat capacity can be achieved. For the smaller pixel sizes being developed, the model shows that the leg conductance is becoming dominated by the metallization, so thinning and lengthening of the legs may not achieve as much of an improvement in conductance as expected. None of these conclusions should be considered set in stone though, as little is known of the individual manufacturers' specific capabilities in controlling these device parameters. The Table 4 below shows model results for pixels of VOx and a-Si for identical C and G values (first 3 columns), then for reduced C and G (last two columns). The NETD predicted for a typical VOx at 2.5V is 40mK and is 1/f noise limited. The alpha-silicon with the higher 1/f k value has an NETD of over 100mK. Reducing the 1/f noise k value to that used for the VOx gives a total NETD for the a-Si bolometer at 5V (column 3) of 57mK, this time limited by the Johnson noise. A twofold reduction in size (C and G) gives total



a-Si NETD's of 55mK and 30mK. From these initial simulations it appears that as the data has shown, the performance of these two detectors will be similar and final performance will probably be determined by manufacturing subtleties and readout electronics. Spatial noise has not been mentioned and this may also become a factor in overall performance. Nonuniformity correction (calibration) must be sufficient to limit spatial NETD to a level significantly below the temporal NETD.

NETD's for 20 micron pixel, f/1, 30Hz, 12ms				.5C, .5G	.5C, .5G
noise	vox	asi	asi	asi	asi
tf	18	17	17	12	12
john	10	49	49	25	25
1/f	34	94	24	47	12
for k =	4.00E-13	6.00E-12	4.00E-13	6.00E-12	4.00E-13
total	40	107	57	55	30

**Table 4: NETD's predicted from model for like-detectors of VOx and a-Si for different levels of 1/f noise.**

## 2.5 Simulation of microbolometer sensors for aerial collision avoidance

In these examples we look at a wide angle FOV (from 20 to 40 degrees) with f/1 optics for small aerial object detection. The frame rate is 30Hz, the spectral band is 8-12 microns, the baseline NETD is 40mK, and the optical efficiency is 70%. The intended target is at altitudes from 100 feet to 10,000 feet and the sensor target path is horizontal (for sky radiance and atmospheric path transmittance calculations). Atmospheric transmittance and radiance data from many MODTRAN runs over the 8-12 micron spectral range were compiled and a model in excel was developed from these data tables<sup>xxxii</sup>. **(18)** Horizontal path sky radiances were compiled for these altitudes and were compared to blackbody curve outputs to assign an effective blackbody temperature to the path inband radiance values from MODTRAN. These **effective** temperatures vs. altitude are shown in Figure 16a which were derived from MODTRAN model runs. Note that the actual temperatures at the altitudes are higher than the effective temperature. The effective temperature takes into account the path emittance from the sensor to space which is less than unity. For example, the MLS sea level temperature is 25C or 77F or 298K, but the horizontal path radiance due to absorption in the 8-12 micron band is only 80% of the ideal spectral sum radiance of a perfect 298K blackbody radiator. The 80% emissivity 298K radiator is equivalent to a 100% emissivity 285K radiator. This 285K is the effective temperature used in the model to calculate inband path radiance. From MODTRAN runs at each altitude we get the effective temperatures that are used in the excel model to approximate horizontal path radiances. For the path transmittances, MODTRAN runs at various altitudes and path distances were used to find absorption coefficients as functions of altitude and path length. These are shown in. These expressions are used to calculate the SNR's for targets of defined areas and temperatures, altitudes and ranges.

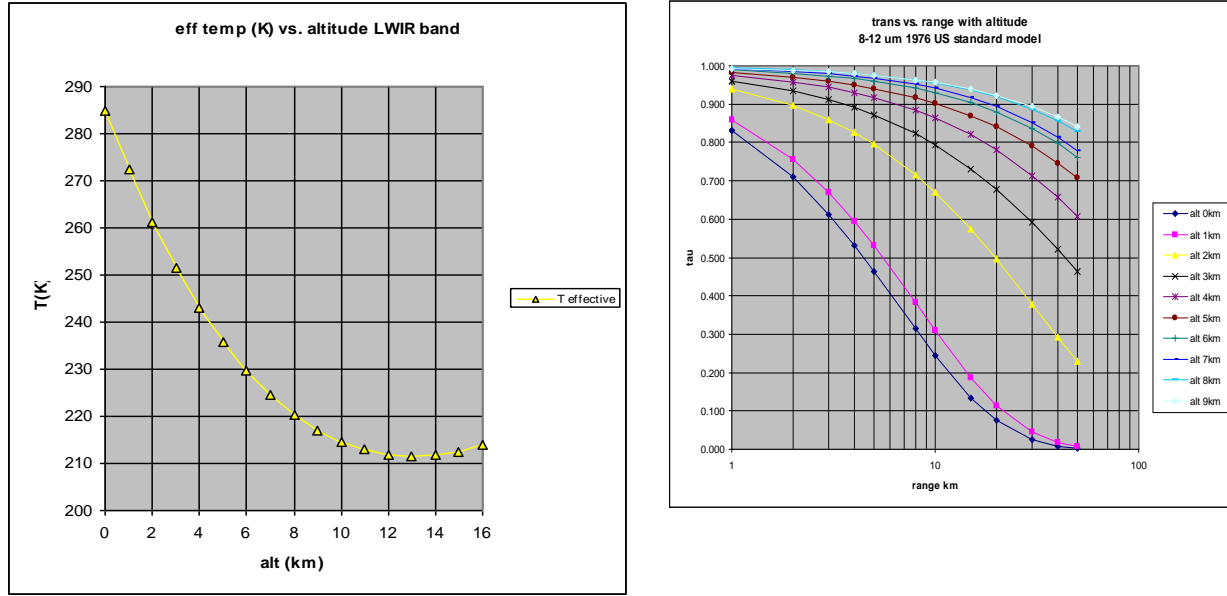


**Figure 16: Effective temperatures of horizontal path vs. altitude (left) and 8-12um transmittances vs. range for altitudes from sea level to 10km (right)**

Sensors and scenarios were investigated to predict SNR's from aircraft at various temperatures and areas, and at various ranges and altitudes. A few of the common bolometer camera FPA formats and FOV's were simulated and the plots in Figure 17 were generated from these excel model runs.

For SNR calculations for subpixel targets, we use the  $NEP$  or the  $V_{noise}/Response$  ratio. The SNR is:

$$SNR = [P_{tar} - P_{scnobs}] / NEP$$

where  $P_{tar}$  is the target energy on the sensor optics (watts) and  $P_{scnobs}$  is the contribution from the path radiance that is obscured by the target.

The response is given as:

$$\mathfrak{R}_G = \frac{\alpha_{icr} V_b}{G} \frac{R_b R_L}{(R_b + R_L)^2}$$

The cases modeled were:

**Case#1:** 40 deg FOV, 0.5" optics, 28um 320x240 FPA, f/1, target deltaT = 30F, target area = 4m<sup>2</sup>, for altitudes of 100ft. to 20kft.

**Case#2:** 20 deg FOV, 0.5" optics, 28um 160x120 FPA, f/1, target deltaT = 5F, 15F and 30F, target area = 2m<sup>2</sup>, for 100ft.

**Case#3:** 25 deg FOV, 1.0" optics, 17um 640x480 FPA, f/1, target deltaT = 130F, target area = 1m<sup>2</sup>, for 10, 20 and 30kft.

These SNR plots are as accurate as the known values for the camera NETD and the optical efficiency. Reported values for f/1 NETD's range are in the 20mK to 50mK region for most of these uncooled sensors. The general trend is a decrease in NETD with pixel size. The NETD was taken to be 40mK for all cases and the optical efficiency (which includes the optics transmittance) was 70%. If the actual NETD and optical efficiency are different, the plots will

move slightly up or down linearly with the NETD and optical efficiency ratios. That is, if the optical efficiency is 60%, the SNR plot should be lowered by 0.6/0.7.

The signal was calculated as the difference in level (voltage) of the pixel containing the target to a nearby pixel that is observing only sky radiance. The accuracy was checked by adding a 285K target in the pixel IFOV (target being the same temperature as the effective sky temperature). The signal here was seen to be zero. As an additional check, the target was made to fill the IFOV and set at 285.04K. Here the delta is equal to the NETD of the uncooled sensor. The signal to noise was exactly one when the effect of the atmospheric transmittance was removed.

The sky radiance was modeled from MODTRAN runs for horizontal paths at the specified altitudes. The inband target radiance was calculated from a blackbody emitter at the specified area and temperature, diminished by the atmospheric path transmittance. The path radiance (target to sensor path) was added back into the expression so that a target at ambient temperature produces zero signal. The signal was diminished by the optical efficiency as in this case, 30% of the target signal will be collected by the target pixel. In the bolometer model, the delta signal produces a temperature difference and resistance change in the bolometer which is sensed as a voltage difference. This voltage difference divided by the total noise voltage is the SNR. The target was moved from 1km to up to 50km in horizontal range and SNR's were tabulated for all cases.

The top left plot in Figure 17 for **case#1** shows SNR's for the 40 deg FOV 320x240 sensor and the +30F 4m<sup>2</sup> target. As expected, SNR's are shown to be higher for the lower altitudes tracking with the atmospheric transmittance. The SNR = 6 level for this target is in the 6 to 14 km range for these altitudes. The +30F target is defined as 30F above the sea level temperature (77F) or 107F and remains 107F at all altitudes. Note that at the lower two altitudes, the transmittance diminishes the signal much faster. The higher altitudes (above 3000 ft) allow for about twice the SNR6 range.

**Case#2** (upper right plot Figure 17) for the 160x120 20 degree FOV sensor shows improvement in SNR with target temperature delta. All SNR of 6 levels occur within the 3.7 to 4.7 km range for the +5F to +30F 2m<sup>2</sup> targets.

In **Case#3** for the 25 degree FOV 640x480 sensor, the SNR of 6 levels from the 1m<sup>2</sup> 130F delta target are in the 27 to 35 km range. The plot at 10kft shows more attenuation of signal than the plots at 20kft and 30kft which are nearly identical.

NETD's in current sensors will probably be close to the estimated 40mK for the small pixels, where for the larger pixels, NETD's may be as low as 30mK. Vendor data has shown the best FPA's can achieve NETD's 10mK or so better than these values; however, average NETD's over a decent sample of detector arrays are more in the 30-50mK range. From the limited data acquired from the vendors for this study, it remains unclear what the limiting noise mechanism will be for the alpha-silicon and the vanadium oxide detectors. 1/f noise may be the limiting noise source for both detectors, especially at the higher bias voltages; however, hard numbers (k-values or Hooge parameters) were not available. If the best detectors are used (lower NETD values), the case #1 and #2 ranges may be increase somewhat. Cooling the FPA to 220K may also improve NETD by up to a factor of two according to some L3 data on their alpha-silicon. We have not seen any data on vanadium oxide at lower temperatures for comparison.

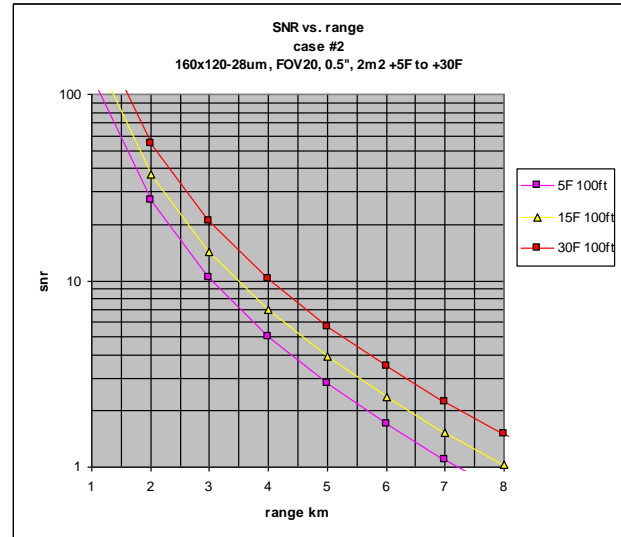
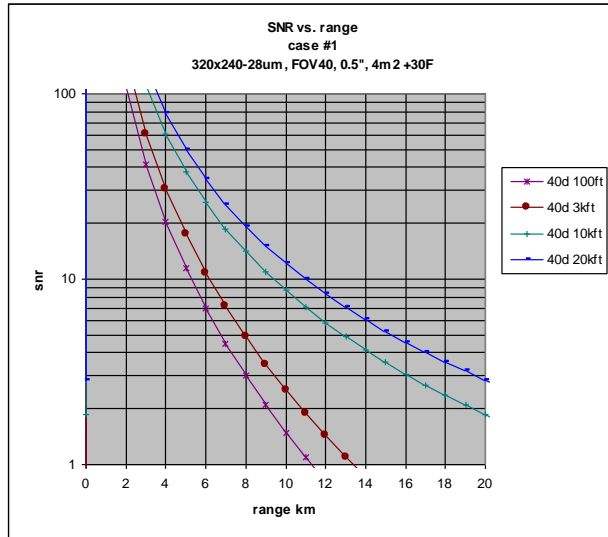


**Figure 17: SNR's vs. target range for case 1 and 2 sensor configurations**

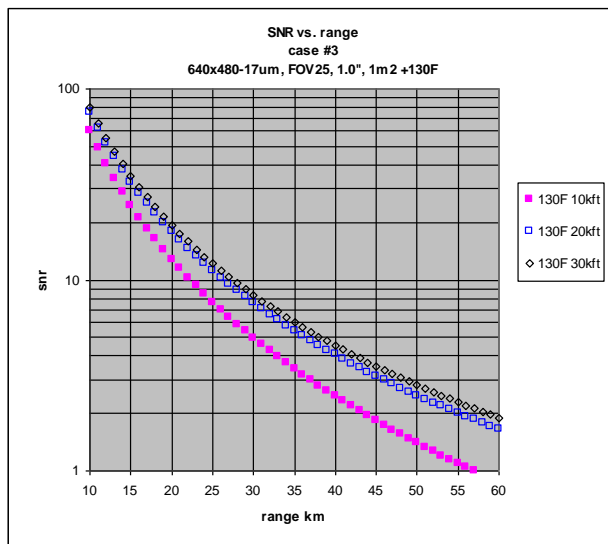


**Figure 18: SNR's vs. range for case 3**

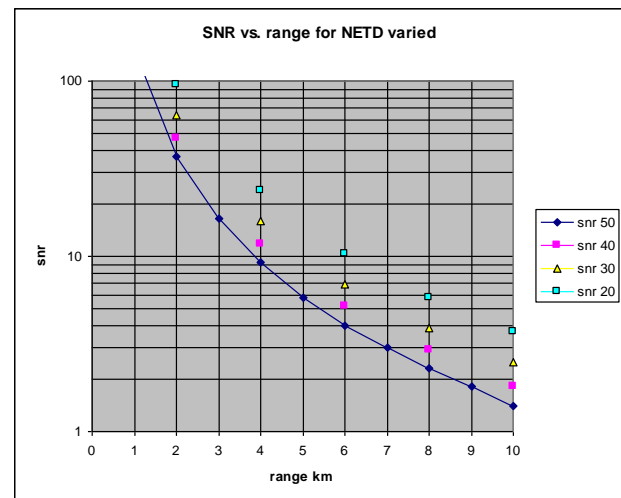


**Figure 19: SNR's vs. range with NETD varied from 20 mK to 50 mK**

In Figure 19 we reproduce the results with some differences in NETD to show its effect on SNR and range. The baseline NETD was 40mK and other typical and possible NETD's of 20, 30, and 50mK produce the plots shown in Figure 19. In general we see increases in range with reduction in NETD. For the SNR=6 criteria, the ranges for 50, 40, 30 and 20mK NETD's are 5, 5.6, 6.5 and 8 km.

Uncertainty in NETD, in optical efficiency (a function of the optical spot size and detector area), and variations in atmospheric transmittance and turbulence will all add uncertainty to these range estimations. For the lower altitudes, the transmittance will vary much more significantly with different levels of humidity and aerosol. Currently, three atmospheres have been generated for use in calculating SNR, the U.S. standard 1976 model with 23 km visibility (rural), the mid-latitude summer with 23km visibility and then with 5 km visibility (both rural). The 8-12

micron band transmittances are shown in Figure 20 for these three choices. These charts were generated from MODTRAN runs for horizontal paths. The MODTRAN data were fit with  $\exp(-a \cdot \text{range}^b)$  expressions which give very accurate fits to the data from 1 to 50 km path lengths.

The effect on SNR from atmosphere variability is shown in Figure 21 for the case #2. A +30F target gives SNR's vs. range as follows for altitudes of 0 to 3 km for three specific atmosphere prescriptions. The US 1976 Standard atmosphere with 23 km visibility (aerosols) gives the highest SNR's. The second best is the midlatitude summer model with 23 km visibility and the third best is the midlatitude summer with 5 km visibility. For the sea level altitudes, the SNR=6 range for the three atmospheres are from about 4 km to 5.5 km. Going to a 1 km altitude improves the range to 5 to 7 km. The SNR=6 range for the US Standard atmosphere is about 9 km for the 3 km horizontal path.

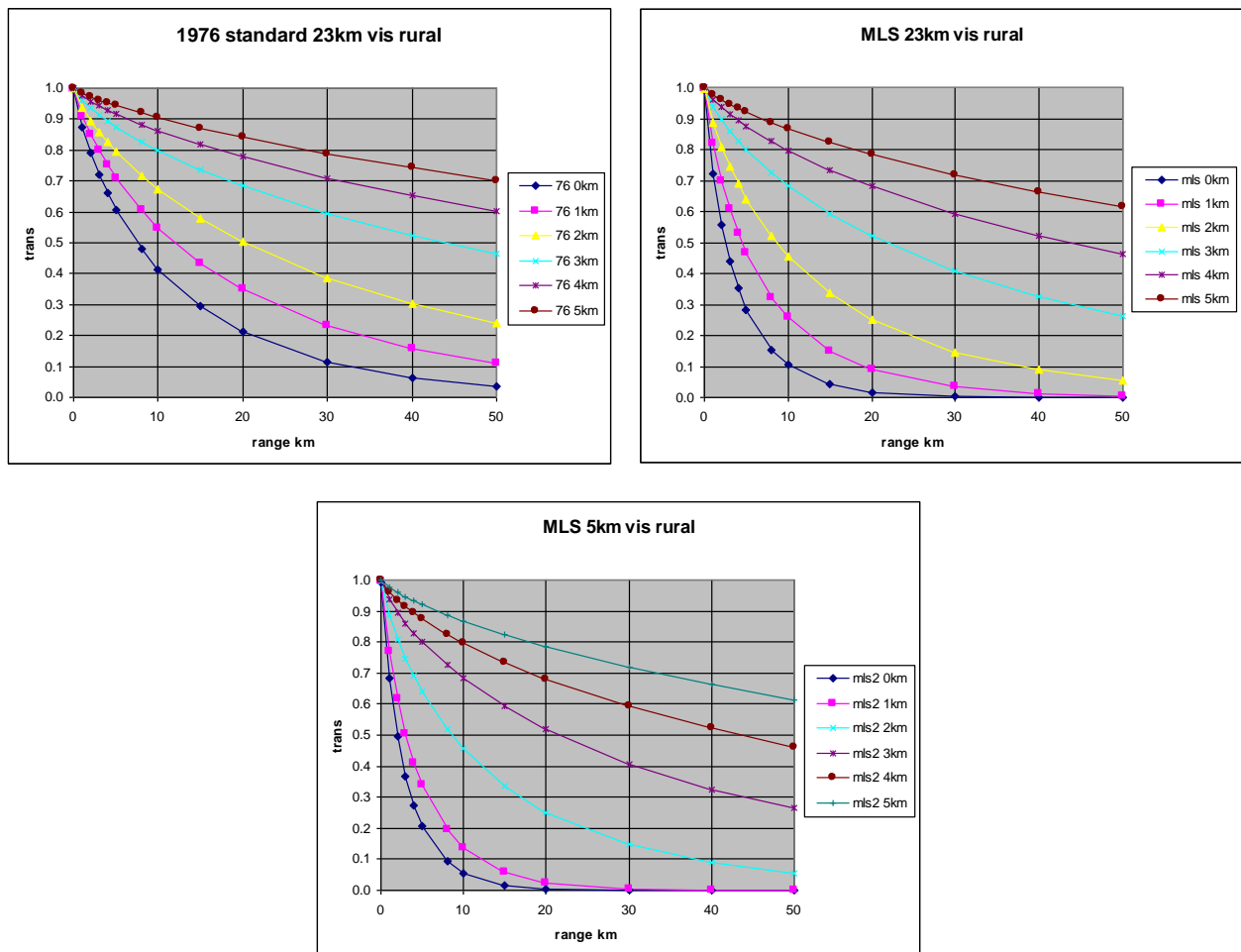
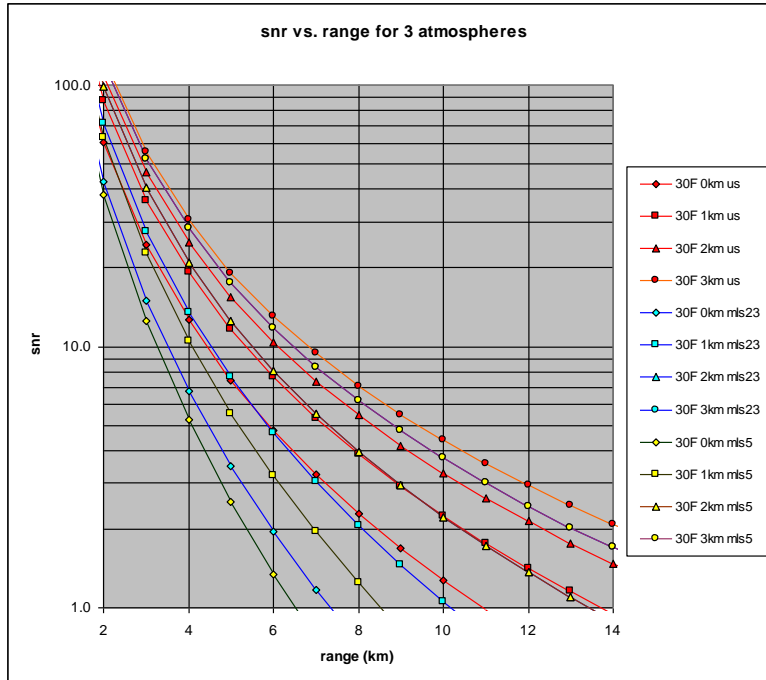


Figure 20: Three atmospheres currently simulated in program



**Figure 21: Case #2 with a +30F target and at altitudes from 0 to 3 km for the 1976 US standard 23km vis, the MLS 23km vis and the MLS 5km vis atmospheres.**

## 2.6 Some unique attributes of the model

The model consists of some unique characteristics that were developed to better characterize microbolometers and uncooled cameras. Some of these attributes are:

1. Detailed equations for NETD and NEP from first principles: bolometer geometries and layer characteristics.
2. Radiometric expression derived for background solid angle gives more accurate calculation of NETD for low f-numbers.
3. NETD expressions allow for centrally obscured optics (reflective), as do the diffraction spot size calculation (EOD for diffraction limited optics which is used in the NEP and NEI calculations).
4. Response is calculated for all contributions from the heat balance equation, not just the usual approximation using the leg thermal conductance.
5. Creation of simulated bar target imaging sequences that when observed by the human eye give MRTD's that are in agreement with NVTherm MRTD(f) results.
6. Full use and validation of model to NVTherm equations and outputs for MTF, MRTD and probabilities of detection, identification and recognition.
7. Model provides a seamless transition from subpixel region (point object images and performance predictions, NEP and SNR) to resolved region (extended object images and performance predictions, NETD and MRTD).

The differences in NETD due to the scene solid angle expression used are shown in figure 19. Expressions found in the literature were either of the form  $4F^2$  or  $4F^2+1$ . The first overestimates the solid angle, the second underestimates it. All expressions converged for the larger

f/numbers, but significantly differ from f/1.5 on down. The expression used in the model (middle curve) gives an accurate value for the area of a sphere subtended by a solid angle phi for all f-numbers.

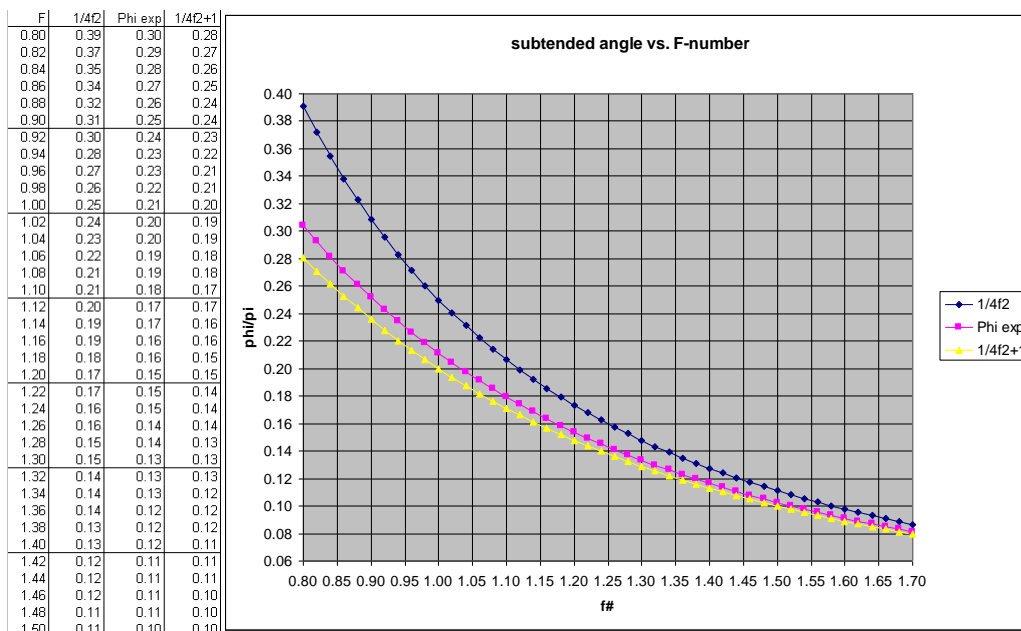


Figure 22: solid angle of scene (phi/pi) gives more accurate NETD at f/1 and lower

## 2.7 Summary and discussion

A microbolometer model has been developed and validated that predicts accurate NETD values for specified bolometer materials, geometries and electronics. The model was implemented in excel and in matlab to provide detailed single pixel predictions and realistic image sequences complete with nonuniformities and 3-D noise. The model was extended to predict MRTD's and probabilities in accordance with and validated to the Night Vision models (NVTherm2002 and NVThermIP). Both NETD's predicted by the model and MRTD plots generated by the model are in close agreement with other model results from literature and to NVTherm outputs and simulated visual bar target observations. The model was applied to the mission of collision avoidance to predict SNR's and ranges for a variety of scenarios. Further efforts in validation and model development (in order to fully predict and characterize performance) rely on discerning the practical limits in bolometer pixel manufacturing and the bolometer materials semiconductor characteristics such as 1/f noise, TCR, resistance and absorbance. Knowledge of the vendors' electronics readout and noise reduction schemes and effectiveness will also be required to determine if electronics noise and spatial noise can be kept below the total of the other four types of temporal noise (1/f, Johnson, thermal fluctuation, and background fluctuation) for future designs. The model as it is predicts the major noise components in correct proportion for both the alpha-silicon and vanadium oxide microbolometers

Some observations here that look to be typical of f/1 uncooled microbolometer sensors are that both types of detectors (VOx and a-Si) are limited by 1/f noise at the higher bias voltages; otherwise, higher biases would continue to improve performance. In general, the a-Si bolometers exhibit slightly faster responses, but also may have higher inherent 1/f noise. MRTD predictions from my matlab images, NVTherm runs, and from the various equations show that for a large part of the spatial frequency range, the MRTD remains less than the NETD, up to a factor of two to three times less. This is a direct result of the eye integration which sums a few frames (signal) while rejecting some of the temporal noise which provides a square root of the

number of frames integrated improvement in SNR and MRTD. The eye CTF(f) and the system MTF(f) functions are the other variables used in the MRTD equation. Eye CTF is dependent on ambient illumination and display characteristics and the system MTF in the model is comprised of diffraction effects, detector sampling effects, and spurious response or aliasing.

### 3 Hardware and Software

To accomplish the goals of the program COTS technology was extensively leveraged. Off the shelf microbolometer cameras and existing data collection software was modified to meet the needs of the program.

#### 3.1 Data Collection Software

Streams5 ([www.ioindustries.com](http://www.ioindustries.com)) a Windows based multistream data collection software. It allows the simultaneous collection of data streams in multiple formats to multiple devices (Figure 23). This video transmission formats used in this program was analog, LVDS, CameraLink and GiGE. It is deeply integrated with Windows via C++ and has open source PYTHON scripting capability [www.python.org](http://www.python.org). IO Industries was hired to code special drivers for the GiGE interface and IMU integration. The data was exported in a RAW format for use with MatLab (UConn) and MatCad and ImageJ (MilSys). [ImageJ](http://imagej.nih.gov) is a Java based open source image processing program supported by the NIH.

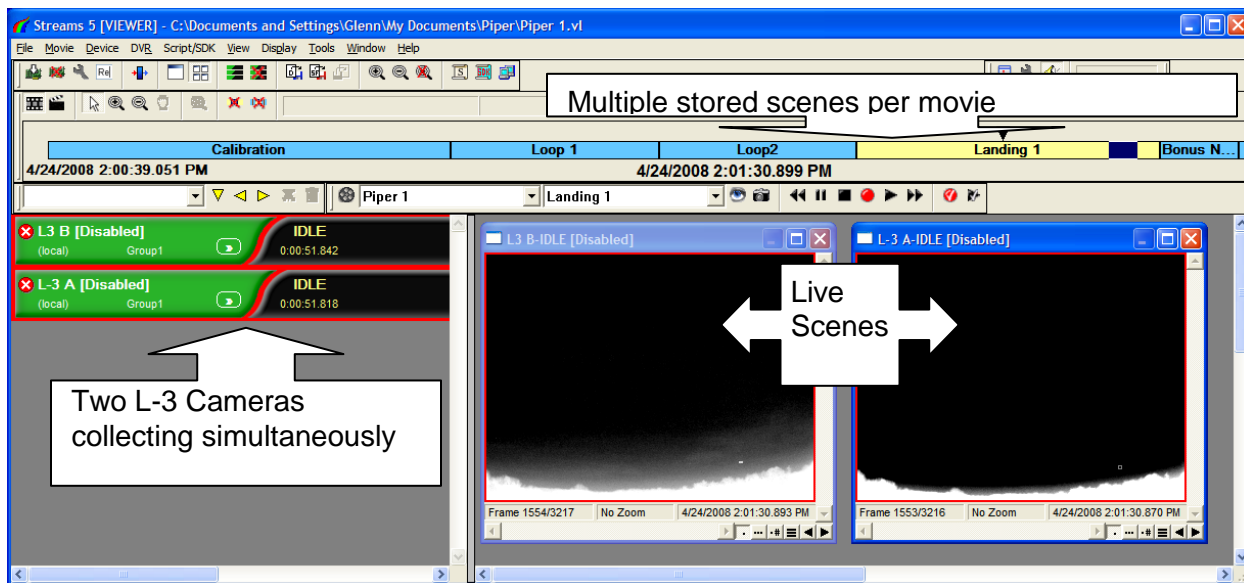


Figure 23: Streams5 screen capture

Several custom models were created to support hardware setup and GigE driver integration (Figure 24). The L-3 hardware setup was via a USB port. The GigE was controlled through an iPort driver developed by [Pleora](http://pleora.com). The IMU (inertial measurement unit) was programmed via the iPort through a UART to the FPGA (See 3.4).



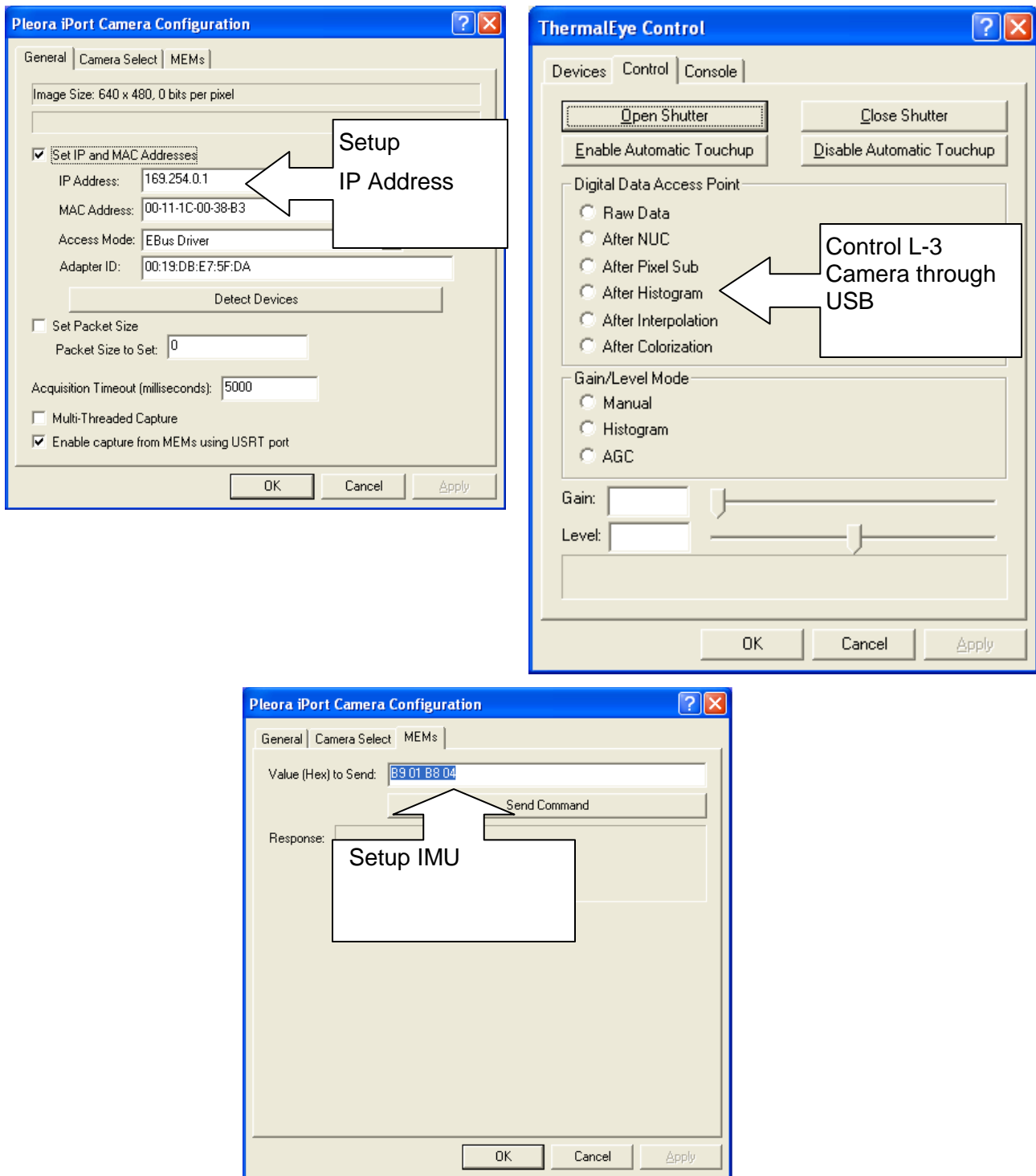


Figure 24: Modules to developed to control the camera and IMU.

### 3.2 COTS Microbolometers

The two core technologies, Vox and a-Si, (Table 5) for microbolometers were extensively studied and reviewed for the program. The BAE camera uses the SCC500 core with a third party CameraLink interface and lens from OPHIR. The L-3 4550AS came complete with lens, analog output, and a 16bit digital OEM port. MilSys designed for it an interface board for the

OEM port for both the LVDS and GigE output (See 3.4). Unsuccessful attempts were made to purchase a DRS 640 X 480 Vox microbolometer. Indigo (FLIR) also sells a similar package, but was not contacted due to the potential non-disclosure issues. Raytheon has a very small package (Figure 25), however due to their commitment to meet DoD sales, at the time no cores were available for testing.

		
Manufacturer	BAE	L-3
Optics	$\phi 1''$	$\phi 0.5''$
Pixels	640 X 480	320 X 240
FOV	28°	54°
Pixel Size	25 $\mu\text{m}$	30 $\mu\text{m}$
Technology	VOx	$\alpha$ -Silicon
Range	8-12 $\mu\text{m}$	7-14 $\mu\text{m}$
Sensitivity	<50mK	<50mK

**Table 5: Comparison of the specifications of the two(2) main MB technologies.**

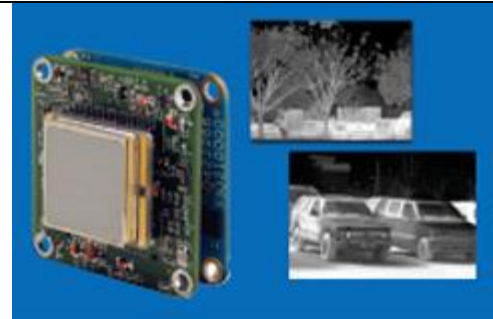


**Figure 25: Raytheon microbolometer 320 X 240, 25um with electronics**

As part of the development process the noise and S/N ratio of the cameras (both VOX and  $\alpha$ -Silicon) was measured. Several macros were written in ImageJ to process the videos.

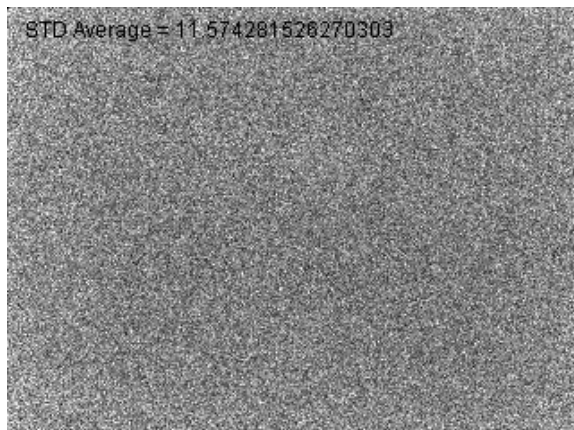
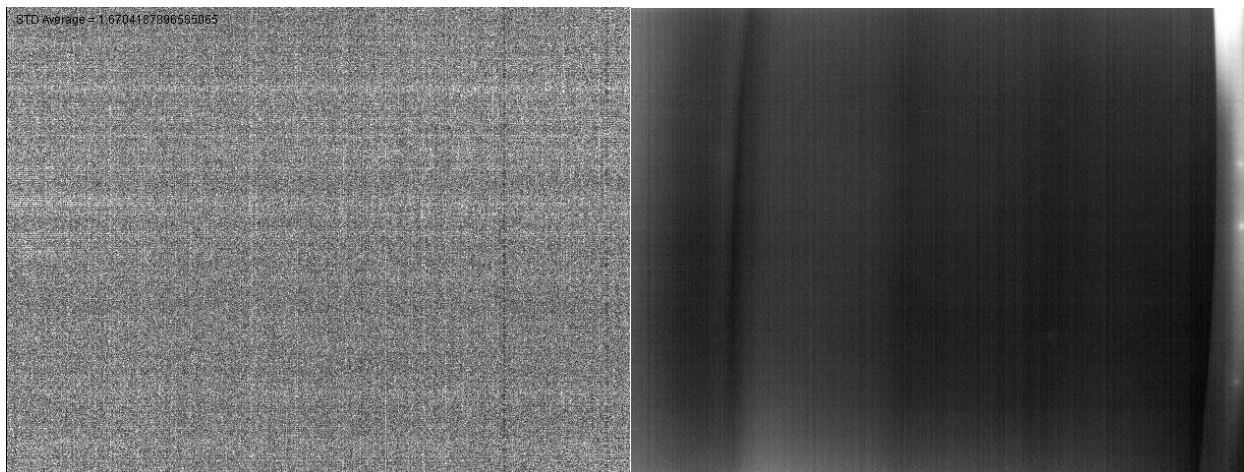


**Figure 26: STD and average of the L-3 microbolometer. Note the red circle is a defect in the FPA.**

The images above (Figure 26) are from the  $\alpha$ -Silicon viewing a wall. The above left image is a standard deviation (n=100) of the still image (AVG n=100) on the right. The STDEV is uniform over the entire image. The population average of the STDEV is approx 11.5 counts out of 16bits. Note the red circle; it is a problem with the camera developed during the first two months. Interestingly it does not affect the measurements. It was returned to the factory for repair.



The images above are from the BAE Vox viewing the same wall as the  $\alpha$ -Silicon. The above left image is a standard deviation (n=100) of the still image (AVG n=100) on the right. The STDEV indicates some fixed pattern noise within the image. The population average of the STDEV is approx 1.5 out of 14bits. The results indicate that both cameras have a S/N 12bits (4096:1).

The cameras were used in three configurations: BAE and L-3 parallel looking at the same scene (Figure 27), L-3 and L-3 side by side for tracking across the FOV (Figure 28), and L-3 and L-3 both parallel (not shown).



Figure 27: Camera system used to collect initial data of Ultralight. Both BAE and L3 are shown.



Figure 28: Dual L-3 Camera used in later side by side data collections.

### 3.3 GPS Data Logger

To track the position of the aircraft relative to other aircraft or the ground, portable GPS data loggers were purchased from [Landairsea](#) (Figure 29). This model was chosen for its accuracy, 2.5meters and its small size. The update rate is only 1Hz, which corresponds to 88ft/s @60mph. The factory was contacted about increasing the rate, however, it is not possible with this type of technology at the price point. In general, this resolution was deemed accurate enough for the tasks required. At the start of each data collection, the logger was located at the camera mount and then placed in the pilots pocket or on board the aircraft. The results were later exported into their customer software, a text file or Google Earth for post processing.





Figure 29: LandAirSea GPS data logger.

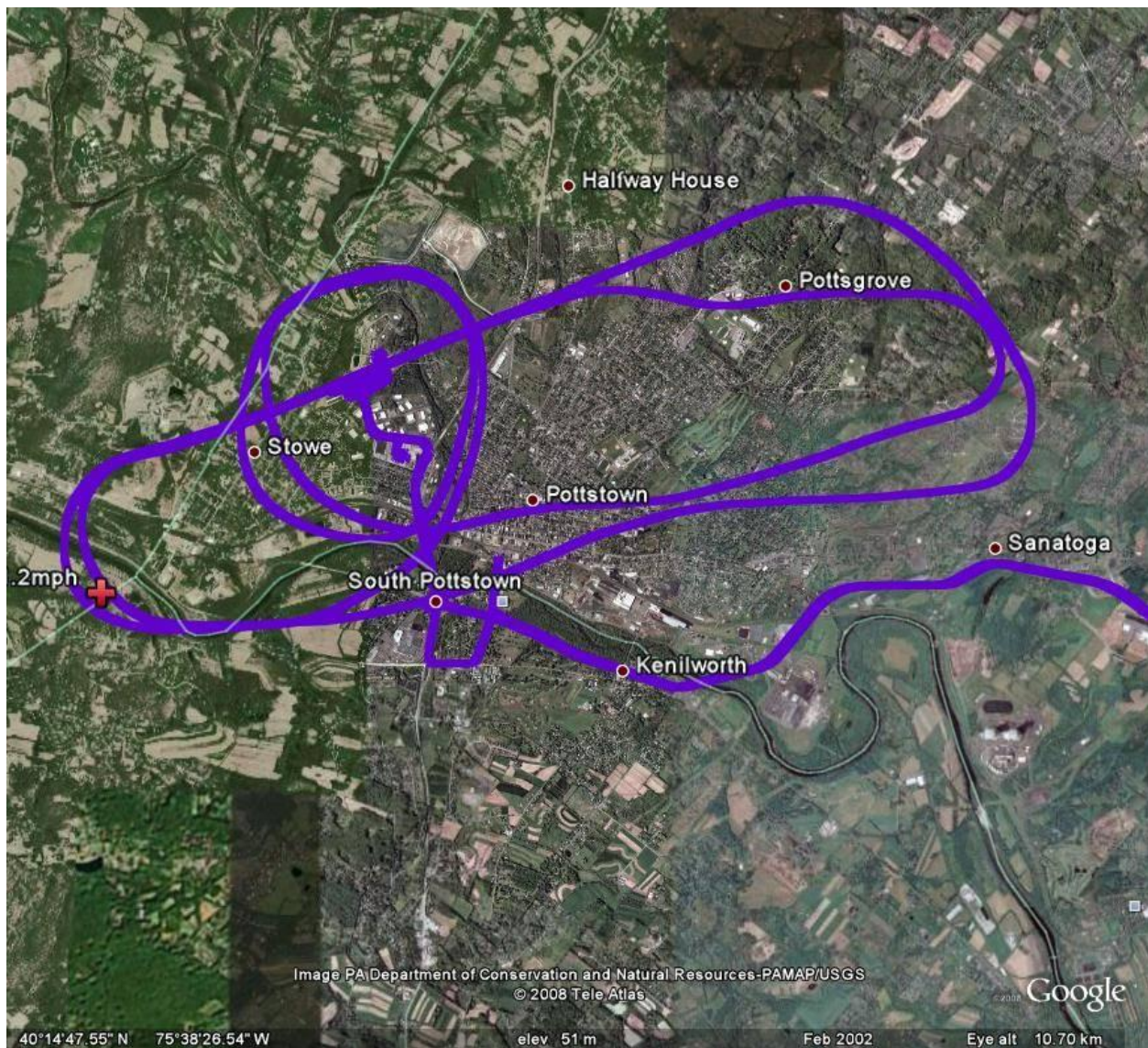


Figure 30: An example of the data export from the GPS tracker into Google Earth.

### 3.4 Aircraft

Two types of light aircraft were used for data collection Piper (Figure 31 & Figure 32) and Kolb Ultralight (Figure 34). The original work by Priest et al used a Cessna as its standard target; however, a Piper is a close match (Table 6) and was a more available aircraft. Most of the data collections, ground-air and air-air used the Kolb Ultralight. The pilot was very cooperative and he flew out of the uncontrolled airport at Alloway NJ (See 3.6).



Figure 31: Piper aircraft used for data collections.



Figure 32: Piper from website.

Figure 33: Cessna from website.

	Piper	Cessna
Maximum Take-off Weight	2,750 lbs/1,247 kg	2450 lbs/1111kg
Useful Load	960 lbs/437 kg	758 lbs/343kg
Length	24.7 ft/7.5 m	27'2"/8.3m
Height	7.9 ft/2.4 m	8'11"/2.7m
Wing Area	170 ft <sup>2</sup> /15.79 m <sup>2</sup>	174 ft <sup>2</sup> /16.2 m <sup>2</sup>
Wing Span	35.4 ft/10.8 m	36'1"/11m
MAXIMUM SPEED	145 kts/269 km/h	123 kts/228 kph
CRUISING SPEEDS	137 kts/254 km/h 75% @8kft	122 kts/227 kph 80% @8kft
<b>Table 6: Specifications for Piper and Cessna.</b>		





Figure 34: Kolb FireStar Ultralight 33ft wing span cruising speed 60mph.

The Ultralight is constructed of tubular aluminum and fabric wings. The engine is a multistroke “lawnmower” type with a large muffler. The engine is pointed towards the rear of the aircraft. The pilot indicated that the muffler during operation approaches 1200F (Figure 35). At range, the wings provide some thermal contrast with the background sky, however the primary background contrast or hot spot is provided by the muffler.

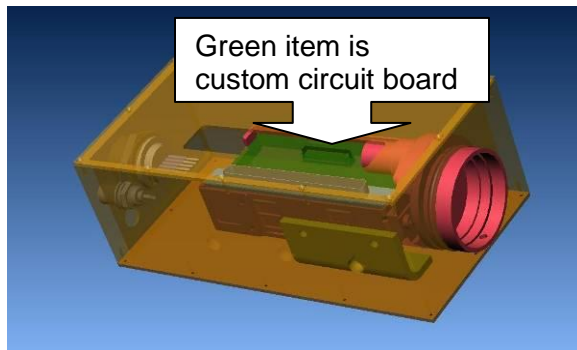


Figure 35: LWIR image of the Ultralight. Muffler runs at approximately 1200°F.

### 3.5 Camera hardware development

The BAE camera was purchased from a third party integrator which provided a CameraLink interface providing a full digital data collection. However, the L3 camera core was only available with analog output or OEM 16bit digital port. Custom hardware is required to use the OEM port. In the first phase, a OEM to LVDS interface was designed (Figure 36-Figure 38). The LVDS interface uses a 0.5” diameter stiff cable. This cable was determined to be not compatible with

the goal of developing a small data logging system that could be flown in multiple platforms, ranging from a small UAV to a larger manned aircraft.



**Figure 36: 3D model of LVDS circuit board with L-3 AS4500.**

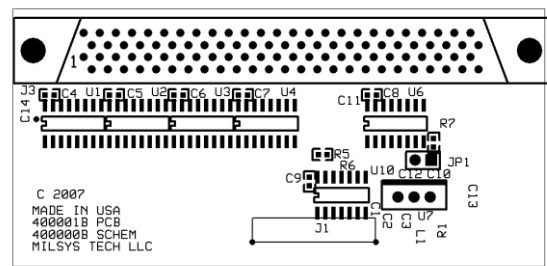


**Figure 37: Silk screen of circuit board.**

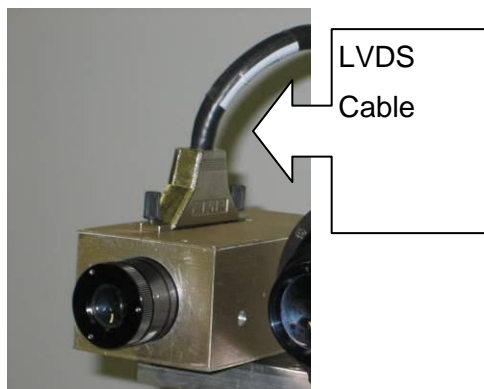


**Figure 38: Assembled camera and cable.**

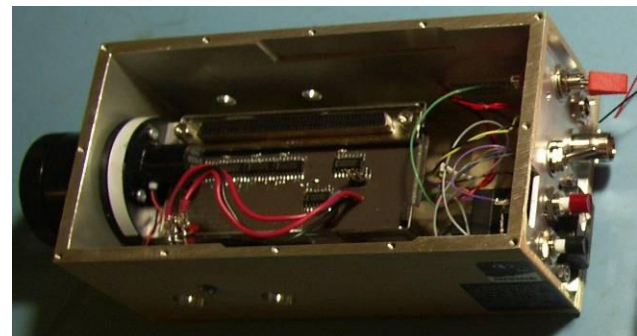


**Figure 39: L3 Core with LVDS circuit board.**

The second stage of development was to integrate IMU with a GigE interface. The GigE interface was chosen because of its high bandwidth and small cable size (Figure 40-Figure 42). The IMU was an integrated module produced by Analog Devices AD16355. It is based on their iMEMs process. Two cameras were completed for use in air-air testing.

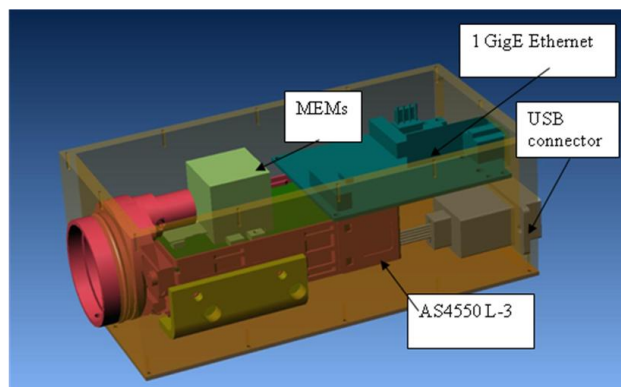


**Figure 40: 3D model of GiGE and IMU with L-3 AS4500.**

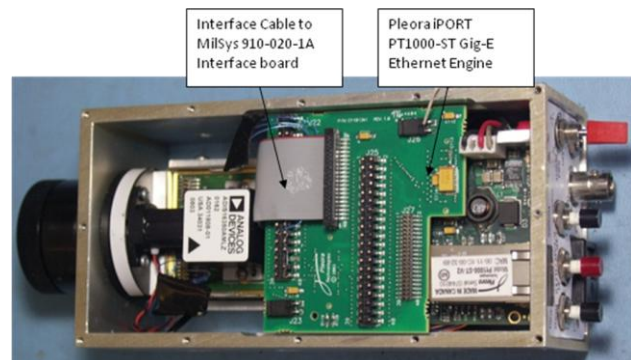


**Figure 41: View of the completed camera.**

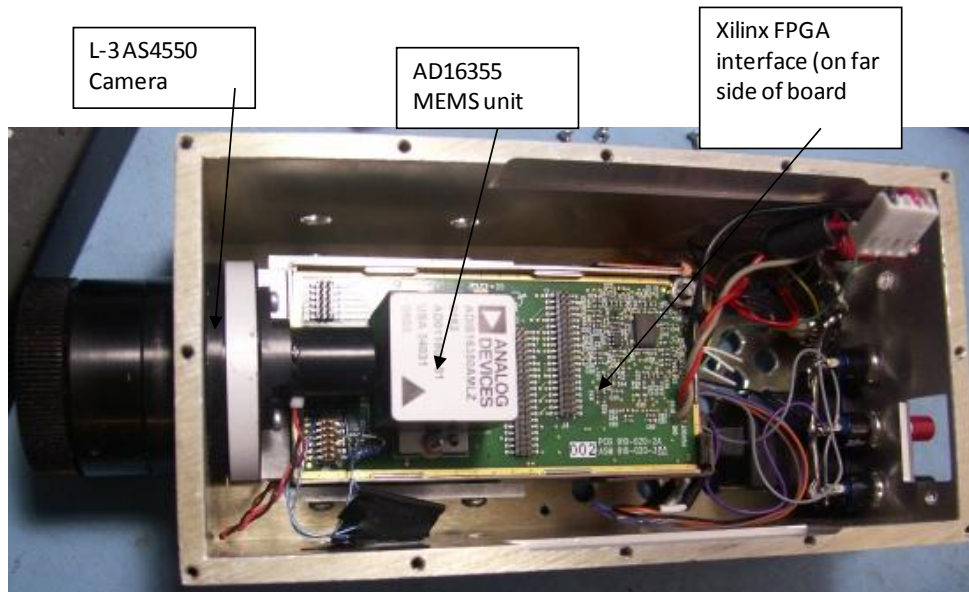


Figure 42: View of the completed camera.

To collect air-air data an ITX form factor PC (Figure 44) was chosen due to its size, power requirements, and dual GiGE ports. A small ruggedized 80GB disk drive was installed. A portable Lead Acetate battery and charger were installed in the Kolb Ultralight behind the pilots seat (Figure 43). The camera was installed on a removable mount on the nose (Figure 45). The mount was isolated from aircraft with vibration mounts. The engine is also isolated from the airframe with vibration mounts. The pilot indicates that the aircraft does not vibrate due to the engine.

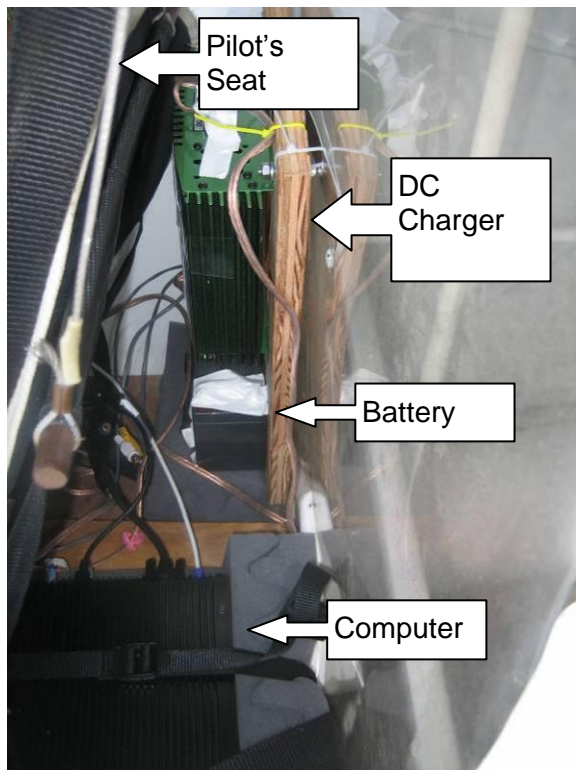




Figure 43: Installation of the computer, battery, and DC charger.



Figure 44: Mini-ITX computer.



Figure 45: View of the completed camera installed in the UltraLight.

### 3.6 Airports

All of the data collections took place at two airports, Pottstown, PA (Figure 46-Figure 48) and Alloway (Figure 49 & Figure 50), NJ, during 2007-2008. Pottstown is a public ATC local municipal airport. Alloway is a private uncontrolled airport. Due to the flexibility and lack of restrictions, Alloway airport was the primary chose for data collections.

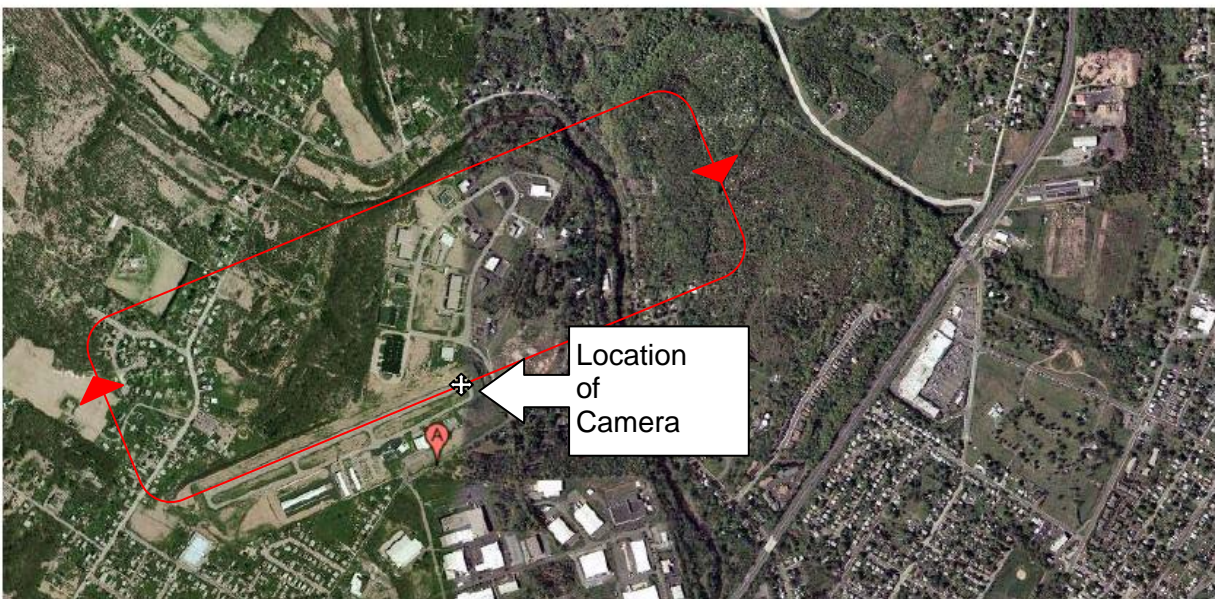


Figure 46: Ariel View with flight path of the Pottstown Airport, PA.



Figure 47: Dual camera setup at Pottstown Airport.



Figure 48: Ariel View of the Pottstown Airport, PA.

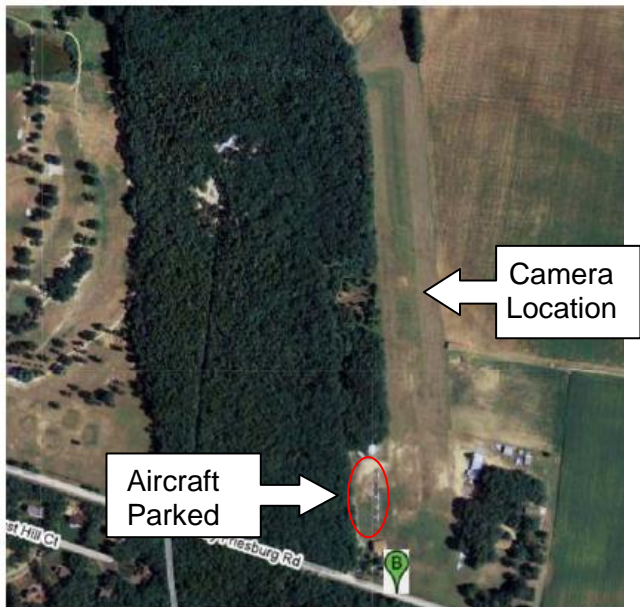


Figure 49: Ariel View of the Alloway Airport, NJ.



Figure 50: Ground level view of the Alloway Airport.

## 4 Representative Data Collections

The following is a representative sampling of the ground-air data collections and their range estimates (Figure 51-Figure 54 & Table 7).



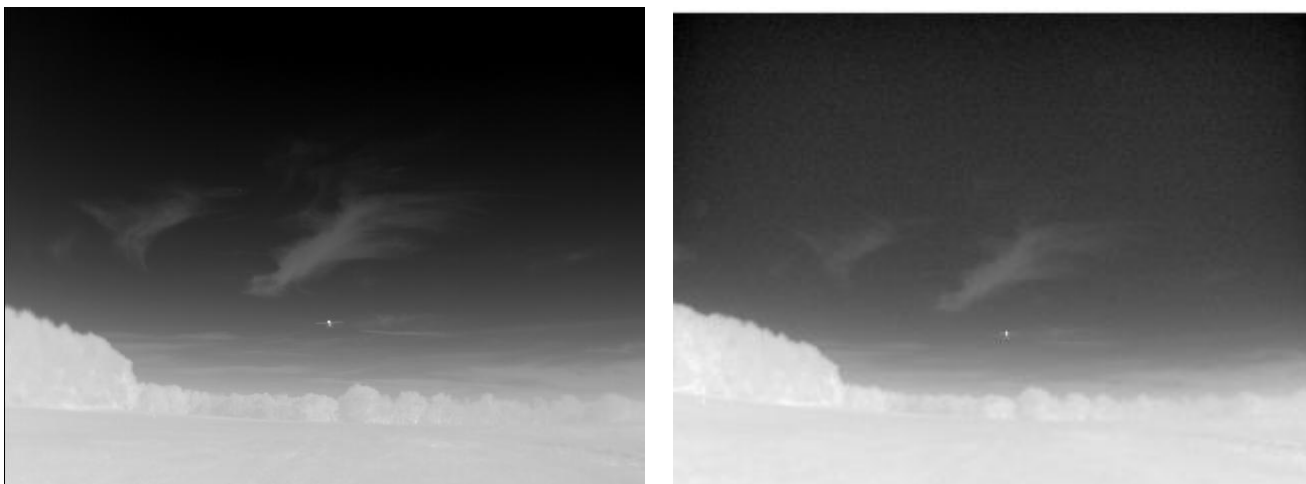
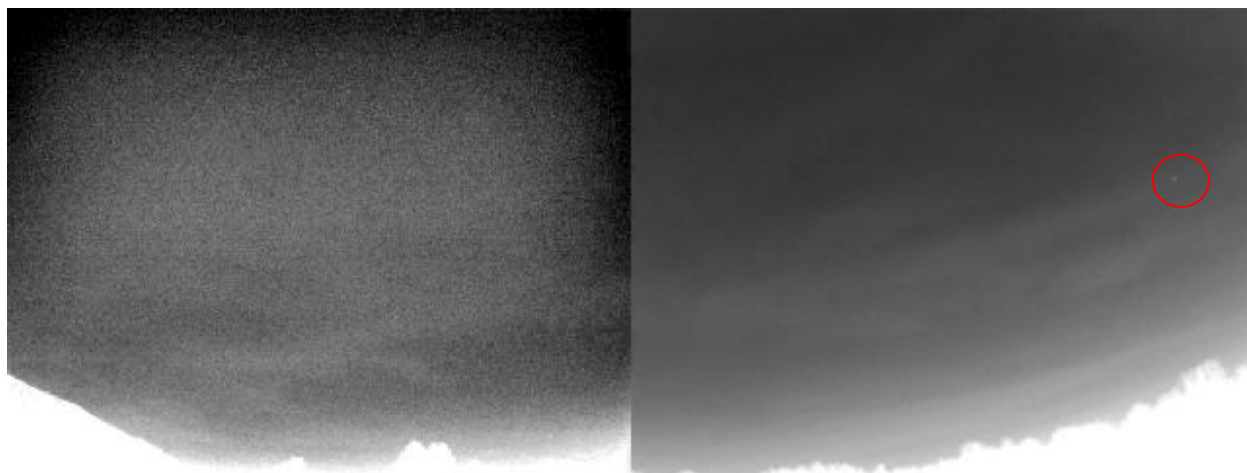


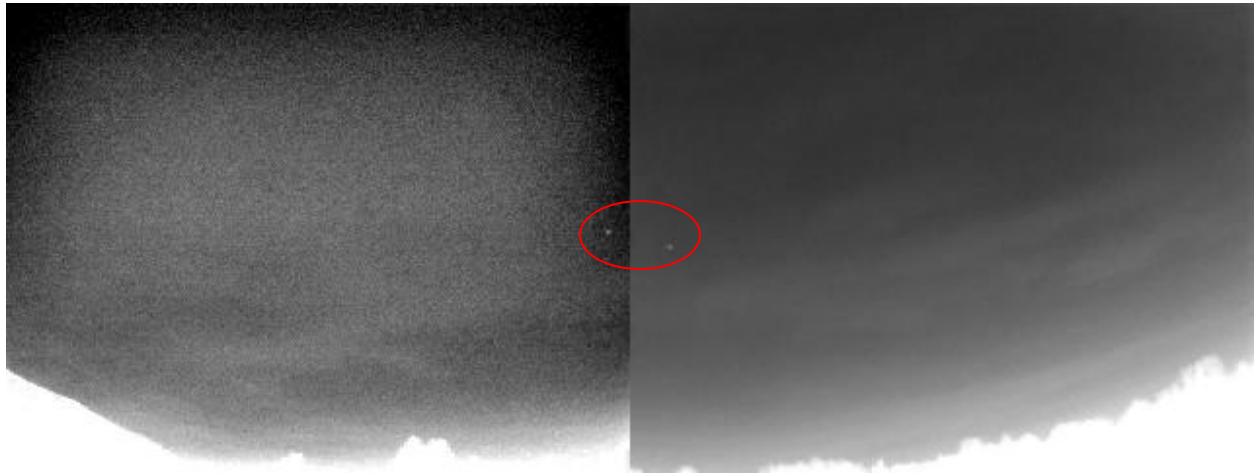
Figure 51: BAE (left) and L-3 (right) collected at the Alloway Airport using camera configuration in Figure 27.



Figure 52: L-3 both parallel (Figure 28) collected at Pottstown Airport.



**Figure 53: L-3 side by side (Figure 28) collected at Pottstown Airport.**



**Figure 54: Frame showing Piper crossing from one camera FOV to another later in the data collection of Figure 53.**

On Oct 31 both the BAE and L-3 cameras were operational and using the Streams5 software the video was collected synchronously. The pilot was instructed to pass as close as comfortable above the camera tripod and fly straight for 3 miles climbing to 1000ft. The pilot had a GPS data logger in his pocket. Actually the pilot trended to the right and flew out of the FOV of the cameras on two of the three passes. Based on the Oct 30 video, on Nov 28 the pilot was instructed to fly to 3000ft with the thought being that the background would be clearer and lower in temperature thereby improving the range performance of the camera. The pilot flew straight however, he reached the 3000ft at 3 miles. Review of the data indicated that he was at approximately the same altitude at the limits of visibility of the camera.

Start – First moment that the aircraft is visible in the scene

End – Last moment that I can see the aircraft. Aircraft is at one pixel and the Scene is zoomed on the monitor

Comments – The distance was determined by aligning the Start/End Times with the GPS data.

Note:

- 1) When in black and white, Streams5 displays 256 levels of gray the window and level need to be adjusted to try to enhance the visibility of the single pixel.
- 2) The BAE camera has 4X large lens.

	Camera	Start	End	Comments
Scene 2	BAE	9:52:52	9:54:40	Dist -1.9m(3km)
	L-3	9:52:52	9:54:40	Dist -1.9m(3km)
	BAE	9:52:52	9:55:14	Dist – 2.6m(4.1km)
	Note: I prematurely cut off some of this scene data during editing			

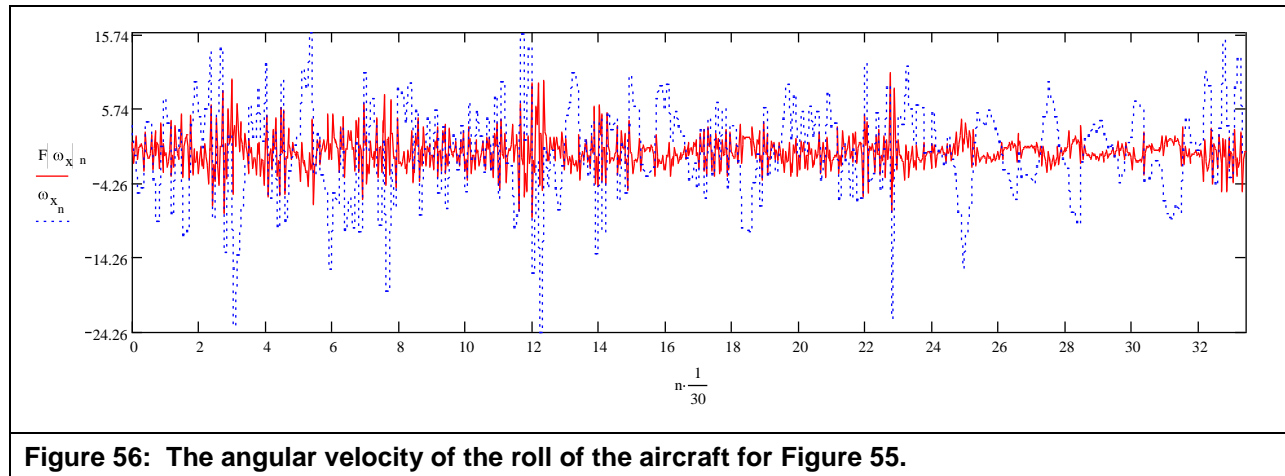
	GPS Data	Scene2.txt		AVG Speed 63.6mph Flew out of FOV Altitude – 879ft
Scene 3	BAE	10:13:55	10:14:41	Dist – 0.9km(1.5km)
	L-3	10:13:55	10:14:45	Dist – 0.9km(1.5km)
	GPS Data	Scene3.txt		AVG Speed 60.7mph Flew out of FOV 354ft
Scene 4	BAE	10:24:31	10:27:36	Dist – 3.1m(5km)
	L-3	10:24:29	10:26:31	Dist – 2.0m(3.2km)
	GPS Data	Scene 4.txt		AVG Speed 60mph Altitude 958ft The short ranging distance for the L-3 mimics scene 2.
<b>Table 7: Slant Range estimates of ground-air data.</b>				

Figure 55 is the initial test flight of the hardware developed above (Figure 42-Figure 45). A second Kolb Ultralight was used as the test aircraft. The hardware and software performed as expected and both video and IMU data was collected. The second pilot was not expected at the initial test flight and the GPS dataloggers (Figure 29) were not brought to Alloway Airport. On the inauguration flight, the second test pilot let his GPS on the wing of the aircraft and it damage the flap and the propeller. Before the aircraft could be repaired or another pilot and aircraft arranged time ran out of this program.



Figure 55: Initial test flight of the IMU for Air-Air data collection.

The IMU collects data along six axis, three acceleration and three angular velocity. Figure 55 plots the absolute roll angular velocity. The blue line represents both the absolute translation of the aircraft in degrees. The red line represents the translation of aircraft due to fast vibrations as one might expect due to the motor (2-5Hz). The goal of adding the IMU to the camera was required to stabilize the image due to vibrations not physical translations of the aircraft. The track processor would use the INS from the aircraft to correct for translations.



## 5 Algorithm Development

Dr. Bar-Shalom and Dr. Willet are world renowned researchers in the area of small target detectors and target trackers, along with Richard Osborn (grad student), they were hired to develop both a small target detector and a tracker for the PCAS program. Based upon their experience, the attitude was that the technology tasks have been solved, and that what was needed was a unique implementation (i.e. nothing needs to be invented). (Due to the software used to create their report, it is included here as a static reference. The data provided by MilSys for their development work was ground-air only.) As discussed below, technical difficulties arose and time ran out on the present contract before air-air data with inertial measurements could be provided. Their small target detector is based upon single frame processing with a measurement window ranging from 50 X 50 to 20 X 20 pixels.

### 5.1 UConn Report

# Passive Collision Avoidance System, Final Report

R. W. Osborne, III, Y. Bar-Shalom, P. Willett

September 2, 2008

## 1 Introduction

Commercial airliners are currently equipped with systems which will warn when other aircraft are within an unsafe range in order to mitigate the chances of a midair collision. Currently, the unmanned aerial vehicles (UAV), used for military operations, do not have a system which will warn of impending collisions with other airborne targets. Such a system should be able to track uncooperative targets, and therefore must not rely on communications between aircraft. In this case, the sensors used for tracking will be imaging sensors mounted on the airframe in order to observe and track targets in the surrounding airspace.

The main difficulty that arises from using imaging sensors is the fact that the resulting data will be only a two-dimensional representation of the space around the aircraft, and as such, will lack any range data for the targets which must be tracked. Without range data, the only way to detect an impending collision is to estimate the line-of-sight (LOS) velocity of the tracked targets and look for any target with a nearly zero LOS velocity.

Section 2 outlines the method of extracting measurements from the image data provided by the camera(s). Section 3 outlines the motion model and tracking method used to maintain the track on the target, as well as outlining the method of initializing the track. This section also looks at the consistency of the tracker, important for evaluating the “credibility” of a collision warning. Section 4 discusses the method of declaring a warning of possible collision. Finally, Section 5 discusses why comparison of the extracted

measurements to GPS data (as well as possible hand-off of tracks between multiple cameras) is hampered by significant (and unknown) lens distortion.

Additionally, information on previous measurement extraction and target tracking methods, as well as measurement conversion formulas, can be found in the appendix.

## 2 Measurement Extractor

In order to track targets within the field of view from each frame of a camera, the measurements for each detected target must be extracted. For the purposes of tracking with a single camera, the measurements can remain pixel measurements and the tracking may be performed in the pixel space. Tracking with multiple cameras, however, would best be accomplished by tracking using azimuth and elevation measurements. In the absence of any distortion from the camera lens, the pixel measurements could be easily converted to azimuth and elevation measurements (see Appendix A). Distortion from the camera lens, however, will make the conversions much more difficult (see Section 5).

### 2.1 Extraction Algorithm

Previous methods of measurement extraction (outlined in Appendix F.1) either resulted in a large number of false measurements at the top of the frame or a number of missing measurements from true targets which are in the frame (although they are unintentional targets which appear at presumably much greater distances than the test target). In order to address this, another method of measurement extraction is proposed.

The neighborhood average for pixel  $i$ , denoted as  $\bar{I}_i$ , will be calculated as

$$\bar{I}_i = \frac{1}{L_1 L_2} \sum_{w \in W_i} I_w \quad (1)$$

where  $I_w$  is the intensity of pixel  $w$ ,  $L_1 L_2$  is the size of the window, and  $W_i$  is the set of pixels of the window centered at pixel  $i$ .

In addition to calculating the neighborhood average in a window, the standard deviation of the intensities in the window is also calculated. The



standard deviation in the window corresponding to the  $i$ th pixel is

$$\sigma_i = \left( \frac{1}{L_1 L_2} \sum_{w \in W_i} (I_w - \bar{I}_w)^2 \right)^{1/2} \quad (2)$$

where  $I_w$  is the intensity of pixel  $w$ ,  $L_1 L_2$  is the size of the window,  $W_i$  is the set of pixels in the sliding window centered at pixel  $i$ , and  $\bar{I}_w$  is given by (1).

A detection is now declared at pixel  $i$  if

$$|I_i - \bar{I}_i| > \alpha \sigma_i \quad (3)$$

where  $\alpha$  can be adjusted to tune the measurement extractor.

As a final step in extracting the measurements, the centroid of each group  $G$  of detected pixels is calculated. Detected pixels are grouped together if they share a side or corner (i.e., they are connected in a horizontal, vertical or diagonal direction, an “8-connected neighborhood”). The centroid for a group of pixels is calculated within a rectangular window  $W_G$  which includes a one-pixel border around the group  $G$ . The centroid, for one dimension, is

$$\hat{x}_c(G) = \frac{\sum_{i \in W_G} x_i I_i}{\sum_{i \in W_G} I_i} \quad (4)$$

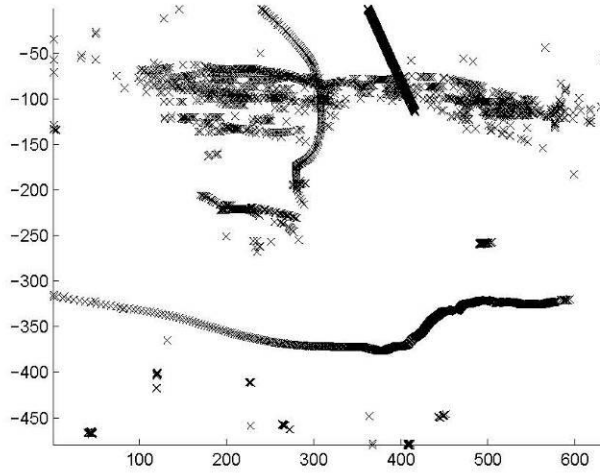
where  $x_i$  is the  $x$ -coordinate of pixel  $i$ ,  $I_i$  is the intensity of pixel  $i$ , and the group  $G$  of pixels  $i$  are those which have values from (3) which exceed the threshold and have been grouped together. A similar expression is used to calculate the  $y$ -coordinate of the centroid for group  $G$ .

Figure 1 shows the centroid measurements using (3),  $\alpha = 5$  and  $L_1 = L_2 = 101$ . Preliminary testing seems to favor a larger window for this particular measurement extractor. The use of such a large window, however, causes long computation times and a window of length 51 was used in later runs.

Additionally, extracted measurements which are found below the horizon can safely be ignored since there is no danger of collision with a target which is found to be below the horizon. This can help eliminate some false measurements arising from bright spots along the ground in some of the video data utilized here.

## 2.2 Second Stage Measurement Extraction

In addition to utilizing the method of measurement extraction outlined above, it is possible, in some circumstances, to further improve the measurement extraction by repeating a similar stage of measurement extraction. Since the



**Figure 1:** Measurements (in pixel coordinates) obtained from the extractor with the  $5\sigma$  rule (ultralight1\_archive.v1, scene 3, BAE camera)

idea behind this measurement extraction method is to search for pixel intensities which stand out from the background, the target pixels should not be included amongst the background pixels during detection. The problem, of course, is that detection must first be carried out in order to know which pixels should not be included within the background. In an attempt to mitigate this “catch-22” style process, a two stage measurement extraction may provide some benefit.

After the first round of detection is carried out in the manner outlined above, the detected pixels are eliminated from the calculation of the (1) and (2). A second stage of detection is carried out in exactly the same manner, except using the newly calculated  $\bar{I}_i$  and  $\sigma_i$ .

## 2.3 Variance of Extracted Measurements

### 2.3.1 Theoretical Measurement Noise Variance Calculation

Rather than simply make an assumption about the measurement noise variance, it is possible to evaluate the measurement noise variance during measurement extraction. The measurement noise variance in the case of an image centroid (equation (4) above) has been derived previously [1]. The measurement from the extractor (equation (4)) can be viewed as

$$\hat{x}_c = x_c + w_c \quad (5)$$

where  $x_c$  is the true image centroid in the  $x$ -coordinate and  $w_c$  is the (zero mean) centroid measurement noise. Furthermore, the measured pixel intensity is

$$I_i = s_i + n_i \quad (6)$$

where  $s_i$  is the true intensity of pixel  $i$  and  $n_i$  is the noise intensity in pixel  $i$ . The variance of the noise  $w_c$  in the centroid measurement can be evaluated in a window of the image as [1]

$$\sigma_c^2 = \frac{x_c^2}{r^2 + 1} + \frac{\sum_{i \in W_G} x_i^2}{m(r^2 + 1)} + \frac{\sum_{i \in W_G} s_i^2}{12(\sum_{i \in W_G} s_i)^2} \quad (7)$$

where  $m$  is the number of pixels in the window,  $r$  is the SNR in the window,  $I_i$  is the intensity of pixel  $i$ ,  $W_G$  is the rectangular window around the group  $G$  of pixels as in (4) (i.e., a single target), and  $x_c$  and  $x_i$  are measured using a coordinate system centered on the window. The value of the SNR in the window,  $r$ , is

$$r = \frac{\sum_{i \in W_G} s_i}{\sqrt{m}\sigma} \quad (8)$$

where  $\sigma$  is the standard deviation of the image noise.

Since the value  $s_i$  is not available directly, the following approximations can be used:

$$\sum_{i \in W_G} s_i^2 \approx \sum_{i \in W_G} I_i^2 - m\sigma^2 \quad (9)$$

$$\sum_{i \in W_G} s_i \approx \sum_{i \in W_G} I_i \quad (10)$$

All of the above equations assume that the noise intensity is zero mean, so the estimated noise mean must first be subtracted from the measured pixel intensities before calculating the centroid measurement variance.

### 2.3.2 Empirical Measurement Noise Variance Estimation

Rather than relying on theoretical calculations for the measurement variance of the centroid of an IR target, there is another possible method of variance estimation that can be used. Previously used to estimate the unknown measurement noise variance of radar systems (see [3]), this method uses multiple Interacting Multiple Model (IMM) estimators in order to estimate the unknown variance. The use of an IMM estimator is not specifically required by this method, however, IMM estimators often lead to very good tracking performance for maneuvering targets.

In order to estimate the unknown measurement variance, multiple IMM estimators (three in this case) must be run simultaneously, each with its own assumption for the measurement noise variance. Each estimator should also be identical except for the assumed measurement noise variances. For the scope of this work, the three estimators were set up with one using an appropriate initial variance, and the other two using scaled versions of that variance (50% and 150% of the assumed variance).

In order to determine the most likely measurement noise variance assumption, the likelihood of each estimator must be determined. Each IMM estimator calculates the probability of the system being in each mode assumed by the estimator (details on the IMM estimator can be found in [2]). The mode probabilities can then be used to evaluate a likelihood function for each IMM estimator.

The probability that, according to IMM number  $m$ , the system is in mode  $i$  at time  $k$ , given the data at time  $k - 1$ , with  $i = 1, \dots, r$  is

$$\mu_m^i(k|k-1) = \sum_{j=1}^r p_{ji} \mu_m^j(k-1) \quad m = 1, \dots, n \quad (11)$$

where  $\mu_m^j(k-1)$  is the probability of being in mode  $j$  at  $k-1$ , and  $p_{ji}$  is the probability of transition from mode (motion model)  $j$  to mode  $i$ .

The likelihood function for IMM estimator  $m$  at time  $k$  can then be written in terms of the likelihood functions for each mode of this IMM estimator and the above probabilities, namely [2],

$$\Lambda_m[z(k)] = \sum_{i=1}^r \mathcal{N}[z(k); \hat{z}_m^i(k|k-1), S_m^i(k)] \mu_m^i(k|k-1) \quad (12)$$

where  $\mathcal{N}[z(k); \hat{z}_m^i(k|k-1), S_m^i(k)]$  is a Gaussian pdf that represents the likelihood function of mode  $i$  of IMM  $m$  at time  $k$ ,  $\hat{z}_m^i$  is the predicted measurement

for filter  $i$  and  $S_m^i$  is the innovation covariance of filter  $i$ . In other words, the likelihood function of the IMM estimator is the sum of the likelihood functions of each filter multiplied by the one-step predicted probability of being in that mode.

As more data are obtained, the likelihood function for each IMM estimator can be updated in the form of a cumulative likelihood function, given as

$$\Lambda_m^{k_2} = \prod_{k=k_1}^{k_2} \Lambda_m[z(k)] \quad (13)$$

where  $k_1$  is the starting time and  $k_2$  is the ending time. The probability of the  $m$ th IMM estimator (measurement model  $M_m$ ) having the correct variance assumptions given the data up to and including  $k_2$  can then be obtained as

$$\beta_m \triangleq P\{M_m|Z^{k_2}\} = \frac{\Lambda_m^{k_2}}{\sum_{m=1}^{N_m} \Lambda_m^{k_2}} \quad (14)$$

which assumes a uniform prior.

The probability from each estimator can then be used as a weighting to arrive at the estimated measurement noise variance, i.e.,

$$\hat{\sigma}_e^2 = \sum_{m=1}^n \beta_m \sigma_{e_m}^2 \quad (15)$$

where  $n$  is the number of IMM estimators used ( $n = 3$ , in our case). This variance can then be used by the “center” estimator, while the others use scaled versions of the newly calculated value. This process continues as the estimators track each target and result in a continuously updated measurement noise variance.

A method of measurement noise variance estimation such as this is necessary for tracking in this passive collision warning system due to the non-stationary nature of the measurement noise. For example, as targets move closer or farther from the camera, the measurement noise will change as the target’s energy is spread over a different number of pixels. Additionally, as the target moves throughout the scene, the environment will have differing effects on the target detection and measurement noise.

### 3 Target Tracker

Once the measurements corresponding to each detection centroid in a frame of data are obtained, the tracker can use these measurements to start tracks and estimate target trajectories. The target state consists of position, velocity and acceleration in the focal plane (FP). Currently, a nearest neighbor approach is utilized to assign measurements to tracks. Each currently running track is assigned the measurement which is closest to the predicted measurement location (provided it falls within a validation region centered at the predicted measurement [1]). Currently a  $5\sigma$  validation gate is applied to the measurements. The number of measurements in a validation gate is rarely greater than one, so using a measurement assignment method more complex than the nearest neighbor approach is not necessary. Once measurements are assigned to the currently running tracks, each track is updated via an IMM estimator [2] utilizing two Kalman filters which assume appropriate motion models.

#### 3.1 Target Motion Models

##### 3.1.1 Autocorrelated Process Noise Model

Standard nearly constant velocity (NCV) and nearly constant acceleration (NCA) motion models assume that the process noise (acceleration in the NCV model and acceleration increment in the NCA model) can be treated as white. In the case of video data, the sampling time is 1/30 s, and the white process noise assumption becomes unrealistic. The accelerations the target undergoes clearly must be correlated between samples when the sampling time is very small. For this reason an autocorrelated process noise model will provide higher quality target tracking than NCV or NCA motion models.

Specifically, the autocorrelated process noise model used here models the target accelerations as an exponentially autocorrelated noise with zero mean [2]. The autocorrelation of the target acceleration  $a(t)$  is therefore

$$E[a(t)a(t+\tau)] = \sigma_m^2 e^{-\alpha|\tau|} \quad \alpha > 0 \quad (16)$$

where  $\sigma_m^2$  is the instantaneous variance of the acceleration and  $1/\alpha$  is the time constant of the target acceleration autocorrelation. For this model, the state equation will be

$$x(k+1) = Fx(k) + v(k) \quad (17)$$

where

$$\begin{aligned}
F &= \begin{bmatrix} 1 & T & (\alpha T - 1 + e^{-\alpha T})/\alpha^2 & 0 & 0 & 0 \\ 0 & 1 & (1 - e^{-\alpha T})/\alpha & 0 & 0 & 0 \\ 0 & 0 & e^{-\alpha T} & 0 & 0 & 0 \\ 0 & 0 & 0 & 1 & T & (\alpha T - 1 + e^{-\alpha T})/\alpha^2 \\ 0 & 0 & 0 & 0 & 1 & (1 - e^{-\alpha T})/\alpha \\ 0 & 0 & 0 & 0 & 0 & e^{-\alpha T} \end{bmatrix} \\
&\approx \begin{bmatrix} 1 & T & 0 & 0 & 0 & 0 \\ 0 & 1 & T & 0 & 0 & 0 \\ 0 & 0 & 1 - \alpha T & 0 & 0 & 0 \\ 0 & 0 & 0 & 1 & T & 0 \\ 0 & 0 & 0 & 0 & 1 & T \\ 0 & 0 & 0 & 0 & 0 & 1 - \alpha T \end{bmatrix}
\end{aligned} \tag{18}$$

Additionally, the process noise  $v(k)$  will have a covariance matrix of

$$Q = 2\alpha\sigma_m^2 \begin{bmatrix} T^5/20 & T^4/8 & T^3/6 & 0 & 0 & 0 \\ T^4/8 & T^3/3 & T^2/2 & 0 & 0 & 0 \\ T^3/6 & T^2/2 & T & 0 & 0 & 0 \\ 0 & 0 & 0 & T^5/20 & T^4/8 & T^3/6 \\ 0 & 0 & 0 & T^4/8 & T^3/3 & T^2/2 \\ 0 & 0 & 0 & T^3/6 & T^2/2 & T \end{bmatrix} \tag{19}$$

A value of  $\alpha = 2 \text{ s}^{-1}$  was deemed appropriate for both motion models of the IMM estimator as it results in a decorrelation time of roughly 1 second.

### 3.2 Choice of the Process Noise Level

The standard deviation of the process noise,  $\sigma_m$ , should be chosen to cover the expected accelerations of the targets. Early tests were run using three scenes of an ultralight aircraft passing over the camera. The supplied data for the BAE camera was examined to determine the test target's accelerations both near to and far from the camera. The position of the test target was found over two one-second intervals in order to estimate the velocity and acceleration of the target, the difference in position providing velocity and the difference of two velocity estimates providing the acceleration estimate. The estimated accelerations are shown in Table 1. Scene 4 was estimated to

Ultralight1_Archive.vl BAE Camera	Near Camera	Far From Camera
Scene 2	$ \hat{a}  = \begin{pmatrix} 4.2 \\ 1.2 \end{pmatrix}$	$ \hat{a}  = \begin{pmatrix} 0.8 \\ 0.3 \end{pmatrix}$
Scene 3	$ \hat{a}  = \begin{pmatrix} 54.39 \\ 11.4 \end{pmatrix}$	$ \hat{a}  = \begin{pmatrix} 0.7 \\ 0.8 \end{pmatrix}$
Scene 4	$ \hat{a}  = \begin{pmatrix} 32.3 \\ 0 \end{pmatrix}$	$ \hat{a}  = \begin{pmatrix} 0.4 \\ 0.2 \end{pmatrix}$

**Table 1:** Estimated acceleration of the test target from the BAE Camera in various scenes

have a zero acceleration in the  $y$  direction for the “near camera” section since the velocity estimates were found to be equal in that portion of the video.

Based on the estimated accelerations of the test target, a value of  $\sigma_m = 10$  pixels/s<sup>2</sup> was used in some simulations on Scene 3 using a single Kalman filter with an autocorrelated process noise model with  $\alpha = 0.5 \text{ s}^{-1}$ . The difference in acceleration values between the near and far targets as well as between different scenes, however, suggested that a multiple model approach would be needed eventually for better tracking across different scenarios.

In the case of the IMM estimator which utilized two autocorrelated process noise models, parameters of  $\alpha_1 = \alpha_2 = 2 \text{ s}^{-1}$  and  $\sigma_{m1}^2 = 25$  and  $\sigma_{m2}^2 = 2$  were used. It should be noted that, at this stage, the L3 camera was used exclusively; and the lower resolution of the L3 camera, as well as the different  $\alpha$  values, leads to the use of different process noise levels. In general, for an autocorrelated process noise motion model, the choice of  $\sigma_m$  is related to the process noise,  $q$ , of a white noise acceleration (WNA) model by [2]

$$\frac{2}{\alpha} \sigma_m^2 = q \quad (20)$$

### 3.3 Track Initialization

In order to initialize tracks, a validation gate (in pixel space), based on the assumed maximum velocity of a target over one sampling period, is set up for each measurement location for the potential tracks. Originally, the assumed maximum velocity of 100 pixels/s in the  $x$ -direction and 50 pixels/s in the



$y$ -direction was used when the target was entering the camera frame at a relatively close distance (and was therefore much larger in number of pixels). The maximum velocity assumption is important only for track initialization, however; and for a realistic scenario, a target of interest will be initialized at a much greater distance, and will therefore have a much smaller maximum velocity in pixel space. For this reason, the track formation using maximum velocity assumptions of 10 or 20 pixels/s (in both  $x$  and  $y$  directions) are likely more reasonable.

Additionally, instead of insisting that two consecutive measurements be found (as described in section Appendix H.1), the track initialization will instead look for three valid measurements within five sampling intervals. This amounts to an  $M/N$  logic [1] with  $M = 3$ ,  $N = 5$  and will allow for intermittent detection of a target which is a large distance from the camera. In this case, the validation gate must be increased when there is a missed detection. The increased gate size should not cause difficulties for the tracker as the initial gate is small due to the assumption of the target being at far distances (when track initialization should be taking place) and therefore appearing as a small low-maneuvering target. For the case of “three out of five” track initialization, the validation gate will cover, at worst, three times the maximum velocity over a single sampling interval.

Following track maintenance (see section 3.4) all the remaining measurements in the frame are used to initialize new possible tracks. All unassigned measurements from a frame are saved as starting points for new potential tracks at the next sampling time.

### 3.3.1 Comparison of Track Initialization Methods

Table 2 compares the number of tracks formed and time of track confirmation for each of the track initialization procedures (2/2 and 3/5 logic). The track initialization was run using the data from the BAE camera, movie file “Ultralight 1\_Archive.vl,” scene 3, the measurement extractor with window length 51 and a  $5\sigma$  threshold, and the older WPA motion model (see section Appendix G.1).

In each case, the test target track was always formed and the extra tracks were the result of measurements that are the result of intermittent bright spots along the tree line or clouds, or the result of a flock of birds passing through the camera frame (e.g., the upper part of Figure 1).

	$[\dot{x}_{max}, \dot{y}_{max}]$ (in pixels/s)		
Number of Tracks	[100, 50]	[20, 20]	[10, 10]
2/2 Initiator	491	140	137
3/5 Initiator	320	81	77
<b>Test Track Confirmation Frame</b>			
2/2 Initiator	1888	1888	1888
3/5 Initiator	1887	1887	1887

**Table 2:** Comparison of number of tracks formed for various track initialization procedures

### 3.4 Track Maintenance

Once potential tracks have been confirmed, they are treated as if they are a true track. A validation gate is set up at each currently running track's predicted measurement location. The closest measurement to the predicted measurement location that falls within the validation gate is assigned to that track. The measurement is then used in an IMM estimator, which passes the measurement to two standard Kalman filters with autocorrelated process noise models as discussed in 3.1. After the currently running tracks are assigned measurements and propagated, the remaining measurements of the frame are used in initialization of new tracks or saved as potential starting points of new tracks for the next frame. If a track does not have a measurement assigned to it, the track will be propagated "open-loop." If four consecutive missed detections occur, the track will be terminated.

### 3.5 Distance at Track Confirmation

In order to determine the distance at which the test flight target is acquired, the frame number at track confirmation is recorded. The timestamp of that frame can then be compared to available GPS data to determine the location of the target of interest. Use of the equations of Appendix C, with the camera location as the origin, will result in the ENU vector of the target at the time of track confirmation. Simply taking the magnitude of this vector results in the distance from the camera to the target.

The following distances of track confirmation utilize a measurement extractor with  $L_1 = L_2 = 51$  and  $5\sigma$  threshold, and a single filter tracker with

autocorrelated motion model with  $\alpha = 0.5 \text{ s}^{-1}$  and  $\sigma_m = 10 \text{ pixels/s}^2$ . The camera is assumed to be located at  $39^\circ 32' 31.82''$  N latitude,  $75^\circ 18' 14.5''$  W longitude and 0 elevation (in the absence of altitude information). The distance at track confirmation using the BAE camera is shown in table 3 (Note: the video is played backwards to simulate a target approaching the camera rather than flying away from the camera).

BAE Camera	Confirmation Frame	GPS Coordinates	Distance
Scene 2	1814	$39^\circ 33' 2.9375''$ N $75^\circ 18' 19.9005''$ W 305 ft	973 m
Scene 3	1887	$39^\circ 33' 1.8832''$ N $75^\circ 18' 20.1322''$ W 291 ft	941 m
Scene 4	2657	$39^\circ 33' 25.7443''$ N $75^\circ 18' 31.3793''$ W 669 ft	1,723 m

**Table 3:** Distance to target of interest at track confirmation for various scenes

### 3.6 Target Tracker Consistency

Since the estimated state from the target tracker will be utilized to test whether or not a target is on an impending collision course, it is important that the target tracker be consistent<sup>1</sup> [2]. Since the consistency must be tested from a single run (since the tracker is operating on real data) the consistency of the target tracker must be tested with the normalized innovation squared (NIS). The normalized innovation squared is

$$\epsilon_\nu(k) = \nu(k)' S(k)^{-1} \nu(k) \quad (21)$$

where  $\nu(k)$  is the innovation at time  $k$  and  $S(k)$  is the innovation covariance at time  $k$ . If the filter is consistent, the NIS will have a chi-square distribution with  $n_z$  degrees of freedom, where  $n_z$  is the dimension of the measurement

---

<sup>1</sup>Consistency of a state estimator is the requirement that its calculated state estimate variances are statistically compatible with the actual errors.

(in our case,  $n_z = 2$ ). In order to test from a single run, the time-averaged NIS

$$\bar{\epsilon}_\nu = \frac{1}{K} \sum_{k=1}^K \nu(k)' S(k)^{-1} \nu(k) \quad (22)$$

may be used, where  $K\bar{\epsilon}_\nu$  follows a chi-square distribution with  $Kn_z$  degrees of freedom [2]. In the case of a time-averaged NIS over 100 samples, the 95% confidence region will be between 1.63 and 2.41.

In the case of an IMM estimator, there are two (or more, in general) differing motion models, which each result in different values for (21). In this case, the NIS will be approximated as a combination of each mode's NIS,  $\epsilon_{\nu i}(k)$ , where

$$\epsilon_{\nu i}(k) = \nu_i(k)' S_i(k)^{-1} \nu_i(k) \quad (23)$$

and  $\epsilon_\nu$  will be expressed as

$$\epsilon_\nu(k) = \sum_{i=1}^r \mu^i(k) \epsilon_{\nu i}(k) \quad (24)$$

where  $r$  is the number of modes in the IMM estimator and  $\mu^i$  is the probability that the system is in mode  $i$ . The time-averaged NIS can now be calculated as before, using (24) in place of (21).

### 3.6.1 Fixed Centroid Measurement Noise

Figure 2 shows the sliding window time-averaged NIS for a single model filter using an autocorrelated process noise model with  $\alpha = 0.5 \text{ s}^{-1}$ ,  $\sigma_m = 10 \text{ pixels/s}^2$ , and  $\sigma_c = 0.5 \text{ pixel}$ . Figure 3 shows the time-averaged NIS with the same parameters, except that measurement noise standard deviation  $\sigma_c = 0.1 \text{ pixel}$ . Both filters were run on the data from Scene 3 from the BAE camera. Both figures show the time-averaged NIS over a sliding window of 100 samples.

When the measurement noise standard deviation is taken as 0.5 pixels, the average NIS is clearly far from the values expected for a 100 sample average NIS. Since the NIS is much lower than expected, the innovation covariance must be too large, suggesting that the measurement noise standard deviation was too large. When the measurement noise standard deviation is lowered to 0.1 pixels, the average NIS takes on values much closer to what is expected. Furthermore, the movement of the NIS may also suggest that the measurement noise standard deviation may vary throughout the scene. If

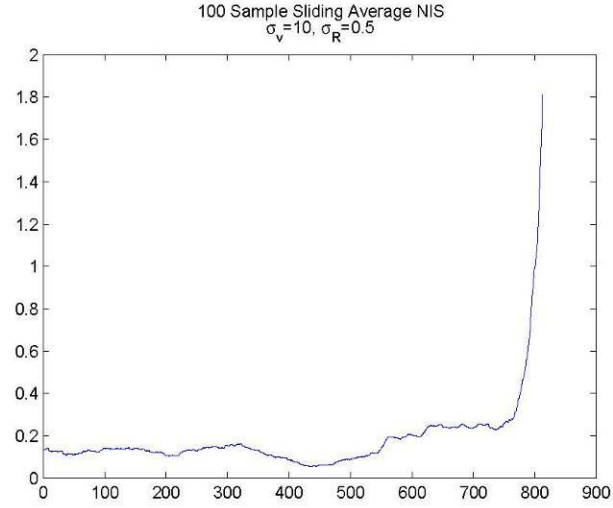


**Figure 2:** 100 Sample sliding window time-averaged NIS with  $\sigma_m = 10 \text{ pixels/s}^2$ ,  $\sigma_c = 0.5 \text{ pixel}$

the measurement noise does indeed change depending on the scenario, then a tracker which can adapt to these changes would be preferable.

Figures 4 and 5 show the sliding window time-average NIS for a single model filter with an autocorrelated process noise model with  $\alpha = 0.5 \text{ s}^{-1}$ ,  $\sigma_m = 2.5 \text{ pixels/s}^2$ , and  $\sigma_c$  calculated using (7). Figure 4 uses data from camera B, scene “Loop 1” of the “Piper1.vl” movie file. Figure 5 uses the data from camera A of the same scene.

### 3.6.2 Dynamically Determined Centroid Measurement Noise

By using the theoretical calculations for the variance of the centroid measurement noise (equation (7)), the tracker can utilize a measurement noise standard deviation which is free to change throughout the scenario. Additionally, since the tracker is evaluating the measurement noise from the data, each camera will be able adjust to the particular view it has of the target.

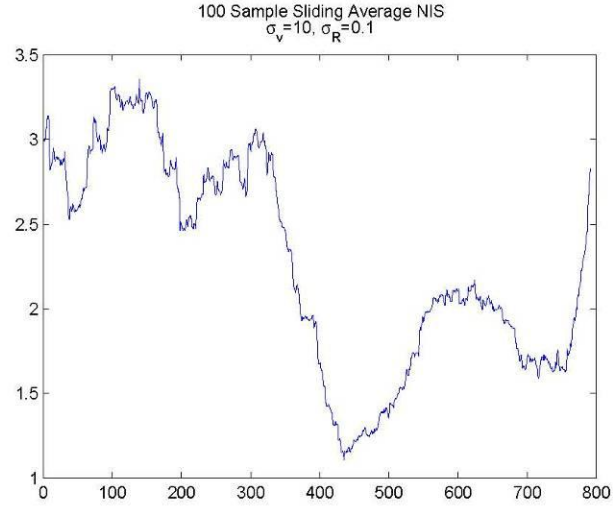


**Figure 3:** 100 Sample sliding window time-averaged NIS with  $\sigma_m = 10 \text{ pixels/s}^2$ ,  $\sigma_c = 0.1 \text{ pixel}$

Different cameras may detect a different number of pixels for each target, for example, so the centroid measurement noise shouldn't be assumed to be the same across cameras.

## 4 Threshold Test for Collision Course

Lacking any range information, the only way to test whether the target is on a collision course is to examine the estimated angular (LOS) velocity of the target. For the case of tracking a target in pixel space, the velocity estimates in the two pixel dimensions ( $\dot{x}$  and  $\dot{y}$ ) can be used. A target which has an estimated angular velocity near zero can be assumed to be on a collision course. As long as either  $\dot{x}$  or  $\dot{y}$  is estimated to be far enough from zero (greater than  $3\sigma$  away), no collision will be declared. In order to set a threshold for declaration of an impending collision, the filter-calculated track

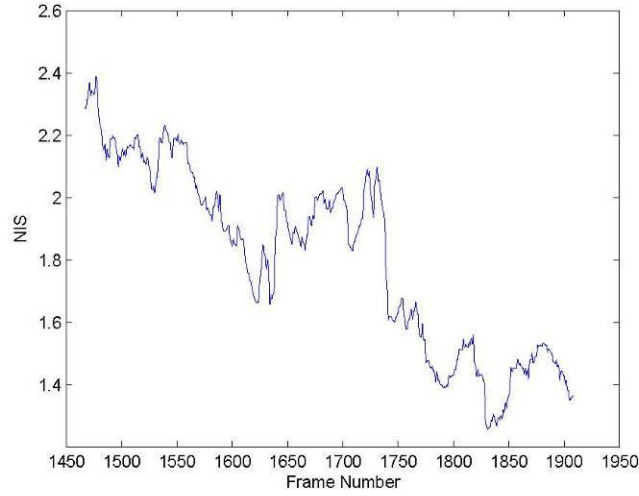


**Figure 4:** 100 Sample sliding window time-averaged NIS with  $\sigma_m = 2.5 \text{ pixels/s}^2$ ,  $\sigma_c$  calculated, camera B

covariance will be used to compare the estimated velocity to its standard deviation.

Figures 6 and 7 show example plots of  $\frac{\hat{x}}{\sigma_{\hat{x}}}$  and  $\frac{\hat{y}}{\sigma_{\hat{y}}}$ , respectively, with the dashed lines denoting the  $3\sigma$  boundaries. The data in this case is from a single model tracker using autocorrelated process noise with a measurement noise standard deviation,  $\sigma_c$ , assumed to be 0.1, which results in the more consistent filter as seen in figure 3. When *both estimated velocities* are found to be within  $3\sigma$  of zero, a collision could be declared. As the track continues, however, it is clear that no collision will occur as at least one of the estimated velocities is more than  $3\sigma$  away from zero. In this case, the estimate of  $\dot{x}$  is almost never within  $3\sigma$  of zero, so there will be no collision warning from this target.

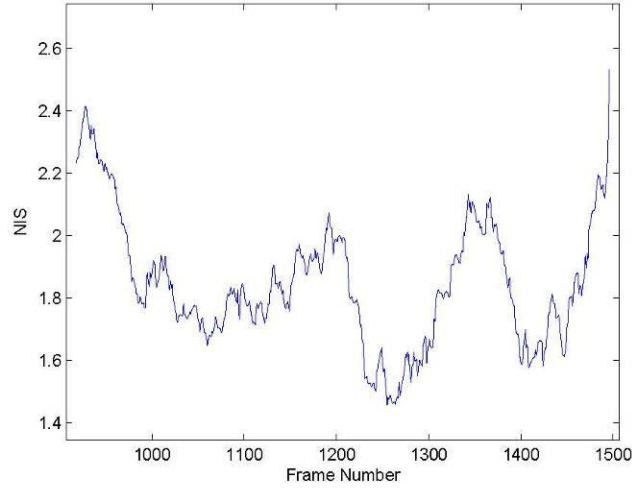


**Figure 5:** 100 Sample sliding window time-averaged NIS with  $\sigma_m = 2.5 \text{ pixels/s}^2$ ,  $\sigma_c = \text{calculated}$ , camera A

## 5 Comparison Between Calculated Track and GPS in LOS Space

In order to compare the extracted measurements and the calculated track to the available GPS data of the target, the measurements must be converted from pixel space to LOS space. Appendix A–Appendix D outline the necessary calculations and conversions for comparing the calculated track to GPS. These are done assuming a distortionless lens where a pixel location can be converted directly to a LOS angle.

Additionally, the camera boresight angles and the roll of the camera can be estimated by comparing the measurements from the camera to the available GPS data. Figure 8 shows the GPS data from the Piper1.vl file scene “Loop 1” in azimuth and elevation angles as well as the measurements from camera B converted to azimuth and elevation angles. The offset of the two



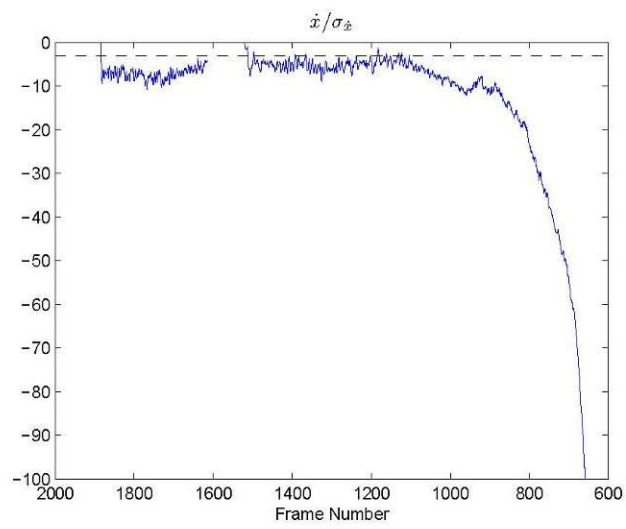


**Figure 6:** Collision threshold test on the estimate  $\dot{x}$  — ratio of the velocity estimate to its standard deviation estimate: “non-zero velocity estimate”  $\Rightarrow$  “no collision”

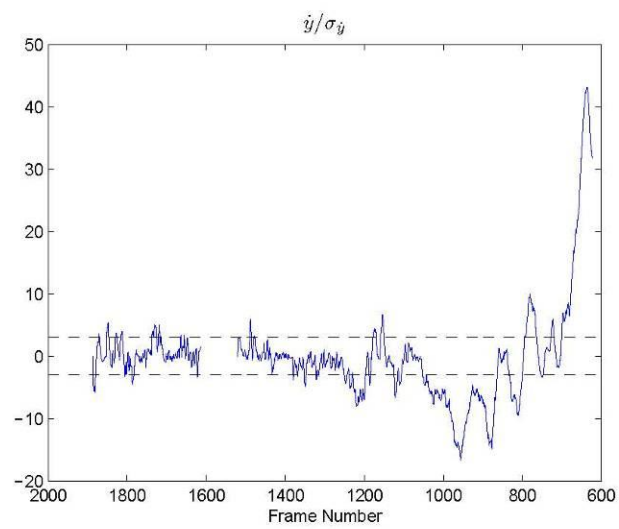


**Figure 7:** Collision threshold test on the estimate  $\dot{y}$  — ratio of the velocity estimate to its standard deviation estimate

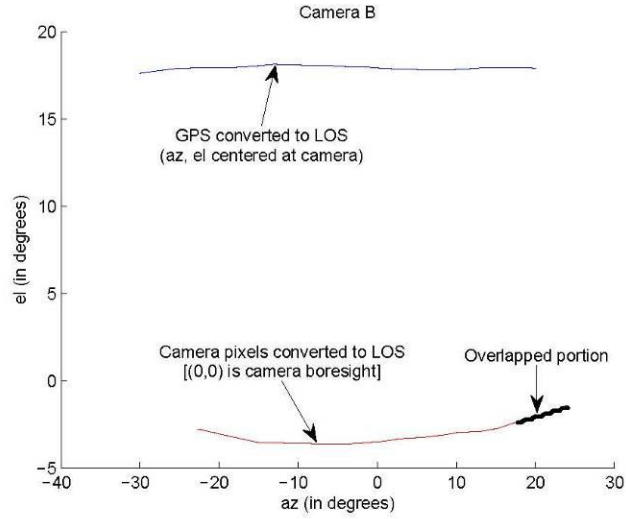


**Figure 8:** Comparison of GPS data with measurement conversions to LOS, Camera B, Piper1, Loop 1

plots represent the azimuth and elevation angles of the camera boresight as well as a possible non-zero roll angle of the camera. Figure 9 shows similar data for the same scene with camera A. Both figures also highlight the portions of the data for which the frames of the two cameras are overlapped.

Unfortunately, in both cameras, there is a “barrel” distortion clearly present at the edges of the frame, which causes the converted camera pixel measurements to match poorly to the LOS based on GPS data. This causes the overlapped portion of the two cameras to exhibit a small amount of roll when in fact camera A is rolled a great deal with respect to camera B. The distortion at the edge of the frames, therefore, will hamper relative registration and there can be no handoff of target tracks from one camera to the other. Additionally, comparison to GPS data is not possible, due to the unknown distortion mapping between apparent focal plane and true azimuth/elevation coordinates, this discrepancy being largest near the image boundaries.

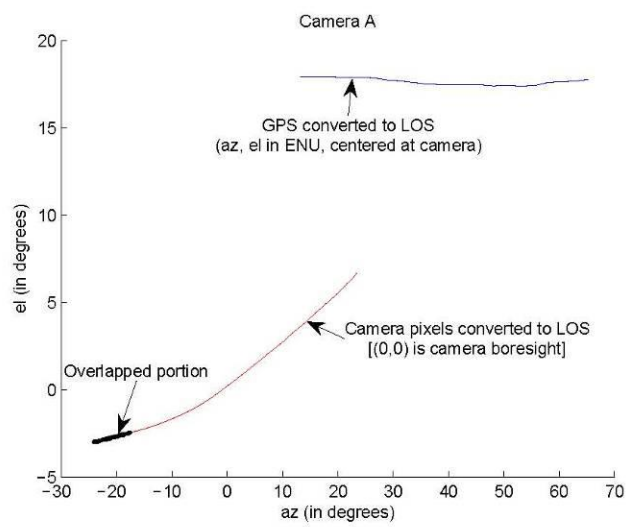


**Figure 9:** Comparison of GPS data with measurement conversions to LOS, Camera A, Piper 1, Loop 1

## APPENDIX

### Appendix A Conversion of pixel location to azimuth and elevation

We wish to convert measurements in pixel space to measurements in angle space. The following derivation shows the conversion of pixel  $(x, y)$  to azimuth and elevation angles  $\alpha$  and  $\epsilon$ , respectively (measured about the frame boresight). For an image of width  $N_x$  pixels and height  $N_y$  pixels, the cartesian coordinates of a pixel will be numbered left to right ( $x = 1, \dots, N_x$ ) and bottom to top ( $y = 1, \dots, N_y$ ). More traditional pixel location representation (the  $[1,1]$  pixel located in the top left corner of the image) can be used by simply utilizing the transformation  $x_i = x$  and  $y_i = N_y - y + 1$ . The camera is assumed to have a horizontal aperture angle  $A_x$  and vertical aperture angle  $A_y$ , focal length of  $f$ , and square pixels of width  $p$ .

The distance to the rightmost edge of the image is given as

$$\frac{1}{2}N_x p = f \tan \frac{A_x}{2} \quad (25)$$

and the horizontal distance to the center of pixel  $(x, y)$  is

$$\left(x - \frac{N_x}{2} - \frac{1}{2}\right)p = f \tan \alpha \quad (26)$$

Now using (25) and (26) we have

$$\alpha = \tan^{-1} \left( \tan \left( \frac{A_x}{2} \right) \left( \frac{2x - N_x - 1}{N_x} \right) \right) \quad (27)$$

In a similar fashion the distance to the topmost edge of the image is given as

$$\frac{1}{2}N_y p = f \tan \frac{A_y}{2} \quad (28)$$

The vertical distance to the center of pixel  $(x, y)$  is

$$\left(y - \frac{N_y}{2} - \frac{1}{2}\right)p = f \frac{\tan \epsilon}{\cos \alpha} \quad (29)$$

where  $\alpha$  is taken from (27). Relating (28) and (29) we now have

$$\epsilon = \tan^{-1} \left( \tan \left( \frac{A_y}{2} \right) \cos(\alpha) \frac{2y - N_y - 1}{N_y} \right) \quad (30)$$

Now that we have the measurement in terms of azimuth and elevation in the Focal Plane (FP) frame, we wish to express the measurement as a line-of-sight (LOS) unit vector in the FP coordinate system. The LOS unit vector relative to the FP-xyz frame is

$$\text{LOS} = \mathbf{1}_x L_x + \mathbf{1}_y L_y + \mathbf{1}_z L_z \quad (31)$$

where  $L_x = \cos \epsilon \sin \alpha$ ,  $L_y = \sin \epsilon$  and  $L_z = \cos \epsilon \cos \alpha$ .

## Appendix B Conversion of LOS in FP coordinate system to local ENU coordinate system

Next we must convert the line of sight (LOS) vector in the focal plane (FP) coordinates to east-north-up (ENU) coordinates (centered at the camera) in order to compare the track with GPS information. We first assume that the frame boresight has an elevation of  $\epsilon_F$  (above the horizontal), an azimuth angle of  $\alpha_F$  (in the horizontal plane clockwise from north), and a roll angle of  $\rho_F$  (in the vertical plane clockwise from up). In order to transform between FP frame coordinates and ENU coordinates we first assume that the frame  $(\mathbf{1}_{x'''}, \mathbf{1}_{y'''}, \mathbf{1}_{z'''})$  coincides with  $\mathbf{1}_E, \mathbf{1}_N$  and  $\mathbf{1}_U$ . Using three rotations, we can transform any FP frame of given azimuth, elevation and roll to local ENU coordinates.

First, a rotation of  $180 - \alpha_F$  along  $\mathbf{1}_{z'''}$  yields an azimuth pointing of  $\alpha_F$ . This rotation is given as

$$\begin{aligned} \mathbf{1}_{x''} &= \mathbf{1}_{x'''} \cos(180 - \alpha_F) + \mathbf{1}_{y'''} \cos(\alpha_F - 90) \\ &= \mathbf{1}_{x'''} (-\cos \alpha_F) + \mathbf{1}_{y'''} \sin \alpha_F \end{aligned} \quad (32)$$

$$\begin{aligned} \mathbf{1}_{y''} &= \mathbf{1}_{x'''} \cos(90 + 180 - \alpha_F) + \mathbf{1}_{y'''} \cos(180 - \alpha_F) \\ &= \mathbf{1}_{x'''} (-\sin \alpha_F) + \mathbf{1}_{y'''} (-\cos \alpha_F) \end{aligned} \quad (33)$$

$$\mathbf{1}_{z''} = \mathbf{1}_{z'''} \quad (34)$$

Next, a rotation of  $90 - \epsilon_F$  along  $\mathbf{1}_{x''}$  tilts the frame to an elevation of  $\epsilon_F$ . This rotation is given as

$$\mathbf{1}_{x'} = \mathbf{1}_{x''} \quad (35)$$

$$\begin{aligned}\mathbf{1}_{y'} &= \mathbf{1}_{y''} \cos(90 - \epsilon_F) + \mathbf{1}_{z''} \cos(\epsilon_F) \\ &= \mathbf{1}_{y''} \sin \epsilon_F + \mathbf{1}_{z''} \cos \epsilon_F\end{aligned}\quad (36)$$

$$\begin{aligned}\mathbf{1}_{z'} &= \mathbf{1}_{y''} \cos(180 - \epsilon_F) + \mathbf{1}_{z''} \cos(90 - \epsilon_F) \\ &= \mathbf{1}_{y''} (-\cos \epsilon_F) + \mathbf{1}_{z''} \sin \epsilon_F\end{aligned}\quad (37)$$

Finally, a rotation of  $\rho_F$  around  $\mathbf{1}_{z'}$  tilts the frame to the proper roll angle. This rotation is given as

$$\mathbf{1}_x = \mathbf{1}_{x'} \cos \rho_F + \mathbf{1}_{y'} \sin \rho_F \quad (38)$$

$$\begin{aligned}\mathbf{1}_y &= \mathbf{1}_{x'} \cos(90 + \rho_F) + \mathbf{1}_{y'} \cos \rho_F \\ &= -\mathbf{1}_{x'} \sin \rho_F + \mathbf{1}_{y'} \cos \rho_F\end{aligned}\quad (39)$$

$$\mathbf{1}_z = \mathbf{1}_{z'} \quad (40)$$

Combining these rotations together we have the transformation of the measurements of azimuth and elevation angles within the FP frame to a LOS unit vector in ENU coordinates. The full transformation is given as

$$\mathbf{LOS} = \begin{bmatrix} L_x & L_y & L_z \end{bmatrix} \begin{bmatrix} \mathbf{1}_x \\ \mathbf{1}_y \\ \mathbf{1}_z \end{bmatrix} \quad (41)$$

$$= \begin{bmatrix} L_x & L_y & L_z \end{bmatrix} T_3 \begin{bmatrix} \mathbf{1}_{x'} \\ \mathbf{1}_{y'} \\ \mathbf{1}_{z'} \end{bmatrix} \quad (42)$$

$$= \begin{bmatrix} L_x & L_y & L_z \end{bmatrix} T_3 T_2 \begin{bmatrix} \mathbf{1}_{x''} \\ \mathbf{1}_{y''} \\ \mathbf{1}_{z''} \end{bmatrix} \quad (43)$$

$$= \begin{bmatrix} L_x & L_y & L_z \end{bmatrix} T_3 T_2 T_1 \begin{bmatrix} \mathbf{1}_{x'''} \\ \mathbf{1}_{y'''} \\ \mathbf{1}_{z'''} \end{bmatrix} \quad (44)$$

$$= \begin{bmatrix} L_x & L_y & L_z \end{bmatrix} T_3 T_2 T_1 \begin{bmatrix} \mathbf{1}_E \\ \mathbf{1}_N \\ \mathbf{1}_U \end{bmatrix} \quad (45)$$

$$\begin{bmatrix} L_E & L_N & L_U \end{bmatrix} = \begin{bmatrix} L_x & L_y & L_z \end{bmatrix} T_3 T_2 T_1 \quad (46)$$

where

$$T_3 = \begin{bmatrix} \cos \rho_F & \sin \rho_F & 0 \\ -\sin \rho_F & \cos \rho_F & 0 \\ 0 & 0 & 1 \end{bmatrix} \quad (47)$$



$$T_2 = \begin{bmatrix} 1 & 0 & 0 \\ 0 & \sin \epsilon_F & \cos \epsilon_F \\ 0 & -\cos \epsilon_F & \sin \epsilon_F \end{bmatrix} \quad (48)$$

$$T_1 = \begin{bmatrix} -\cos \alpha_F & \sin \alpha_F & 0 \\ -\sin \alpha_F & -\cos \alpha_F & 0 \\ 0 & 0 & 1 \end{bmatrix} \quad (49)$$

## Appendix C Conversion of GPS coordinates to local ENU

In order to evaluate the accuracy of tracking, GPS measurements from test targets will be provided along with the video data from the cameras used. In order to properly compare this data, the GPS coordinates must be transformed into the same ENU coordinate system used for the measurement conversion (ENU centered at camera). In order to convert geodetic (GPS) measurements to ENU coordinates, we must first convert the measurements (as well as the GPS coordinates of the origin) to earth-centered earth-fixed (ECEF) coordinates.

For GPS coordinates of height  $h$ , latitude  $\lambda$ , and longitude  $\phi$ , the ECEF coordinates  $(x, y, z)$  are given by

$$x = (h + N) \cos \lambda \cos \phi \quad (50)$$

$$y = (h + N) \cos \lambda \sin \phi \quad (51)$$

$$z = (h + (1 - e^2)N) \sin \lambda \quad (52)$$

where  $N = \frac{a}{\sqrt{1-e^2 \sin^2 \lambda}}$ ,  $e = 8.1819191 \times 10^{-2}$  (eccentricity term) and  $a = 6378137$  (semimajor axis of earth, in meters).

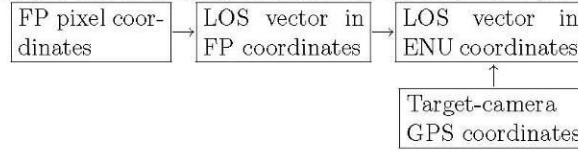
The conversion of ECEF coordinates  $(x, y, z)$  to local ENU coordinates  $(e, n, u)$  is given by

$$\begin{bmatrix} e \\ n \\ u \end{bmatrix} = \begin{bmatrix} -\sin \phi & \cos \phi & 0 \\ -\cos \phi \sin \lambda & -\sin \lambda \sin \phi & \cos \lambda \\ \cos \lambda \cos \phi & \cos \lambda \sin \phi & \sin \lambda \end{bmatrix} \cdot \begin{bmatrix} x - x_0 \\ y - y_0 \\ z - z_0 \end{bmatrix} \quad (53)$$

where  $(x_0, y_0, z_0)$  is the origin of the local ENU coordinate system in ECEF coordinates, given by (50)–(52) with  $h = h_0$ ,  $\lambda = \lambda_0$ ,  $\phi = \phi_0$ , the GPS coordinates of the camera.

## Appendix D Comparison of track from camera to GPS information

The overall procedure for comparing the track generated from the camera measurements to the GPS information follows the flow chart provided here.



Also, note that once the GPS coordinates of the target are converted to ENU coordinates (with the origin centered at the camera) the distance from camera to target is simply the magnitude of the ENU vector of the target.

## Appendix E Positioning of two fixed cameras for PCAS

In order to calculate the azimuth overlap in field of view (FOV) of two cameras (assumed to have the same boresight elevation angles), their pointing angles ( $p_1$ ,  $p_2$  in Figure 10, assumed given in degrees) must be known. The overlap  $\epsilon$  (in degrees) of the two cameras is

$$\epsilon = p_1 + \frac{\alpha_1}{2} - \left( p_2 - \frac{\alpha_2}{2} \right) \quad (54)$$

where  $\alpha_1$  and  $\alpha_2$  are the horizontal FOV of each camera, and  $p_1$ ,  $p_2$  are their boresight angles (measured clockwise with respect to the perpendicular on the base  $L$ ).

For two cameras separated by a distance  $L$ , the distance  $d$  in Figure 10 (the distance from the cameras to the intersection of their fields of view) is, for  $\epsilon < 0.1\text{rad} \approx 6^\circ$

$$d = \frac{L}{\epsilon} \quad (55)$$

with  $\epsilon$  in radians.

Assuming the separation base  $L = 2$  feet,  $\alpha_1 = \alpha_2 = 45^\circ$ , and the two cameras are pointed symmetrically with respect to the perpendicular on the

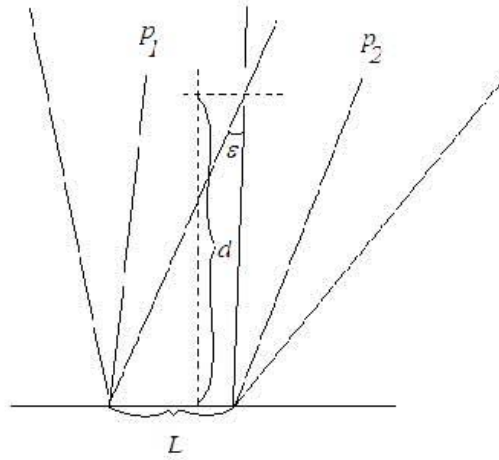


**Figure 10:** Two camera FOV overlap

base  $L$ , then Table 4 shows the largest possible distances  $d$  for a given FOV overlap  $\epsilon$ .

$\epsilon$	$p_1$	$p_2$	$d$	Total FOV
$1^\circ$	$-22^\circ$	$22^\circ$	114.6 ft	$89^\circ$
$2^\circ$	$-20^\circ$	$20^\circ$	57.3 ft	$88^\circ$

**Table 4:** FOV intersection distance for various levels of overlap, separation base  $L = 2$  feet,  $\text{FOV} = 45^\circ$

A minimum overlap of  $2^\circ$  (about 5% of each camera's FOV) is recommended to have a smooth transition of the tracks between the cameras.

## Appendix F Previous Measurement Extractors Considered

### Appendix F.1 Measurement Extractor 1

The measurements are extracted from each frame of data by first calculating the average pixel intensity over a sliding window and using it in a threshold to declare a detection in the center of the window. Each pixel of the frame can be divided by the appropriate average value of its neighborhood to find pixels which stand out from their neighborhood. The neighborhood average for pixel  $i$ ,  $\bar{I}_i$ , will be calculated as

$$\bar{I}_i = \frac{1}{L_1 L_2} \sum_{w \in W_i} I_w \quad (56)$$

where  $I_w$  is the intensity of pixel  $w$ ,  $L_1 L_2$  is the size of the window, and  $W_i$  is the set of pixels of the sliding window centered at pixel  $i$ . Pixel  $i$  will then be declared a detection if

$$\frac{I_i}{\bar{I}_i} > \tau \quad (57)$$

where  $I_i$  is the intensity of pixel  $i$  and  $\tau$  is the set threshold. This is Extractor 1a.

The detected pixels are grouped and the centroid of each group calculated as described in section 2.1.

This method of measurement extraction alone may result in a large number of false measurements if areas of the frame have especially low pixel intensities. Figure 11 shows the centroid measurements from the extractor which uses a threshold of 1.35 and  $L_1 = L_2 = 21$ . The large number of measurements at the top of the frame are a result of the low pixel intensities which can easily exceed the set threshold without being much larger than the neighborhood average intensity. In order to avoid this behavior, the detection rule can be augmented by requiring a detected pixel to also exceed the average pixel intensity of the entire frame. This is Extractor 1b. Figure 12 shows the centroid measurements from this updated measurement extractor.

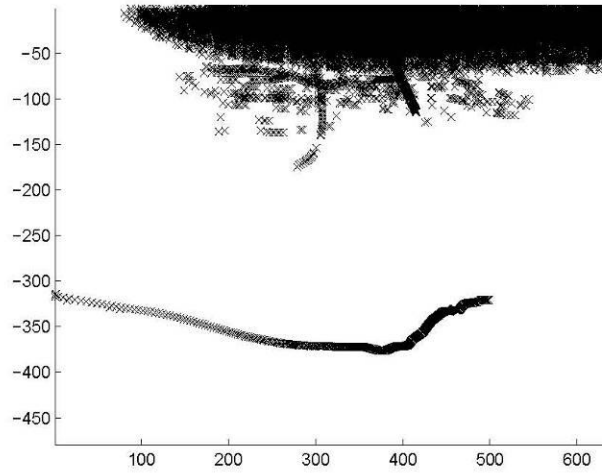


**Figure 11:** Extractor 1a with threshold of 1.35

## Appendix G Previous Motion Models Considered

### Appendix G.1 Wiener Process Acceleration Model

Originally, a discrete Wiener process acceleration (WPA) model [2] was used, where the state equation is

$$x(k+1) = Fx(k) + \Gamma v(k) \quad (58)$$

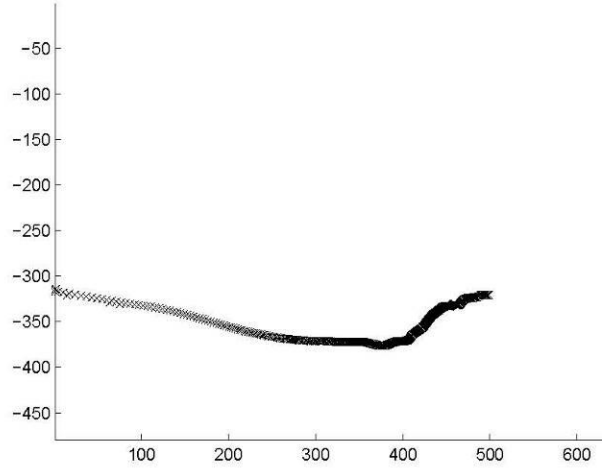


**Figure 12:** Extractor 1b with full frame average exceedance rule

where  $x(k)$  is the state at time  $k$  and  $v(k)$  is the process noise during the  $k$ th sample (acceleration increment in this case), and

$$F = \begin{bmatrix} 1 & T & T^2/2 & 0 & 0 & 0 \\ 0 & 1 & T & 0 & 0 & 0 \\ 0 & 0 & 1 & 0 & 0 & 0 \\ 0 & 0 & 0 & 1 & T & T^2/2 \\ 0 & 0 & 0 & 0 & 1 & T \\ 0 & 0 & 0 & 0 & 0 & 1 \end{bmatrix} \quad (59)$$

$$\Gamma = \begin{bmatrix} T^2/2 & 0 \\ T & 0 \\ 1 & 0 \\ 0 & T^2/2 \\ 0 & T \\ 0 & 1 \end{bmatrix} \quad (60)$$

where  $T$  is the sampling time ( $T = 1/30$  in our case).

The standard deviation of the measurement noise was assumed to be 0.5 pixels, while the standard deviation of the process noise (acceleration increment in a sampling interval) was chosen to be  $\sqrt{5}$  pixels/s<sup>2</sup>.

## Appendix H Previous Track Initialization Schemes Considered

### Appendix H.1 Track Initialization 1

A validation gate (in pixel space), based on the assumed maximum velocity of a target over one sampling period, was set up for each measurement location for the potential tracks. In this case, a gate which assumed a maximum velocity of 100 pixels in the  $x$ -direction and 50 pixels in the  $y$ -direction was used. Tracks were confirmed and initialized when a second consecutive measurement is found within the validation gate of the potential tracks. These tracks were then added to the list of currently running tracks and any potential tracks without a second measurement in their validation gates were dropped from the list of potential tracks.

## Appendix I Multiple Camera Registration

### Appendix I.1 Relative Registration

In order to track targets using multiple sensors, the sensors must be properly registered in order to combine the data. For this passive collision avoidance system, the cameras must be registered relative to each other at a minimum, i.e., it is only necessary to know the difference of the azimuth and elevation angles of each camera and not the actual azimuth and elevation angles. Absolute registration (section Appendix I.2) is only necessary for evaluating the performance of the tracker with a target of known location (e.g., one with GPS data).

In order to estimate the difference in azimuth angles of two overlapping cameras, the measurements of a target within the overlapping portion of the camera frames can be used. The relation between the azimuth measurements



of two cameras (e.g., camera A and camera B) is

$$\alpha_B + \hat{\alpha}_B = \alpha_A + \hat{\alpha}_A \quad (61)$$

where  $\alpha_x$  is the boresight azimuth of camera  $x$  and  $\hat{\alpha}_x$  is the measured azimuth to the target (relative to the focal plane of camera  $x$ , and available from (27) in Appendix A). Rearranging (61) results in the difference of the camera boresight azimuth angles ( $\tilde{\alpha}$ ):

$$\tilde{\alpha} = \hat{\alpha}_B - \hat{\alpha}_A \quad (62)$$

A similar equation holds for the elevation angle.

Additionally, a possible non-zero roll angle in either camera must be taken into account. The measured azimuth and elevation angles can be corrected by using the transformation  $T_3$  from Appendix B. This will correct the measured azimuth and elevation angles for the roll angle rotation of the camera (assumed known) so that the new azimuth and elevation angles are relative to a camera with zero roll angle.

The boresight angle difference (62) can be calculated for each measurement within the overlap of the two camera and this data can be used in a LS (least squares) estimator. The LS estimator in this case simply corresponds to the sample mean of the calculated boresight angle differences.

## Appendix I.2 Absolute Registration

Registering one camera in relation to another will provide the difference in azimuth and elevation angles of the boresight of each camera. Using this information, if the pointing direction of one camera is known, then the pointing angle of the second camera is simply the pointing angles of the first plus the differences obtained from relative registration.

In order to determine the pointing angle of the first camera, available GPS information for a tracked target can be used. The GPS data can be converted to ENU coordinates by using the calculations of Appendix C with the origin of the ENU coordinate system as the camera location. The ENU coordinates can then be used to determine the azimuth and elevation angles from the camera to the target. The measurements of the target in the focal plane (in pixels) can be translated to azimuth and elevation angles, relative to the focal plane, by using the equations of Appendix A. The boresight azimuth angle is then

$$\alpha_{BS} = \alpha_{GPS} - \alpha_{FP} \quad (63)$$

where  $\alpha_{BS}$  is the boresight azimuth,  $\alpha_{GPS}$  is the azimuth obtained from the ENU coordinates of the GPS data, and  $\alpha_{FP}$  is the azimuth of the measurement relative to the focal plane. A similar equation can be used to solve for the elevation angle. Multiple points of GPS data can then be used in a LS estimator to determine the estimated boresight angle of the camera.

If GPS data is available for a target in the second camera, the same equations can be used to determine the boresight angles of the second camera. The boresight angles of the second camera can also be calculated using the data from relative registration along with the boresight angles calculated for the first camera. These two sets of boresight angles can then be compared. Additionally, the GPS data for the target in the second camera can also be compared to the angles calculated from relative registration and the boresight angles of the first camera. Table 5 shows the boresight angle estimates of Camera A calculated both directly from GPS data and also indirectly from the relative registration of Camera A to Camera B (using the boresight of Camera B calculated from GPS data). Additionally, the azimuth and elevation angles to the target were calculated using the relative registration boresight angles, and the RMS errors were then calculated (using the azimuth and elevation to the target calculated from the GPS data as truth).

	Relative Registration	GPS	RMS error
Azimuth	38.5°	38.68°	0.808°
Elevation	19.76°	18.4°	1.578°

**Table 5:** Comparison of boresight calculations (for Camera A) resulting from relative registration to those resulting from direct GPS data estimation

## References

- [1] Y. Bar-Shalom and X. R. Li, **Multitarget-Multisensor Tracking: Principles and Techniques**, YBS Publishing, 1995.
- [2] Y. Bar-Shalom, X. R. Li and T. Kirubarajan, **Estimation with Applications to Tracking and Navigation: Theory, Algorithms and Software**, J. Wiley and Sons, 2001.
- [3] R. Osborne III, Y. Bar-Shalom and T. Kirubarajan, "Radar Measurement Noise Variance Estimation with Several Targets of Opportunity," *IEEE Trans. on Aerospace and Electronic Systems*, July 2008.

The following are representative frames of the process video created by UConn. The red track indicates that their measurement extractor has located the target aircraft and has started a track. In Figure 59, the angular velocity (degrees/second) of tracked targets is displayed. The GPS tracking information in on the left and on the calculated from the image is on the right.

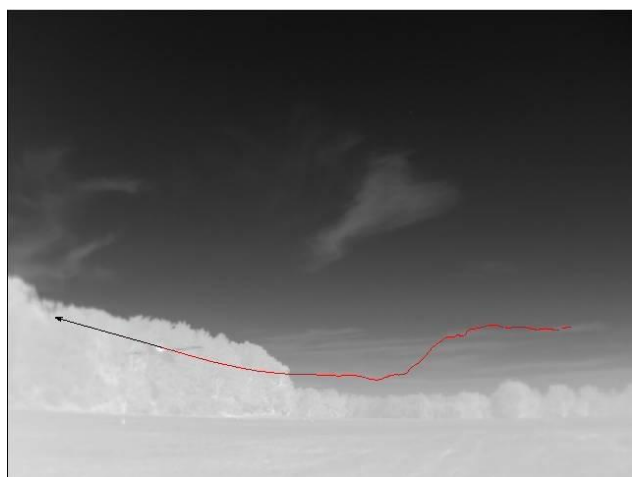


**Figure 57: Video track of Ultralight of Figure 6 of the UConn report showing no collision.**

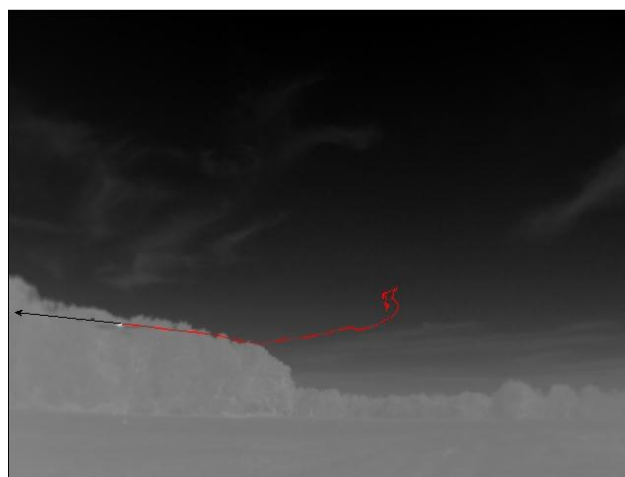


**Figure 58: Video track of Ultralight of Figure 7 of the UConn report showing collision course.**



**Figure 59: Video track of Piper aircraft using side by side L3 cameras at Pottstown Airport (Figure 28). Left hand side in the data logger GPS track, right hand side is the calculated track**

## 5.2 Image Differencing

While UConn focused on single frame detector, with the issue of clutter removal and S/N, using image differencing is another approach. By differencing, clutter would be “zeroed” out because it is static frame to frame and targets which are moving would create additional contrast against the static background. This concept is illustrated in Figure 60, the algorithmic flow is illustrated in Figure 62. The bird flying in from the right is not apparent in the image on the left. The background including the ground clutter goes to zero. However, image differencing is very susceptible to motion of the platform during collection. The image must be stabilized to be

effective (Figure 61). Note: at this time due to the ending of the program stabilization was not completed.

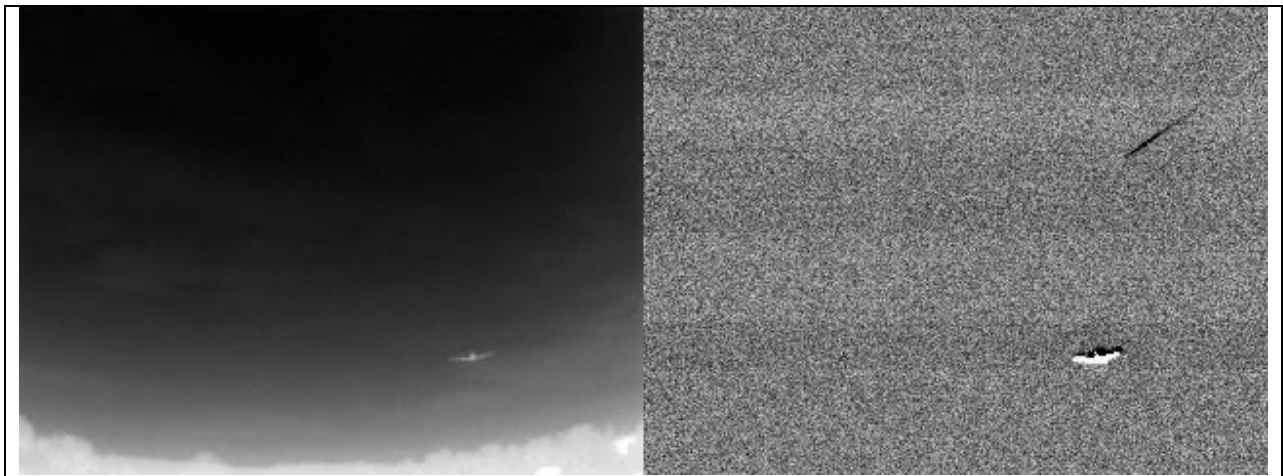


**Figure 60: Example of image differencing.**

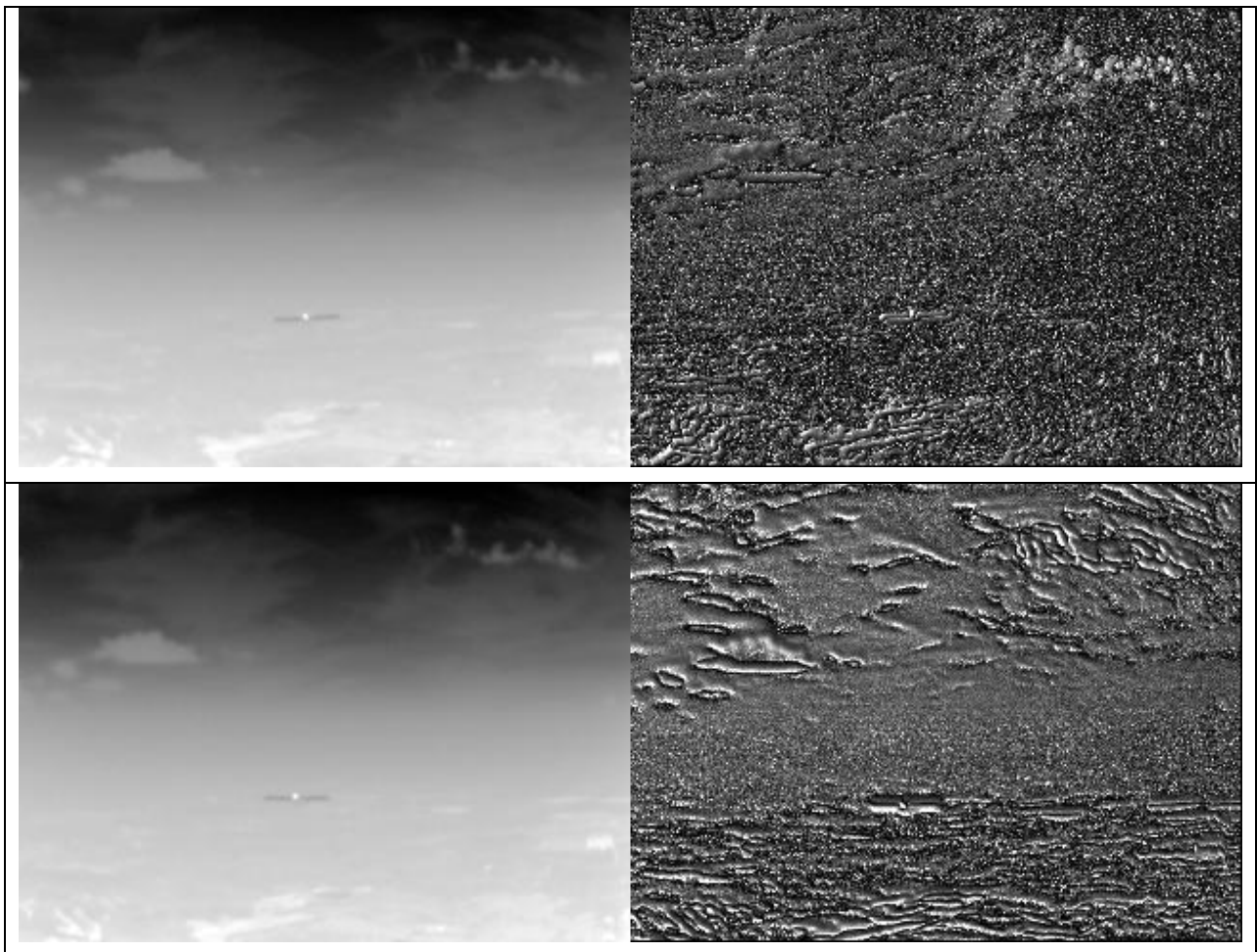


Figure 61: Example of image differencing on a moving unstablized platform.

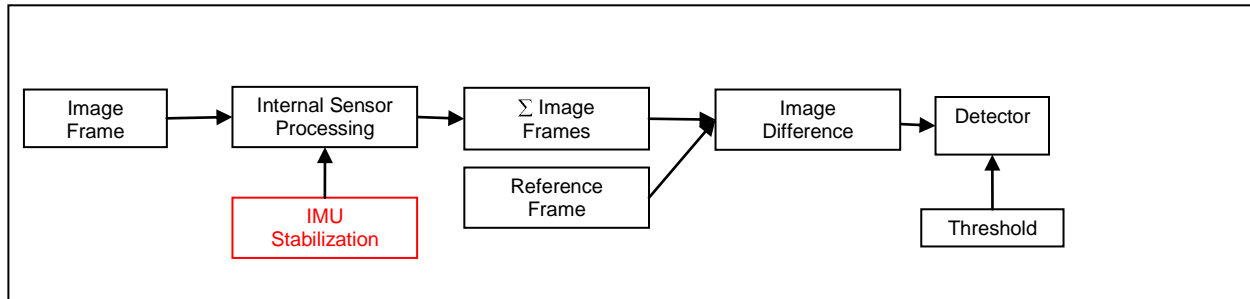


Figure 62: Flow diagram of the image through the sensor.

## 6 Hardware Approach for Tier I UAV

MilSys Technologies as been in contact with a few of the mini-UAV manufacturers to discuss our PCAS system. Our existing configuration of a multi-sensor system does not meet their SWAP requirements. What has come out of our discussions, is that the mission profile is different enough from the Predator class, that some compromises on performance can be made to reduce the SWAP requirements.

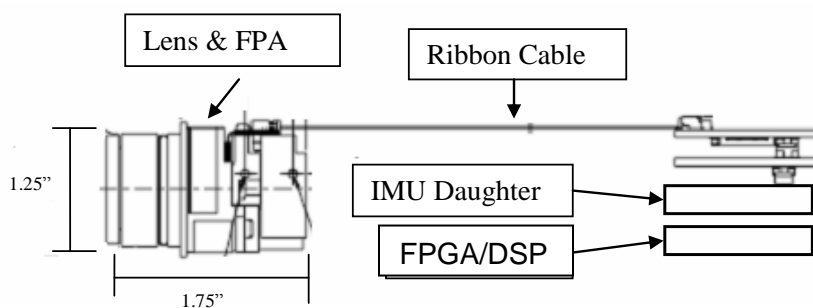


Figure 63: Side on diagram of the propose sensor / TP. Note the dimensional scales.


	Weight
3600AS	3oz w/lens
FPGA/DSP	2oz
IMU	2oz
Total	7oz

**Table 8: Estimated weight.**

As discussed in Section 1.3, the most import factor in avoiding collisions is the time to collision. For the Predator class under most situations, it has been specified as 32 seconds [minimum]. Due to the differing mission scenarios and platform design for the mini-UAS, this time can be

reduced to  $\approx 10$  seconds. MITL time goes to 0 and the bank angle can be significantly  $>18^\circ$  reducing the time to  $\approx 5$  seconds. Detection and tracking time remains constant at 2-5 seconds. At a 250knot head on closing speed, 10 seconds is 1.5km minimum slant range at detection. Microbolometer technology is more than adequate for this mission.

The innovative approach is integrate COTS IR technology, such as the L-3 Thermal Eye 3600AS (Table 9), Xilinx FPGA/DSP with an IMU currently under development at MilSys Technologies. Figure 63 is a side on view of what the hardware would approximately look like. The lens and FPA are separate from the control electronics for the maximum mounting flexibility (Figure 63). Table 8 is the estimate of the total weight  $\approx 7\text{oz}$  ( $<0.5\text{lbs}$ ). The Scan Eagle published payload is 6lbs the Silver Fox is 5lbs. So the proposed configuration is at  $\approx 10\%$ . With additional engineering one or two of the PCBAs could potentially be eliminated. The major weight driver is the lens.

	
Optics	$<\phi 0.5''$
FOV	$50^\circ$
Pixels	160 X 120
Pixel Size	$30\mu\text{m}$
Technology	a-Silicon
Wavelength	$7\text{-}14\mu\text{m}$
Sensitivity	$<50\text{mK}$
Table 9: L-3 3600AS.	

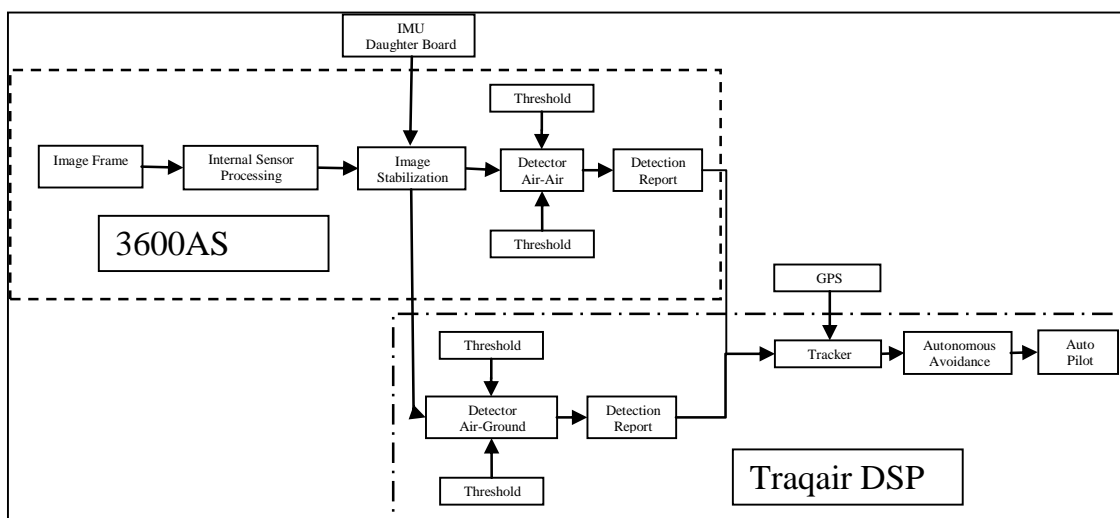


**Figure 64: Block diagram of how the new functions of air-ground would be implemented to leverage the existing PCAS architecture and developments.**

With only one sensor, complex image transformation will not be required by the TP, however, the new function of air-ground will replace it. The block diagram of the information is more complex with the addition of the air-ground detector (Figure 64).

The lens currently offered by L-3 on the 3600AS has a FOV of  $53^\circ \times 37^\circ$ . Ideally for a forward looking only EO/IR SAA system, a horizontal FOV of  $90^\circ\text{-}120^\circ$  would be optimal. However, microbolometers need a low F/# lens, this drives weight up. An innovative aspect of this proposal is a contrarian approach to lens design. Most lenses are designed for imaging. A trade study will be performed looking at several alternative approaches: For example, modified off the shelf single element (Figure 65) similar to the Temmek Optics IRViper. Note that the weight is almost 4X that of the proposed camera. LWIR transmitting plastics are available (Figure 68). Designs will be reviewed that would be a combination of aspheres, fresnel lenses (Figure 67), and/or diffractive lenses molded out of plastic or chalcogenide glass. A final design possibility is a complex anamorphic wide angle view converter (Figure 66). The optical system



will have a predetermined optical power in the horizontal axis different from the vertical axis. Typically, a pair of prisms is used to form an anamorphic system. For this system, the prism



**Figure 65: Temmek Optics – IRViper Lens, F/# 0.8, FOV  $\approx 80^\circ \times 60^\circ$ , Weight – 260g.**<sup>xxxiii</sup>

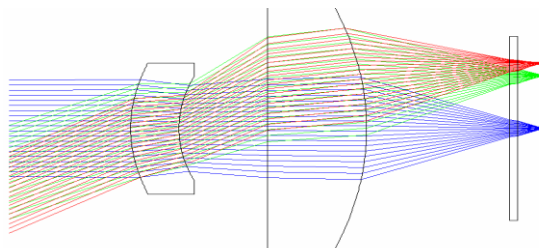


**Figure 66: Schematic of a wide angle FOV converter.**

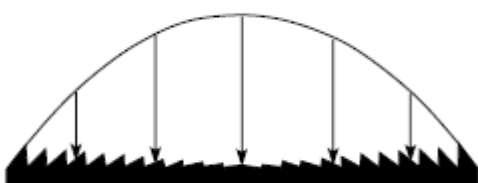


**Figure 67: Schematic of a Fresnel lens.**<sup>xxxiv</sup>

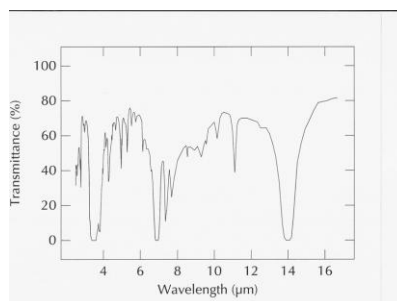


**Figure 68: Transmission spectrum of Fresnel Technologies POLY IR® 2 IR plastic.**<sup>xxxiv</sup>

pair will be incorporated into a two or three element toroidal lens system to change the field of view from a 4x3 format for the microbolometer sensor to a different field of view format. That is, to use all of the pixels most efficiently for a 4x3 image format the corresponding field of view would be 40deg. x 30 deg. As an example, to change to a field of view to 60 deg. or 120 x 30 deg., the toroidal lenses would need to compress the horizontal axis by a factor of 1.5 for the same sensor. The resultant image will have an image which is 2.25 to 4.5X times brighter in the vertical FOV than the horizontal FOV. The overall tradeoffs for the entire system will be the lowest f/number that can be achieved while holding the distortion and the allowable vignetting at the edges of the field to a minimum, while optimizing the lens system for weight, cost and volume.

## 7 Extension of the Technological Approach to solve the full CA problem

### 7.1 Introduction

As defined by the JIPT<sup>xxxv</sup> in their recently published draft UAS requirements document, a sense and avoid (SAA) system encompass the following functions: air-to-air, air-to-ground, ground-to-ground, ground-to-air, and man made hazards (Table 10). Part of the mission planning is an environmental forecast encompassing both atmospheric phenomena and manmade hazards (i.e. smoke). However, this forecast is for the macro airspace and may not necessarily be accurate for the localized mission airspace. As long as the UAV remains within the line of sight of the warfighter, it has a SAA system. As soon as the UAVs fly out of the line of sight on the battle field, risks to the mission increase. Adding the capability to sense the environment would enhance the utility of UAVs, by allowing more autonomous operation, provide localized forecasting for battlefield management, and provide real-time feedback to the onboard ISR sensor suit to maintain probability of detection, contrast level, etc. This capability would reduce

the workload of the warfighter, increase mission success rate, and expand mission opportunities.

To address these needs, various sensors concepts based on the microbolometer were developed. The ability to differentially sense temperature, passive ranging, IR spectrum of clouds and polarization were reviewed for their applicability to potentially solve these issues as well as the technological feasibility.

Phase of Flight	Req. # & Label	Draft Operational Requirement	Rationale / Amplification	Draft Threshold
1.4 UAS Operations - Collision Avoidance				
All Phases	1.4	The UAS shall be capable of avoiding hazards.	Overarching Hazard Avoidance requirement.	
All Phases	1.4.1	The UAS shall be capable of avoiding collision hazards.		The UAS initiates an avoidance maneuver base collision avoidance system determination of a potential hazard.
All Ground	1.4.1.1	While on the ground, the UAS shall be capable of avoiding airborne hazards (Ground-to-Air).	The requirement is to avoid becoming a runway incursion, as in clearing final before taking the active runway.	
All Ground	1.4.1.2	While on the ground, the UAS shall be capable of avoiding ground hazards (Ground-to-Ground).	During taxi operations in the airfield environment, the UAS must be able to avoid fixed obstacles, other ground aircraft, as well as ground support equipment. During takeoff, the UAS shall be	Fixed obstacles 2015

Table 10: JIPT SAA requirements.

## 7.2 Cloud Detection via Infrared Imaging (Background)

Clouds can be detected on an airborne platform with LWIR infrared imaging owing to the high radiometric contrast between the clear-sky emission and the cloud emission<sup>xxxvi</sup>. The Optical Remote Sensors Laboratory (ORSL) at Montana State University, under the direction of Dr. Joseph Shaw, has developed instruments and algorithms for detecting clouds, measuring cloud statistics, and characterizing cloud type using ground-based, uncooled microbolometer thermal infrared cameras<sup>xxxvi,xxxvii,xxxviii</sup>. These techniques were optimized for vertically viewing ground-based infrared imagers, could be modified to operate in an airborne environment for detecting clouds at angles other than vertical.

**Figure 69** shows the down-welling atmospheric spectral radiance calculated for the 1976 U.S. Standard Atmosphere, plotted versus wavelength for a wavelength range of 5-18  $\mu\text{m}$ . This figure illustrates the atmospheric emission spectrum that would be seen by a ground-based, upward-viewing infrared sensor. The bottom three curves are for a clear sky with water vapor contents that increase upward from the bottom curve: 0.1x, 1x, and 2x the normal water vapor content. The top curve is for a cloudy sky with mid-level altostratus clouds. **Figure 70** is the vertical-path atmospheric transmittance plotted versus wavelength for the 1976 U.S. Standard Atmosphere model, with 1x water vapor (top) and 2x water vapor (bottom). These figures show that the atmosphere exhibits high transmittance where there is low emission, and vice versa. This is the result of emission arising proportional to absorption.

Examining **Figure 69** and **Figure 70** within the spectral bandwidth of most LWIR cameras (~8–14  $\mu\text{m}$ ) reveals several important points about cloud detection with IR cameras: 1) the

atmosphere has relatively high transmittance, especially with low water vapor content); 2) Many clouds are quite bright relative to the clear-sky radiance; and 3) variations in atmospheric water vapor can be interpreted as thin clouds unless the intervening atmospheric emission is compensated for carefully. The difficulty of distinguishing between thin cirrus clouds and water vapor variations is further illustrated by **Figure 71**, which plots down-welling atmospheric emission versus wavelength (similar to **Figure 69**) for a clear sky, a very thin cirrus cloud, an altostratus cloud, and a cumulus cloud. Comparing **Figure 69** and **Figure 71** shows that in this case the thin cirrus emission is less than the radiance change that would occur with a doubling of water vapor.

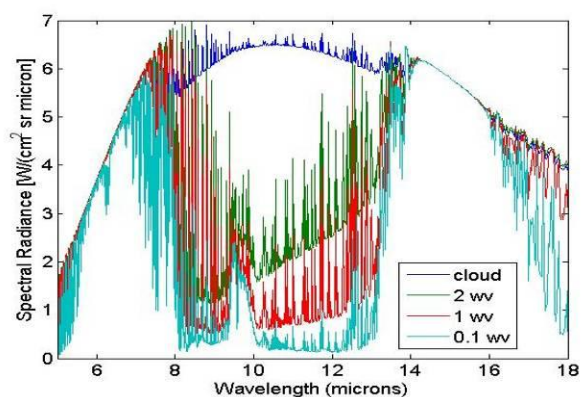


Figure 69: Down-welling atmospheric emission spectrum for the Atmosphere model, shown for a clear sky with three different values of water vapor content (0.1×, 1×, and 2× the standard value) and for altostratus clouds (top blue)

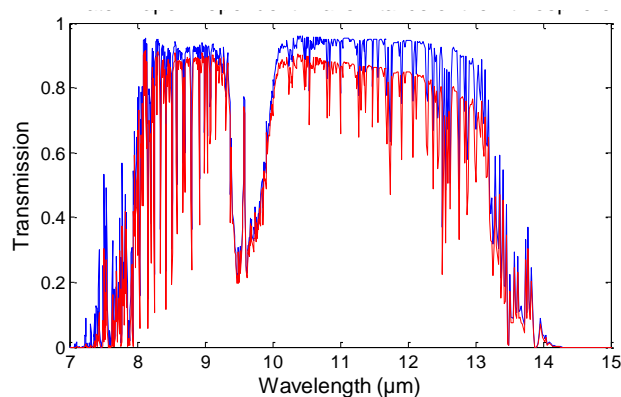


Figure 70: Atmospheric transmittance for a zenith path through the Standard Atmosphere. The top (blue) curve 1× water vapor, and the bottom curve (red) is for 2×.

In ground-based cloud measurements for climate studies it is critical to detect even very thin cirrus. Therefore, these situations are handled through the use of IR cameras that are calibrated very carefully to achieve radiometric measurements with high accuracy and stability<sup>xxxvi, xxxviii</sup>. In these situations the clear-sky emission is calculated using ancillary data that provides a measure of the precipitable water vapor and near-surface air temperature, and this emission is subtracted from the image to generate a “residual radiance” image. These residual radiance images are ideally zero everywhere except where clouds exist. The magnitude of the residual radiance is used to determine cloud type. An example of this type of data is shown in **Figure 72**. In this figure the left-hand panel is the calibrated radiance sky image, the center panel is the residual radiance image, and the right-hand panel is the cloud-detection image color coded by cloud type (dark blue for clear, red for the radiometrically brightest clouds, and other colors for intermediate cases).

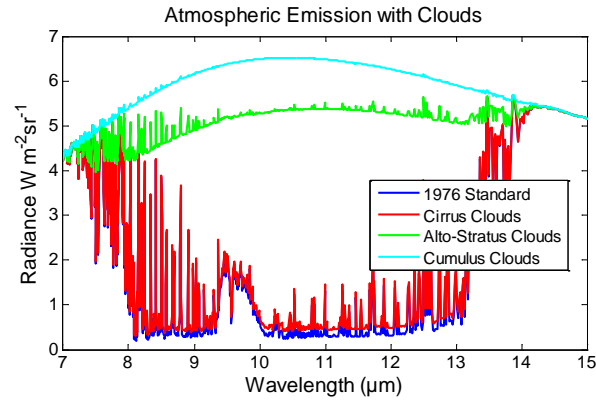


Figure 71. Down-welling emission spectrum for clear sky (blue curve, bottom), very thin cirrus at 9 km altitude (red curve, 2<sup>nd</sup> from bottom), alto-stratus cloud at 2.4 km (green curve, 3<sup>rd</sup> from bottom), and cumulus cloud with its base near 100 m (teal curve, top).

In the proposed technology, the emission signatures will change significantly from what is shown in the preceding figures, primarily because of the large range of viewing angles to be encountered. Also, we are not likely to have sufficient information available to properly estimate the emission of the intervening atmosphere (which requires a reasonable estimate of the atmospheric temperature and water vapor profiles, viewing angle, and range to the cloud). Furthermore, because of size and weight constraints, the imager likely will not be deployed with onboard calibration sources, making the direct use of previously developed algorithms insufficient for this application. Nevertheless, the principles are the same and the need to accurately characterize thin clouds is not a necessary component. Consequently, we propose to develop algorithms that operate on a more relative basis, identifying clouds through the use of a radiometric calibration that is measured in the laboratory and applied to the imager in flight. Shaw's group at Montana State University has recently patented algorithms that allow very accurate calibration of infrared imagers without onboard blackbody sources, and similar techniques will be used here.

The algorithms to be developed would will rely less on the absolute radiance (which is a necessary component of the cloud imaging work done at Montana State University for climate studies) and instead rely more on the relative variations of brightness seen while the air vehicle is flying. Measurements of vehicle altitude and attitude will be used to determine the nominal pointing angle of each pixel, and algorithms will be developed that use either look-up table or

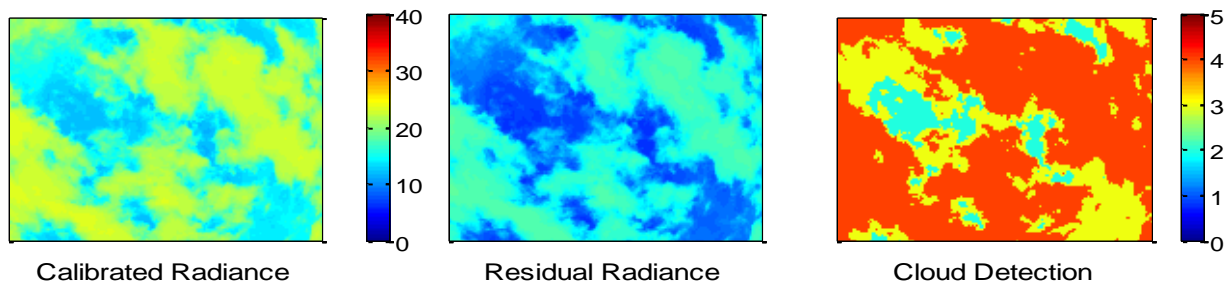


Figure 72. Images from the wide-angle Infrared Cloud Imager system developed at Montana State University: (left) radiance, (center) residual radiance after removing atmospheric emission, and (right) detected clouds classified by cloud type (from 0 = no clouds to 5 = thick clouds as described in text).

curve-fit routines for estimating the background atmospheric signature as a function of viewing angle. This type of approach is not likely to offer sufficient stability and accuracy to allow reliable detection of thin cirrus, but in this application the much more important clouds to detect are thicker clouds that indicate the presence of stormy weather or total obstruction of the view in a particular direction. As shown in **Figure 69**, these clouds are very easy to detect because of their large radiometric brightness relative to the clear atmosphere.

Additional information may be available from the spectral distribution of radiance within the camera's full bandwidth as is being developed. As is indicated in **Figure 69**, there is a distinctly different slope of radiance versus wavelength for clear-sky emission and cloud emission. Satellite imager algorithms sometimes rely on this fact to detect clouds through a "split-window" technique or similar approach relying often on ratios of the radiance detected at two different wavelengths<sup>xxxix</sup>.

### 7.3 LWIR Multispectral Sensor

The literature in the atmospheric science journals is limited. Clouds can be detected on an airborne platform with LWIR infrared imaging owing to the high radiometric contrast between the clear-sky emission and the cloud emission<sup>xxxvi</sup>. The Optical Remote Sensors Laboratory (ORSL) at Montana State University, under the direction of Dr. Joseph Shaw, has developed instruments and algorithms for detecting meteorological phenomena (i.e. clouds, measuring cloud statistics, and characterizing cloud type) using ground-based, uncooled hyperspectral microbolometer based systems<sup>xi,xli,xlii</sup>. Another recent paper by Tamachi<sup>xliii</sup> et al. evaluated the potential of a ground-based IR camera (FLIR Systems, Inc.) to map cloud base temperatures around supercell storms. This study included a nice summary of the difficulties in acquiring accurate measurements from the ground because of IR sources from water vapor, aerosols, and dust within the atmospheric boundary layer. For a UAV flying above the turbid boundary layer, improved IR measurements could be obtained, free from the artifacts described for ground-based imagers as described by Tamachi et al.

What has been investigated, is the possibility of combining a SAA system that is capable of providing both an environmental sensing and air-air collision avoidance capability. At the heart of the MilSys Technologies PCAS are microbolometers which are low cost SWAP efficient LWIR sensors. As can be seen in **Figure 73-Figure 77**, both clouds and an aircraft are visible in the images.



Figure 73: LWIR image of clouds using  $\mu$ bolometer. Red circle is an aircraft.



Figure 74: Image before rain.



Figure 75: Image during rain.



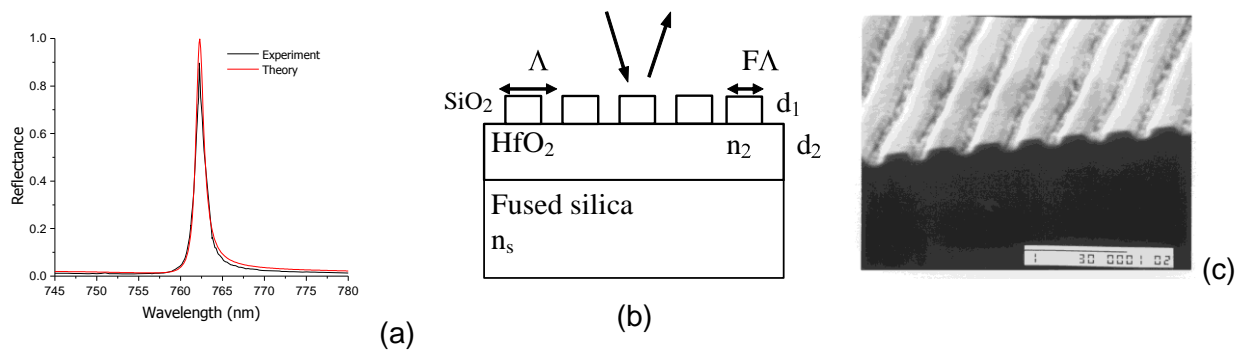
Figure 76: Cloud formations.



Figure 77: Same day as Figure 76

Microbolometers are monochromatic detectors so that the radiant extent of an object is reduced to intensity. Therefore, a hot and distant object could have the same intensity as a close and cool object. The larger the radiance differential is between meteorological phenomena and the background, the greater the probability that this phenomenon is a hazard and should be avoided. Dr. Shaw has developed algorithms that can be used to detect, track, and threshold





**Figure 81.** An example of a fabricated guided-mode resonance element with comparison between experiment and theory for a double-layer device (a). The parameters used for the theoretical curve fit are close to the nominal values; they are cover refractive index  $n_c=1.0$ ,  $n_1=1.454$  (SiO<sub>2</sub>),  $n_2=1.975$  (HfO<sub>2</sub>), substrate index  $n_s=1.454$ ,  $d_1=135$  nm, fill factor (fraction of period occupied by the higher-index medium)  $F=0.58$ ,  $d_2=208$  nm, period  $F\Lambda=446$  nm, and angle of incidence  $\theta=0^\circ$  (b). A scanning electron micrograph (SEM) and a schematic of the device are shown (c) <sup>xlviii</sup>.

meteorological phenomena. Other researchers have developed algorithms to autonomously avoid and plan a path around them <sup>xliv</sup>. However, the lack of discrimination and ranging for intensity only sensing, makes path planning and avoidance more difficult. Even with these limitations, this system concept will work and can be integrated with the current development of our PCAS.

The innovative technology is to create a multispectral microbolometer. This will allow the discrimination of meteorological phenomena by allowing its radiant extent to be measured. These measurements will be used in three ways (3): as raw wavelength data, converted to differential temperature and/or range. The result will be to reduce false positives, improve path planning and avoidance, and the detection and identification of meteorological phenomena etc. This will be accomplished by developing and integrating three (3) technologies; guided mode resonate (GMR) filters, microbolometers, and a moving FPA.

Guided-mode resonance (GMR) filters consist of fine spatial patterns arranged to control the propagation of light (Figure 81). Lithographic patterning of dielectric surfaces, layers, or volume regions yields low-loss structures that affect the spatial distribution, spectral content, energy content, polarization state, and propagation direction of an optical wave. GMR filters can exhibit a filter function that exceeds the performance found with 50 to 100 layer thin-film filters. A significant body of published work has focused on narrow-line GMR filters which have been demonstrated both theoretically and experimentally <sup>xlv-xlviii</sup>. These filters require tight fabrication tolerances. The key insight of the proposed technology is to use GMR filters in a contrarian

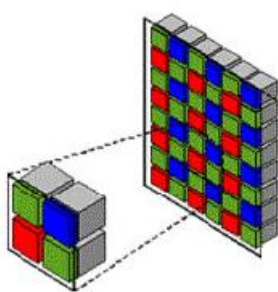


**Figure 78:** Representation of different filters.

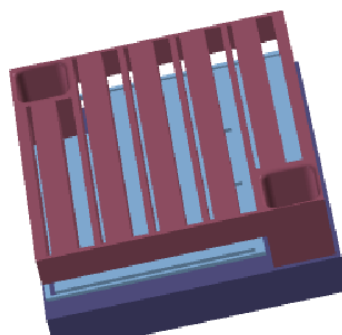


**Figure 79:** Schematic of a GMR membrane (purple) above a pixel (light blue).

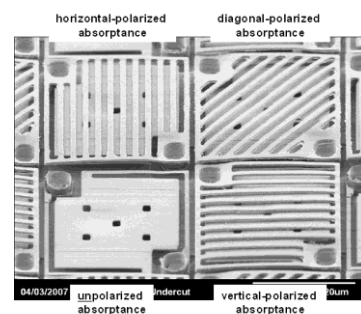


**Figure 80:** SEM of a wire grid polarizer produced by L-3.

approach. That is as a broadband filter (1-3 $\mu$ m bandwidth) with loose fabrication tolerances. By slightly changing the structure without changing the material thickness, the spectral selectivity properties can be modified. A multispectral sensor can then be constructed out of several different GMR designs with a minimum of fabrication steps (Figure 78).

The temperature range most commonly encountered by the multispectral microbolometer will be 0-50°C which has a peak blackbody emission in the 8-12 $\mu$ m range (LWIR) and which corresponds with the peak sensitivity of a microbolometer. By designing GMR filters that are spaced across the LWIR (e.g. 8-9 $\mu$ m, 9-10 $\mu$ m, 10-11 $\mu$ m, 11-12 $\mu$ m etc.) the radiant extent of meteorological phenomena can be measured. By integrating the GMRs into the pixels of the microbolometer each pixel is now wavelength sensitive and permanently co-registered (Figure 78). This is analogous to the Bayer pattern used in visible CCD and CMOS cameras.

Microbolometers are thermal devices and their sensitivity and responsivity are directly related to their thermal mass. The construction of the GMRs on the surface of the microbolometer would drastically change their thermal mass requiring a substantial redesign of the entire microbolometer. Independently and concurrently, MilSys Technologies, Dr. Magnusson and L-3 were working on the concept of building membranes above the surface of materials for the purpose of creating highly integrated optical structures. L-3 has developed the design, process, and integration technology and lithography to construct Aluminum membranes above their pixels (Figure 79 & Figure 80). These membranes are currently 0.25 $\mu$ m thick wire grid polarizers  $\approx$ 1 $\mu$ m above the surface. This technology will need to be extended to the design parameters of the GMR filters. Current estimates are that the material will be Silicon  $\approx$ 1 $\mu$ m thick  $\approx$ 3 $\mu$ m above the surface.

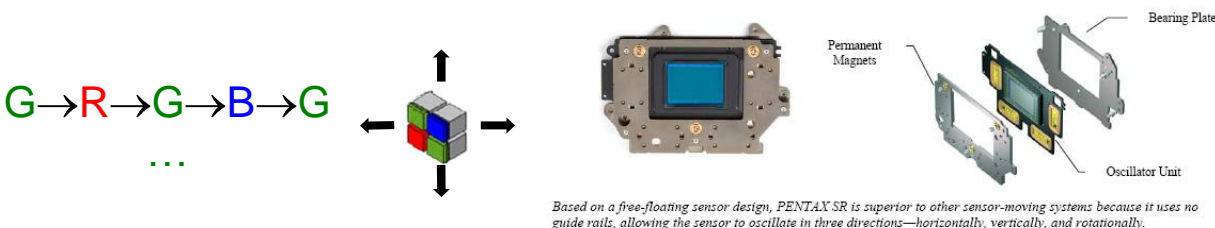


**Figure 82: Example of the movement of a FPA to produce “multispectral image of an IFOV of the FOV. Each arrow (→) represent the physical movement of the FPA in time.**

**Figure 83: Pentax**

Many consumer based camera companies have developed technologies to remove hand and vehicle vibrations during an image capture. They go by the trade names Anti-Shake™, Vibration Reduction™ etc., and have been in wide scale production for approximately 5yrs. Camera motion is detected via MEMs based gyroscopes and compensated for by mechanically moving either the lens<sup>xlix</sup> or the sensor<sup>l,li</sup> (Figure 83) These types of inertial sensors, mechanical mechanisms, and feedback controllers are routinely incorporated into D-SLR cameras costing <\$400. The mechanical moving mechanism is usually a piezo-electric or magnetic coil similar to the driving mechanisms in hard disk drives or zoom lenses on cell phones (Squiggle™)<sup>lii</sup>.

A moving FPA would use this technology in reverse. Instead of removing vibrations, the FPA would be translated around the image plane (Figure 82). This motion would create a multispectral image where each instantaneous field of view (IFOV) would be sampled with several different GMR filters at the frame rate of the camera. The speed of these driving mechanisms is better than 5mm/s (i.e. 5ms to move 25 $\mu$ m and accurate (<1 $\mu$ m).



## 7.4 LWIR Temperature Sensor and Passive Ranging

At a basic level, all radiometric temperature sensors are single point measurements. This is adequate when atmospheric absorption can be negated. However at a significant range, such as for this program, this methodology is inadequate. To use radiometry for temperature measurement, multiple data points (i.e. two(2) or more data points at differing wavelength bands) are required. Significant work has been completed, in multiband systems in the MWIR and LWIR<sup>liii</sup>. However, the prior development work has been focused on missiles and other objects which have significantly higher radiance in the MWIR than meteorological phenomena (clouds and aerosols) and these systems are both SWAP and cost prohibitive for UAV use.

$$R_{\text{detect}} = \sqrt{\frac{L_{\text{object}} T - L_{\text{background}}}{NEI} | e^{-\alpha R_{\text{detect}}} }$$

$\alpha$  = absorption of atmosphere

$NEI$  = sensitivity of sensor

$L$  = radiance  $W \text{ sr}/m^2$

**Equation 1: Range Equation<sup>liv</sup>**

$$L_{\lambda_1, \lambda_2, T} = \int_{\lambda_1}^{\lambda_2} \frac{c_1}{\lambda^5 \left( e^{\frac{hc}{k_b \lambda T}} - 1 \right)} d\lambda$$

**Equation 2: Radiance form of the Blackbody Equation.**

$$\frac{L_{8-10\mu m}}{L_{10-12\mu m}} = k T$$

**Equation 3: The ratio between two(2) radiances of a blackbody is a constant which varies as a function of temperature ( $T$ ).**

Radiometrically, the range to an object, in the IR, can be determined if three(3) variables are known; absorption of the atmosphere, background temperature, and object temperature (**Equation 1**). In general, only the local background temperature is known to any precision, the atmosphere can be estimated using a priori information, and the object temperature is unknown. To use radiometry to determine the object's temperature ( $T$ ), a minimum of two(2) radiances ( $L$ ) at differing wavelength bands are required (Figure 84 & **Equation 3**). These data points are collected empirically by the spectrally sensitive sensor. By calibrating it, a lookup table can be completed to relate the ratio of the radiances to the temperature ( $T$ ) via Plank's Blackbody equation.

To accomplish this task, the multispectral microbolometer would be constructed with side-by-side GMR filters in the 8-10 $\mu m$  and 10-12 $\mu m$  (**Equation 4**). The FPA would be floated and translated back and forth as discussed, collecting the multiband radiometric data for each IFOV (Figure 18). Object temperature ( $L_{\text{object}}$ ) would then be derived

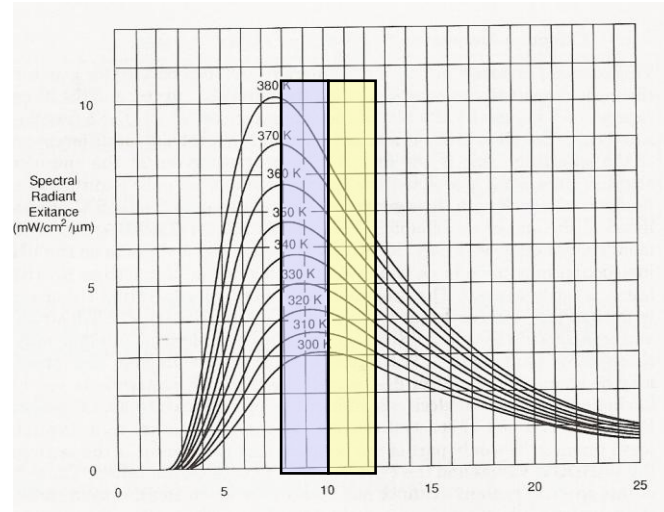


Figure 84: Blackbody curve for 25-100°C (300-380K). The blue box is the 8-10 $\mu m$  waveband, yellow is 10-12 $\mu m$ . The ratio between the total integrated radiance in each waveband indicates the temperature (Equation 3).



Figure 85: Data collected of an aircraft with a COTS microbolometer.

from this data (**Figure 84 & Equation 3**). Additionally, if the object is an aircraft and it is being tracked, the area around the aircraft could be mapped and knowing the background temperature and maximum range of the sensor, the absorption of the atmosphere can be approximated (**Equation 1**). This approximation will be more timely and accurate since it would be based on current data instead of the a priori data provided as part of the mission plan.

## 7.5 Autonomous Avoidance

Given a set of target tracks, the autonomous avoidance algorithms are responsible for separation assurance and collision avoidance. The avoidance algorithm depends in part on available measurements: if range to the target is available (e.g. through IR passive ranging, radar, ADS-B or TCAS) then it may be possible to employ more complex algorithms which seek to minimize deviation from the nominal track while maintaining separation. In this case trajectory optimization methods such as receding horizon control (RHC) can be applied. RHC has been used in various UAV planning scenarios, and recent work by Frew et al.<sup>lv</sup> was concerned with adaptively varying the planning horizon based on the dynamics of the environment.

If range is not available then the avoidance algorithm must control the aircraft to maintain non-zero bearing rate to targets (as discussed above). One approach is based on potential field methods for collision avoidance. This method was introduced by Khatib<sup>lvi</sup> and has been used in simulation and on hardware for obstacle avoidance using vision and inertial measurements as the sole sensors<sup>lvii,lviii</sup>. While potential field approaches can become trapped in local minima, this is generally restricted to cases where there are many obstacles or narrow passageways: this is unlikely to occur in the 3D environment of air vehicles. A closely related approach based on stream functions has been shown to produce smoother trajectories, and this may be more suitable for the current application. Potential field and stream function approaches have the advantage of computational simplicity, and thus will work in real time.

### 7.5.1 Autonomous avoidance Algorithms

Eventhough the BAA was focused on man in the loop CA system some time was invested in reviewing the development of autonomous concepts and algorithms and reaching out to the community on potential collaborations. Most UAS manufacturers and their customers are interested in a man-in-the-loop system for controlled airspace, but once the UAS is en route or on station in uncontrolled airspace where the expectation that >99.99% of the time the airspace is empty autonomous avoidance algorithms could control or take on an enhanced burden for de-confliction. Under these conditions CA is similar to trajectory optimization. Dr. Jack Langelaan @Penn State reviewed the literature and wrote a short proposal on the art of the possible.

Trajectory optimization for UAVs is an active area of research. Typical applications include minimal altitude trajectories for nap of the earth flight<sup>lix</sup>, flight in urban environments<sup>lx, lxi</sup>, ground vehicle tracking<sup>lxii</sup>, road following<sup>lxiii</sup>, target tracking and state estimation<sup>lxiv</sup>, search<sup>lxv</sup>, and more recently chemical plume tracking<sup>lxvi</sup>.

Collision avoidance trajectories are only required if nominal trajectories have failed (i.e. there is a loss of separation due to unforeseen events or unmodeled terrain). Hence very rapid response is required to place the aircraft in a safe state and the

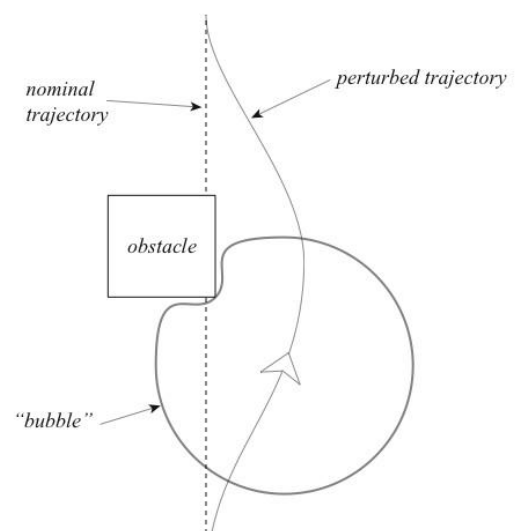


**Figure 86: Schematic representation of the "safety" bubble.**

response *must* be computed in real time. At the same time the computational capability on board a mini UAV is likely to be quite limited, hence very simple algorithms are required.

One of the simplest algorithms for obstacle avoidance is the potential field approach, introduced by Khatib<sup>lxvii</sup>. A potential field is computed based on obstacle position and size, and the vehicle is commanded to steer in the direction of the local gradient. This approach has been used for simulations of UAV navigation in obstacle strewn environments with vision and inertial measurements as the sole sensors<sup>lviii</sup>. Potential field approaches are computationally very simple to implement, but can become trapped in local minima under some conditions. However, the likelihood of these conditions occurring in a 3D environment is unlikely. In addition to obstacles, other constraints (such as altitude limitations or no-fly zones) can also be incorporated into the potential field. The aircraft's goal position (or desired track) can be represented as a "sink" in the potential field.

Figure 86 shows a modification which represents the potential field as a "safety bubble" around the vehicle. Any obstacle which enters the safety bubble causes a perturbation in the trajectory proportional to the size of the obstacle and the degree of bubble penetration. The size and "springiness" of the safety bubble depends on vehicle performance parameters (e.g. maximum turn rate) and mission parameters, and these will be determined as part of this work.

## 8 Conclusion

MilSys has demonstrated the feasibility of using SWAP efficient LWIR microbolometers as outlined in the Priest report circa 1998 as a solution to the collision avoidance problems for UASs . It has accomplished this by, modeling the response, collecting data and leveraging and developing detection and tracking algorithms that could be implemented into future systems. Design proposals were completed that showed the feasibility of extending the concept up to larger aircraft and down the smaller Tier I type UASs. To solve the entire collision avoidance problem, as discussed by the JIPT, technology was proposed, that would create an integrated color FPA that could determine range, weather, and still perform the collision avoidance function.

## 9 References

- <sup>i</sup> Joint Integrated Product Team briefing 21-23 Aug 2007.
- <sup>ii</sup> Doug Davies at AVUSI 2008.
- <sup>iii</sup> Discussion at SC-203 WG3 on Feb 6, 2007. Author does not have direct references.
- <sup>iv</sup> Krause, Shari Stamford, "Avoiding Mid-Air Collisions", McGraw-Hill, 1995.
- <sup>v</sup> "Feasibility of a Passive Collision Avoidance System (PCAS) Based on Staring Infrared Sensors", January 1998, E.H. Takken, E.J. Stone, R.G. Priest, J.C. Kershenstein, NRL, Washington, DC 20375.
- <sup>vi</sup> J.M. Lloyd, "State-of-the-Art for Thermal Imaging", Opt. Eng. Vol. 14(1), Jan 1975.
- <sup>vii</sup> J. Ratches, "Night Vision Laboratory Static Performance Model for Thermal Viewing Systems," RD Tech. Report ECOM-7043, 1975.
- <sup>viii</sup> J. Howe, "Electro-Optical Imaging System Performance Prediction," IR & EO systems handbook, Vol. 4, 1993.
- <sup>ix</sup> NVTherm 2002 manual, Night Vision Laboratory, Fort Belvoir, VA.
- <sup>x</sup> NVTherm IP manual, Night Vision Laboratory, Fort Belvoir, VA.
- <sup>xi</sup> F. Niklaus, "Uncooled Infrared Bolometer Arrays Operating in a Low to Medium Vacuum Atmosphere: Performance Model and Tradeoffs", Infrared Technology and Applications XXXIII, Proc. of SPIE 2007.
- <sup>xii</sup> S. Horn, D. Lohrmann, P. Norton, K. McCormack, A. Hutchinson, "Reaching for the Sensitivity Limits of Uncooled and Minimally-Cooled Thermal and Photon Infrared Detectors", SPIE Vol. 5783, Apr 2005.
- <sup>xiii</sup> R.A. Wood, "Monolithic Silicon Microbolometer Arrays", Semiconductors and Semimetals, Vol. 47, Chapter 3, 43-121, 1997.
- <sup>xiv</sup> P.W. Kruse, "A Comparison of the Limits to the Performance of Thermal and Photon Detector Imaging Arrays", Proc. IRIS Detector, Vol. 1, 95-117, 1993
- <sup>xv</sup> J.M. Lloyd, "State-of-the-Art for Thermal Imaging", Opt. Eng. Vol. 14(1), Jan 1975
- <sup>xvi</sup> NVTherm 2002 manual, Night Vision Laboratory, Fort Belvoir, VA
- <sup>xvii</sup> NVTherm IP manual, Night Vision Laboratory, Fort Belvoir, VA.
- <sup>xviii</sup> J.M. Lloyd, "State-of-the-Art for Thermal Imaging", Opt. Eng. Vol. 14(1), Jan 1975
- <sup>xix</sup> J. Ratches, "Night Vision Laboratory Static Performance Model for Thermal Viewing Systems," RD Tech. Report ECOM-7043, 1975
- <sup>xx</sup> NVTherm 2002 manual, Night Vision Laboratory, Fort Belvoir, VA
- <sup>xxi</sup> NVTherm 2002 manual, Night Vision Laboratory, Fort Belvoir, VA
- <sup>xxii</sup> NVTherm IP manual, Night Vision Laboratory, Fort Belvoir, VA
- <sup>xxiii</sup> R. Blackwell, "17 micron 640x480 Microbolometer FPA Development at BAE Systems", Infrared Technology and Applications XXXIII, Proc. of SPIE Vol. 6542 (2007).
- <sup>xxiv</sup> P. Norton, "Uncooled Thermal Imaging Sensor and Application Advances", Infrared Technology and Applications XXXIII, Proc. of SPIE Vol. 6206 (2006).
- <sup>xxv</sup> S. Ropson, "a-Si 160x120 MicroIR Camera: Operational Performance", Proc. of SPIE Vol. 4393 (2001).
- <sup>xxvi</sup> Private communications with L-3 and BFE
- <sup>xxvii</sup> C. Li, "Recent Development of Ultra Small Pixel Uncooled Focal Plane Arrays at DRS", Infrared Technology and Applications XXXIII, Proc. of SPIE Vol. 6542 (2007).
- <sup>xxviii</sup> D. Murphy, "640x512 17 micron Microbolometer FPA and Sensor Development", Infrared Technology and Applications XXXIII, Proc. of SPIE Vol. 6542 (2007).
- <sup>xxix</sup> V. Zerov, "Heat Sensitive Materials for Uncooled Microbolometer Arrays", J. Opt. Technol. 68 (12) Dec 2001.
- <sup>xxx</sup> F. Niklaus, "Uncooled Infrared Bolometer Arrays Operating in a Low to Medium Vacuum Atmosphere: Performance Model and Tradeoffs", Infrared Technology and Applications XXXIII, Proc. of SPIE 2007
- <sup>xxxi</sup> C.M. Hanson, "Uncooled IR Detector Performance Limits and Barriers," Proc. SPIE Vol. 4028, Jul , 2-11, 2000
- <sup>xxxii</sup> MODTRAN, Ontar Corporation
- <sup>xxxiii</sup> <http://www.temmek.com/>
- <sup>xxxiv</sup> <http://www.fresneltech.com/>.
- <sup>xxxv</sup> Joint Integrated Product Team briefing 21-23 Aug 2007.
- <sup>xxxvi</sup> Shaw, J. A., P. W. Nugent, N. J. Pust, B. Thurairajah, and K. Mizutani, 2005: "Radiometric cloud imaging with an uncooled microbolometer thermal infrared camera," Opt. Express 13(15), 5807-5807.

- 
- <sup>xxxvii</sup> Thurairajah, B. and J. A. Shaw, 2005: "Cloud statistics measured with the Infrared Cloud Imager," *IEEE Trans. Geosci. Rem. Sens.* 43(9), 2000–2007
- <sup>xxxviii</sup> Nugent, P. W., J. A. Shaw, and S. Piazzolla, 2007: "Wide-angle infrared cloud imaging for measuring cloud statistics on Earth-space optical communication paths," *Proc. SPIE* 6709, doi: 10.1117/12.735047.
- <sup>xxxix</sup> Ushio, T., D. Katagami, K. Okamoto, and T. Inoue, 2007: "On the use of split window data in deriving the cloud motion vector for filling the gap of passive microwave rainfall estimation," *SOLA* 3, 1-4.
- <sup>xl</sup> Shaw, J. A., P. W. Nugent, N. J. Pust, B. Thurairajah, and K. Mizutani, 2005: "Radiometric cloud imaging with an uncooled microbolometer thermal infrared camera," *Opt. Express* 13(15), 5807-5807.
- <sup>xli</sup> Thurairajah, B. and J. A. Shaw, 2005: "Cloud statistics measured with the Infrared Cloud Imager," *IEEE Trans. Geosci. Rem. Sens.* 43(9), 2000–2007
- <sup>xlii</sup> Nugent, P. W., J. A. Shaw, and S. Piazzolla, 2007: "Wide-angle infrared cloud imaging for measuring cloud statistics on Earth-space optical communication paths," *Proc. SPIE* 6709, doi: 10.1117/12.735047.
- <sup>xliii</sup> Tamachi, R.L., H.B. Bluestein, S.S. Moore, and R.P. Madding, 2006: Infrared Thermal Imagery of Cloud Base in Tornadoic Supercells. *J. Atmos. Oceanic Tech.*, 23, 1445-1461.
- <sup>xliv</sup> David A. Anisi, John W. C. Robinson, and Petter Ogren. On-line trajectory planning for aerial vehicles: a safe approach with guaranteed task completion. In AIAA Guidance, Navigation and Control Conference, Keystone, Colorado, August 2006. AIAA Paper 2006-6107, American Institute of Aeronautics and Astronautics.
- <sup>xlv</sup> S. Peng and G. M. Morris, "Experimental demonstration of resonant anomalies in diffraction from two-dimensional gratings," *Opt. Lett.* 21, 549-551 (1996).
- <sup>xlvi</sup> D. Rosenblatt, A. Sharon, and A. A. Friesem, "Resonant grating waveguide structure," *IEEE J. Quantum Electron.* 33, 2038-2059 (1997).
- <sup>xlvii</sup> Z. S. Liu, S. Tibuleac, D. Shin, and R. Magnusson, "High-efficiency guided-mode resonance filter," *Opt. Lett.* 23, 1556-1558 (1998).
- <sup>xlviii</sup> P. S. Priambodo, T. A. Maldonado, and R. Magnusson, "Fabrication and characterization of high-quality waveguide-mode resonant optical filters," *Appl. Phys. Lett.* 83, 3248-3250, 20 October 2003.
- <sup>xlix</sup> [http://www.nikon.co.jp/main/eng/portfolio/about/technology/nikon\\_technology/vr\\_e/index.htm](http://www.nikon.co.jp/main/eng/portfolio/about/technology/nikon_technology/vr_e/index.htm)
- <sup>l</sup> Pentax K100D Shake Reduction Technology Fact Sheet
- <sup>li</sup> [http://ca.konicaminolta.com/products/consumer/digital\\_camera/slr/dynax-7d/02.html](http://ca.konicaminolta.com/products/consumer/digital_camera/slr/dynax-7d/02.html)
- <sup>lii</sup> [http://www.newscatech.com/squiggle\\_overview.html](http://www.newscatech.com/squiggle_overview.html)
- <sup>liii</sup> "Passive ranging using an infrared search and track sensor", deVisser, Maarten, Schwing, Piet B. W., de Groot, Johannes F., Hendriks, Emile A., *Optical Engineering*, February 2006, Vol. 45.
- <sup>liv</sup> The Range equation can be solved for  $R_{\text{detect}}$  by the use of the Lamberts W-function. Many times it is just iteratively solved.
- <sup>lv</sup> Eric Frew, Jack Langelaan and Maciej Stachura. "Adaptive Planning based on Information Velocity for Vision-Based Navigation", submitted to IEEE Transactions on Robotics, November 2007.
- <sup>lvi</sup> Oussama Khatib. Real-time obstacle avoidance for manipulators and mobile robots. *International Journal of Robotics Research*, 5(1):90–98, 1986.
- <sup>lvii</sup> Jack Langelaan and Steve Rock. Navigation of small UAVs operating in forests. In AIAA Guidance, Navigation and Control Conference, Providence, RI 2004.
- <sup>lviii</sup> Jacob W. Langelaan. State Estimation for Autonomous Flight in Cluttered Environments. PhD Dissertation, Stanford University, 2006.
- <sup>lix</sup> David A. Anisi, John W. C. Robinson, and Petter Ogren. On-line trajectory planning for aerial vehicles: a safe approach with guaranteed task completion. In AIAA Guidance, Navigation and Control Conference, Keystone, Colorado, August 2006. AIAA Paper 2006-6107, AIAA.
- <sup>lx</sup> Tom Schouwenaars, Eric Feron, and Jonathan How. Safe receding horizon path planning for autonomous vehicles. In 40th Allerton Conference on Communication, Control and Computing, Oct2002.
- <sup>lxi</sup> Y. Kuwata and J. P. How. Three dimensional receding horizon control for uavs. In AIAA Guidance, Navigation and Control Conference. AIAA Paper 2004-5141, AIAA, 2004.
- <sup>lxii</sup> Jusuk Lee, Rosemary Huand, Andrew Vaughn, Xiao Xiao, and J. Karl Hedrick. Strategies of path-planning for a uav to track a ground vehicle. In Second Symposium on Autonomous Intelligent Networks and Systems, June 2003.

- 
- <sup>lxiii</sup> Eric Frew, Tim McGee, ZuWhan Kim, Xiao Xiao, S. Jackson, M. Morimoto, S. Rathinam, J. Padiyal, and R. Sengupta. Vision-based road-following using a small autonomous aircraft. In Proceedings of the 2004 IEEE Aerospace Conference, volume 5, pages 3006–3015, March 2004.
- <sup>lxiv</sup> Ben Grocholsky, Alexei Makarenko, and Hugh Durrant-Whyte. Information theoretic coordinated control of multiple sensor platforms. In IEEE International Conference on Robotics and Auto, p 1521–1526, 2003.
- <sup>lxv</sup> L. F. Bertuccelli and J. P. How. Search for dynamic targets with uncertain probability maps. In Proceedings of the American Control Conference, June 2006.
- <sup>lxvi</sup> William J. Pisano and Dale A. Lawrence. Data dependant motion planning for UAV plume localization. In AIAA Guidance, Navigation and Control Conference. AIAA, 2007.
- <sup>lxvii</sup> Oussama Khatib. Real-time obstacle avoidance for manipulators and mobile robots. International Journal of Robotics Research, 5(1):90–98, 1986.